UNIVERSITY
OF MANITOBA

Comparative Oxidation Study of
Un-Coated and Coated
CMSX-4 and CMSX-486
Single Crystal Superalloys

By: Mathew MacMaster Smith

A thesis submitted to the Faculty of Graduate Studies of
The University of Manitoba
In partial fulfillment of the requirements for the degree of

MASTER OF SCIENCE

Department of Mechanical and Manufacturing Engineering
University of Manitoba
Winnipeg, Canada

Abstract

Microstructural comparison of the isothermal oxidation performance of an experimental Ni-5Cr-15Al overlay coating applied to CMSX-4 and CMSX-486 was performed at 1100 °C. High temperature oxidation was carried out in a box furnace for a maximum duration of 192 hrs. Samples were periodically removed and the oxide, coating and substrates microstructurally analyzed using SEM, EDS and XRD equipment. Un-coated CMSX-4 and CMSX-486 were also oxidized using the same conditions in an attempt to understand how the coating affected oxidation performance based on microstructural changes. Results show that both CMSX-4 and CMSX-486 have unacceptable oxidation characteristics in the un-coated condition, where CMSX-486 had significantly better performance than CMSX-4. However, in the coated condition, both CMSX-4 and CMSX-486 had no significant difference in oxidation performance. It was found, in the un-coated and coated conditions, that the role of Hf in CMSX-486 played a significant role in determining oxidation performance of the material.

Acknowledgements

I would like to thank my supervisor Dr. O. A. Ojo for giving me the opportunity to work on this interesting project and for his helpful perspective on various aspects leading to the completion of this work and for providing the funding for this project. I am also grateful to my co-supervisors Dr. Zhao of the NRC and Dr. C. Deng of the University of Manitoba for their insight on many aspects of this project.

I would also like to thank the Structures and Materials Performance Laboratory at the Institute for Aerospace Research of the National Research Council of Canada located in Ottawa, Ontario for providing the coating equipment and coating material used in this work. I would like to thank Dr. Zhao and the technical staff at the NRC for their time in completing the deposition of the coating material.

I am grateful for the assistance received regarding the equipment in the Materials Laboratory in the Mechanical and Manufacturing Department at the University of Manitoba provided by Mike Boswick. In addition, I would also like to thank Dr. R. Sidhu and Neil Ball in the Geology Department at the University of Manitoba for their help with various aspects of EDS and XRD data collection.

I would also like to thank my colleagues, Clark Murray, Oyedele Ola Temitope and Mark Amegadzie for their insight on many different aspects encountered throughout this work.

Finally I would like to thank my parents, for their continued support throughout my university career, and God for giving me the patience, knowledge and understanding required to see this project through to completion.

Table Of Contents

List of Figures

List of Tables

1.0 Introduction, Objectives and Scope of Project

The modern world has been greatly influenced by the invention and advances of gas turbine engines. The first application of a gas turbine for use in an aircraft was developed by Germany at the end of the Second World War with the production of the Messerschmitt ME 262 Schwalbe (‘Swallow’), powered by the Jumo 004 gas turbine engine [*1*]. This early jet engine was very inefficient, and was fraught with problems. Since then, developments in mechanics, fluid dynamics, aerodynamics and material engineering have provided the basis of the modern turbo jet engines used in both civil and military aircraft, as well as in some stationary power generation applications [*2*].

Turbine blades are one of the most critical components in modern gas turbine engines. The total power produced, as well as the efficiency of the engine will be closely determined by the condition of each turbine blade. As gas turbine engines get bigger and more sophisticated in an attempt to generate more power and have better efficiency, the turbine blades must be capable of withstanding a more demanding environment. These environments typically include high centrifugal stresses and temperatures (exceeding 1500 °C), which result in rapid deterioration of the turbine blades, and by extension their performance, through mechanisms such as creep, fatigue, oxidation and hot corrosion [*2, 3, 4*]. The limiting factor in all engineering applications, especially ones that include an increase in turbine entry temperature (TET) is the material.

Since the invention of the gas turbine at the end of World War II, many advances have been made in the area of turbine material in order to increase the maximum combustion temperature. These advancements include changing the alloy composition, addition of doping elements to improve fatigue and high temperature creep strength, to more recent developments of directionally solidified and single crystal superalloys [*2*, *3, 4*]. However, despite the advancements in turbine material composition and structure, engine temperatures are pushing the boundaries of even the most resilient superalloys. This has lead to the development of turbine blade air-cooling, which in turn has been replaced by coated air-cooled blades [*3*]. All of these advancements have one common purpose, to increase operating temperature of the turbine blades, reliability of the engine as a whole and the operating life of the turbine blades thereby limiting the down time and costly overhauls. The development of protective coatings is critical to the continued improvement of gas turbine efficiency.

The use of diffusion based coatings led to the development of aluminized steels in order to reduce hot corrosion and extend the life of the turbine blades in early jet engines [*1*]. The continued use of such coatings resulted in all alloys used in gas turbine engines to be coated between 1944 and the 1970's [*1*]. By the mid 1970's diffusion based coatings gave way to the more advanced overlay coatings. Also during this time, thermal barrier coatings (TBC's) were developed for use in gas turbine engines on military aircraft [*1*]. By the late 1980's, TBC's were starting to be more commonly found in use on civil aircraft. The advantage of TBC's is they can lower the temperature across the coating by as much as 170 ℃. By combining coating with blade cooling technology, a substantial improvement in gas turbine engine efficiencies was made possible [*3*]. However, coated turbine blades are still susceptible to failure, which recently has been a subject of great interest.

Considerable research has been done on developing coatings over the past 70 years. In that time, several desirable properties for coatings have emerged as requirements before the coating is used on any commercial or military aircraft. These properties include: slow thermally grown oxide (TGO) growth rates (accomplished by the addition of reactive elements (RE) [*5, 6*]), high temperature protection from hot corrosion and high temperature oxidation (by the development of TBC and overlay systems [*7, 8, 9, 10, 11*]), and strong TGO adherence to the coating material (by the development of alumina forming oxides through surface treatments and application techniques [*12, 13, 14*]), while maintaining or improving the structural properties of the substrate material such as creep and fatigue life [*15*]. The lifetime of this protective thermally grown oxide, depends greatly on the slow diffusion of various cations and anions through the TGO scale, in addition to various other microstructural phenomena, such as phase changes and formation of high stress zones. It therefore can be stated that understanding the microstructural interactions between the coating and substrate material is of critical importance to maximizing the lifetime of the protective coating and in turn, the turbine blades [*5, 15, 16, 17, 18, 19, 20, 21*].

The primary goal of this work is to study the oxidation performance of an experimental Ni-5Cr-15Al overlay coating on CMSX-4 and new CMSX-486 Ni-based superalloys by observing the microstructural changes that occur during high temperature isothermal oxidation. Specifically in this work the aim is to analyze the interaction between the coating and substrate though microstructural analysis using scanning electron microscopy (SEM), energy dispersive spectroscopy (EDS) and x-ray diffraction (XRD) and relate this interaction to the performance of the coating.

The substrate CMSX-4 was chosen because it is one of the most commonly used single crystal Ni-based superalloy material used in jet engine turbine blades. In practice, some stray grain boundaries do form in larger single crystal parts as defects in the directional solidification process. Consequently, in order to improve the high temperature mechanical properties of materials containing these defects, addition of grain boundary strengthening elements C, B, Hf and Zr, have been added to CMSX-4 to produce a new single crystal superalloy known as CMSX-486. There have been no comparative oxidation studies between CMSX-4 and CMSX-486 reported in literature.

This project is divided into two sections in order to properly observe and identify the major microstructural changes that occurred as part of coating deposition and heat treatment and changes that occurred as a result of high temperature exposure.

1) <u>High Temperature Oxidation of CMSX-4 & CMSX-486</u>

   In this preliminary stage fundamental behavior of the substrate oxidation behavior was investigated. This investigation looks at the substrate material only during high temperature isothermal oxidation where the oxidation characteristics of the base material are studied. Microstructural changes, identification of phases and tracking of the variation in element concentrations are important for determining how the base material performs during oxidation. This was achieved through SEM, XRD and EDS analyses. The results are presented and compared to observations reported in literature to confirm any similarities. The final results are also compared to the results of the NiCrAl coated material in order to present how the coating changes the oxidation behavior of the substrate materials.

2) High Temperature Isothermal Oxidation of CMSX-4 & CMSX-486 with Ni-5Cr-15Al Overlay Coating

This stage is the primary focus of this work, which includes an analysis of the microscopic interaction of the overlay coating and substrate material after isothermal oxidation testing. The results are compared with Stage 1 to identify differences in oxidation phenomena in order to present mechanisms of coating oxidation performance. Microstructural analysis of the coating and substrate was accomplished through the identification of phases, analyses of chemical composition and morphology of various constituents by SEM, EDS and XRD techniques. Comparisons between observed oxidation characteristics of the coated and un-coated materials are presented and compared with similar experiments reported in literature to verify the experimental outcome.

2.0 Technical Background

The following sections describe some of the technical background critical to understanding the environment in which turbine blades operate. Topics covered include: superalloy composition, hot corrosion and high temperature oxidation, types of protective coatings and their role in prevention of hot corrosion and high temperature oxidation, stages of alumina formation and some coating failure mechanisms that have been reported in literature.

2.1 Superalloy Materials

Since the creation of the German ME262 fighter jet, there have been numerous advancements in jet engine materials. The driving force for these advancements was related to improving the engine power/thrust and more recently efficiency, by increasing the combustion temperature within the combustion chambers. The limiting factor was the materials capability to perform without failing in the hot and more volatile environments within the hot gas stream of jet engines.

From a mechanical loading point of view, the materials in the hot gas stream, as well as in the compressor stages, need to withstand very high rotational loads, generated by the extremely high rotational speeds (up to 150 000 rpm) [*22*]. In addition, high temperatures, especially in the turbine regions of the engine, require additional considerations including the material’s resistance to creep and high temperature fatigue, (commonly known as thermal-mechanical fatigue or TMF). Since materials exposed to the hot gas stream are often subjected to temperatures exceeding 500 ℃, hot corrosion and high temperature oxidation resistance (discussed further in Section 2.2) needs to be accounted for as well [*23*]. Depending on the application requirements of the materials, the presence and quantity of the various alloying elements can be tweaked to ensure optimum performance. Therefore, the general requirements for any superalloy are as follows [*24*]:

1) High mechanical strength at elevated temperature
2) High resistance to creep and thermal-mechanical fatigue
3) High resistance to hot corrosion and high temperature oxidation
4) High microstructural and mechanical property stability at elevated temperatures
5) Low weight

There are three common superalloys used, which include nickel-based, iron-based and cobalt-based. In particular, nickel-based superalloys form a stable FCC matrix with high solubility for other alloying elements [*25, 22*]. This high solubility allows the matrix to be strengthened through substantial solid solution strengthening and precipitate hardening mechanisms, giving the superalloys their excellent high temperature strength and creep resistance [*25*].

2.1.1 Composition of Superalloy Materials

As previously mentioned, a considerable amount of the superalloy's creep and other mechanical properties is attributed to its alloying element composition. Most modern superalloys can have up to ten or more elements dispersed throughout the base material matrix, creating an assortment of different phases that can either be beneficial or detrimental to the alloy's properties, as discussed in Section 2.1.2[*]. Therefore, an understanding of what each element does in the superalloy is critical in developing a superalloy with the properties required for the application [*4, 22, 24, 26*, *27*]:

<u>*Nickel:*</u> Forms the base or matrix of the alloy and accounts for 40-60 wt% of the total alloy.

<u>*Chromium:*</u> Included to improve the hot corrosion resistance of the material and provide moderate high temperature oxidation resistance for applications under 1000 °C. At temperatures above 1000 °C the protective Cr_2O_3 layer vaporizes to become volatile CrO_3 [*3, 25*].

<u>*Aluminum:*</u> Most superalloys include some quantity of aluminum because it forms the γ' phase [$Ni_3(Al,Ti)$] within the γ matrix. This phase provides precipitate hardening and increased high temperature strength. Aluminum also forms Al_2O_3, which is a stable and adherent oxide that provides excellent high temperature oxidation and Type I hot corrosion resistance at temperatures well above 1000 °C.

<u>*Cobalt:*</u> Included to reduce the solubility of γ' forming elements like aluminum and titanium.

<u>*Titanium:*</u> Contributes to the formation and strengthening of the γ'phase. In addition, small amounts have shown to increase the rate at which transient alumina forms stable alumina [*3*]. More recent superalloys have a reduced amount of titanium

---

[*] For the purpose of this work, nickel-based superalloys will be the topic of further discussion.

because it has shown to have a detritus effect on the formation of an adherent oxide scale. Often cracking in titanium rich oxide layers has been observed, leading to the acceleration of oxide spallation [*26*].

Tantalum: Solid solution strengthener and strong former of MC carbides.

Tungsten: Solid solution strengthener and strong carbide former (M_6C and MC type)

Rhenium: First included in second generation superalloys to increase the creep strength through the promotion of rafting making the misfit between γ/γ' larger. Later, additional work concluded that additions of rhenium slow the diffusion rate in nickel-based superalloys when exposed to elevated temperatures and stabilize α-Cr [*5, 22*]. Furthermore, studies performed on the effects of rhenium on the formation of detrimental constituents such as topologically close-packed (tcp) phases showed that additions of rhenium increase the instability of tcp phases at lower and moderate temperature ranges, while delaying the precipitation of these phase at higher temperatures [*28, 29*].

Molybdenum: Solid solution strengthener and strong carbide former (M_6C type)

Hafnium: Increases oxide scale adherence and reduces aluminum diffusion to the oxide [*30*]. However, too much hafnium has been shown to cause premature oxide spallation [*30*]. Hafnium has also been shown to reduce the effect of oxidation induced rumpling of thermally grown oxides when present in optimum quantities [*31*].

Yttrium: Increases oxide scale adherence and reduces aluminum and oxygen diffusion rates resulting in lower oxidation kinetics and longer lasting and adherent protective oxides. Yttrium oxide ‘pegs’ between the TGO and the substrate helps to physically/mechanically attach the oxide to the substrate material. However, too much yttrium results in the formation of many ‘pegs’ that can result in localized high stresses, which increases the oxide spallation rate [*9, 12, 15, 32*].

Boron, Carbon and Zirconium: In small amounts these elements help stabilize the grain boundaries [*4, 33*]. As a result, grain boundary strength and resistance to slip is increased. However, the addition of B, C, Zr and even Hf has been shown to decrease the incipient melting temperatures of the superalloys, thereby increasing the difficulty of fully solution heat treating the γ - γ' eutectic phase without incipient melting occurring within the alloy [*25*].

2.1.2 Microstructure and Phases of Nickel-Based Superalloys

As with all materials, the properties of superalloys depend on the microstructure and phases that occur as a result of material processing. Most nickel-based superalloys have alloying elements partition into one or more of the following phases:

Gamma Matrix (γ): A continuous fcc nickel-based phase that contains high concentrations of solid-solution elements (Co, Cr, Mo, W) [*4, 25, 27*].

Gamma Prime (γ'): The main precipitate strengthening phase formed upon cooling of the supersaturated solid solution (γ or matrix phase). This phase typically has higher concentrations of Ti and Al, and has nominal composition of Ni_3(Al, Ti) in an fcc crystal structure [*24, 25*]. The lattice miss-match between the γ - γ' phases is approximately .5% [*34*] resulting in low interfacial energy allowing for greater stability at elevated temperatures [*22*]. The high temperature creep resistance and strength of the alloy is highly dependent on the quantity, morphology and distribution of this phase [*4, 24, 25, 27*].

Gamma – Gamma Prime Eutectic (γ - γ' Eutectic): A phase that forms during the solidification process as solute from the solidifying dendrites segregates into the still liquid interdendritic regions. As solidification continues and solidification of the interdendritic region initiates, the supersaturated interdendritic regions rich in γ' forming elements begin to form large γ' particles, which are separated by thin lamina of the γ matrix phase [*25*].

Secondary Gamma Prime: Precipitates of γ' which form from secondary heat treatment or result form exposure to high temperatures. Upon exposure to elevated temperatures, approaching the solvus temperature for γ', a solid solution (γ phase) is formed. Cooling from this temperature results in the formation of small precipitates of secondary γ' [*24, 25*].

Carbides: The addition of .02 to .2 wt% carbon in nickel-based superalloys causes a reaction between the carbon and reactive elements like Ti, Ta, Hf, Mo and sometimes Cr to form carbides. Typically, in the as-cast condition, carbides are present in the form of MC (where M is a reactive metal), which serve to reduce grain boundary sliding. However, too many carbides reduce stress relaxation causing premature failure [*25, 35*]. During high temperature exposure or heat treatments, MC carbides decompose to form $M_{23}C_6$ or M_6C carbides along grain boundaries or in solid solution alloys after very long exposure times [*25*].

Topographically Close-Packed Phases (tcp phases): Appearing as needle or plate like structures, tcp phases, such as σ, μ, χ, P, R or Laves phases, are brittle, low strength phases that deplete the matrix of reactive elements (Cr, Ti, Ta, Re, W, Mo, Co) [*25*]. The precipitation of these phases is slow, often only occurring after considerable time at elevated temperatures [*24*].

Despite the advancements in superalloy composition and microstructure through manufacturing processes, working temperatures exceeding .7 - .9 of the absolute melting temperature of the material are pushing the boundaries of even the most resilient superalloys [*24, 25*]. This has lead to the development of turbine blade air-cooling technology, which in turn, has been replaced by coated blades in addition to air-cooling. All of these advancements have been implemented to: increase operating temperature of the turbine blades, increase engine efficiency and power, increase reliability of the engine as a whole and increase the operating life of the turbine blades thereby limiting the down time and costly overhauls. The understanding and development of such protective coatings are critical to the continued improvement of gas turbine efficiency and reduction in damage from hot corrosion and high temperature oxidation.

2.2 Hot Corrosion and Other Forms of High Temperature Corrosion

Hot corrosion represents an accelerated degradation of material at elevated temperatures as a result of the interaction between oxygen and other contaminants found in the hot gas stream within the jet engine. In this section hot corrosion mechanisms are outlined. And an additional common type of corrosion, vanadic corrosion, is also briefly discussed.

2.2.1 Type I and Type II Hot Corrosion and Corrosion Mechanisms

Hot corrosion is a reaction with SO_4 (sulfates) or other corrosive materials from fuels, contaminants or other foreign object debris, that result in the deterioration of the protective oxide layer and subsequently, the base material leading to the failure of the part. Hot corrosion can be broken up into two types. Type I hot corrosion is typically observed between 750 – 900 °C. It often involves the transport of sulphur from a sulphur containing deposit across the protective oxide layer and into the metal base material where metal sulphides form, causing failure of the coating and/or the base material. Coatings rich in Al are required for protection against Type I hot corrosion [*1, 3, 36*]. Type II hot corrosion occurs over a lower range of temperatures, between 600-850 °C [*1, 3, 36*]. Type II hot corrosion involves the formation of metal sulphates, requiring a certain partial pressure of sulphur trioxide to provide a stabilizing effect. The oxides react with alkali metal sulphate deposits forming a low melting point compound preventing the further formation of stable protective oxides.

The use of coatings with high Cr or Si content is best suited for protection against Type II hot corrosion [*36*].

The mechanisms of hot corrosion result from the initial interaction of the molten deposit, usually Na_2SO_4, with surface oxide subsequently progressing to a rapid interaction with the base material [*18, 37*]. These interactions are described as acid or basic fluxing mechanisms depending on the composition of the deposit and the material interacting with the deposit. Basic fluxing results when the molten Na_2SO_4 produces oxide ions from the removal of O and S from the reaction with the coating or base material. These oxide ions react with metal oxides producing complex metal oxide, which dissolve in the molten deposit as shown in Equation (1) where M represents a metal cation [*3*].

$$MO + O^{2-} = MO_2^{2-} \tag{1}$$

Acid fluxing results when the oxide ions in the molten deposit are low compared to the equilibrium concentrations. This results in the metal oxides dissolving into the molten deposit causing the donation of oxide ions as shown in Equation (2) [*3*]. The dissolution of metal oxides from the turbine blade results in the loss of high temperature protection, and eventual degradation or failure of the blade.

$$MO = M^{2+} + O^{2-} \tag{2}$$

It can be noted that in order for hot corrosion to occur there must be an interaction between the surface of the coating or base material, with molten (or semi molten) deposits. This requirement means there must be trace metal elements with reactive species, like SO_4/SO_3, which are deposited on hot gas stream components. The presence of such metal and reactive materials in the hot exhaust of the combustion chamber can be attributed to: contamination of aviation fuels with high sulfur and trace metals, the injection of sea water into the inlet diffuser, or the consumption of other foreign objects through the inlet diffuser which may contain high sulfur and trace metals [*3*]. There are several different processes that form corrosive deposits, such as direct inertial impact, eddy diffusion and vapor deposition. However, the exact dynamics of the formation processes are beyond the scope of this work [*3*].

2.2.2 Other forms of Hot Corrosion

An additional form of hot corrosion can occur that does not require sufficiently high levels of sulfur trioxide or sulfates to form a corrosive deposit. Vanadic corrosion, like the name implies, forms highly corrosive low melting point vanadium deposits on hot gas stream surfaces. Vanadic corrosion occurs when vanadium contaminates in the fuel react with sodium found in salt water taken in by the air inlet diffuser, to form molten sodium vanadyl vanadate deposits. Similar to Type I and Type II hot corrosion, these vanadium deposits can flux the coating and substrate material causing eventual failure of the coating and/or the base material. Vanadic corrosion usually occurs in the temperature range of 535 – 950 ℃ [*3, 18*].

2.3 High Temperature Oxidation

As previously mentioned, the ability of a superalloy or coating to quickly produce a stable protective oxide layer will determine the blade's ability to resist hot corrosion and high temperature oxidation. However, it should be noted that some protective oxides become volatile at certain temperature ranges and all oxides have an upper temperature limit for which the oxide will fail. For instance, the rate at which chromium oxides form is quick when compared to aluminum oxides. This makes chromium oxide a preferred oxide since it will form quickly to protect the base material, and will repair itself quickly in the event the oxide layer spalls or is damaged by foreign object debris. Unfortunately, chromium oxide becomes volatile at temperatures over 1000 ℃, therefore requiring the formation of the more stable alternatives, like aluminum oxide, for environments where the temperature exceeds 1000 ℃. It is therefore critical to know the limits of each oxide and mechanisms controlling high temperature oxidation in order to engineer a proper alloy or protective coating for any given application [*3, 25, 36*]. The following section outlines high temperature oxidation processes and mechanisms as well as the thermodynamics, kinetics and formation of oxides in Ni-Al-Cr containing alloys and coatings.

2.3.1 High Temperature Oxidation

High temperature oxidation is the reaction of the base metal with oxygen at high temperatures. Generally, high temperature oxidation is the dominant failure mode at temperatures exceeding approximately 900 ℃ [*18*]. High temperature oxidation processes are often complex when dealing with alloys, however, the basic process can be outlined as follows [*3*]:

1) Oxygen reacts with the metal surface or the surface of the coating
2) The reacting oxygen creates a thin initial metal oxide layer
3) The diffusion of metal cations to the surface of the metal oxide scale increases the oxide scale thickness
4) Oxygen is diffused into the metal through the growing oxide scale, producing internal oxidation
5) Microcracks are formed in the base metal and/or in the growing oxide scale due to microstructural changes causing stress concentration sites
6) Microcracks coalesce to form visible cracks at or near the base metal and oxide interface. Changes in temperature or additional loading stresses can cause the protective oxide layer to spall, thus resulting in an unprotected area of the base metal.
7) If there are enough reactive elements, like Al and Cr, left in the alloy close to the surface, the protective oxide scale formation will restart. If these elements are depleted, other elements may preferentially oxidize creating an unprotective oxide scale resulting in mass lost and eventual failure of the material.

Typically, for oxidation of Ni-Cr-Al containing alloys and coatings, several different oxidation mechanisms are observed depending on the reactive elements present, oxygen partial pressure and other parameters. Presented in this work are three of the more commonly observed oxide scale development mechanisms.

Previous studies by Reed *et al.* [*38*] and Huang *et al.* [*39*] showed as Ni-Al-Cr containing superalloys were oxidized, a NiO layer formed over an internal oxidation zone, composing of Cr_2O_3 and Al_2O_3 (mechanism I). The NiO forms in three stages. The first stage consists of absorption of oxygen and the formation of an oxygen surface structure (oxide), which differs from the orientation of the surface Ni structure. The second stage involves the nucleation of the NiO scale and lateral growth along the surface of the base material. Before stage two has completed, stage three starts, which involves the logarithmic growth of the oxide scale in the transverse direction. This stage is also commonly referred to as the thickening stage due to the rapid thickening of the NiO layer. These three stages were shown to be highly dependent of the temperature and partial pressure of the oxygen rich environment, but so far there has been no relation to the substrate orientation [*38*]. Even though NiO forms relatively quickly, its protection against hot corrosion or high temperature oxidation is relatively short lived due to the easy diffusion of oxygen through the thin oxide scale [*38*].

The other two mechanisms of oxide formation occur in a similar manor, however the predominate oxide that forms on the outer layers are of a slightly different composition. Mechanism II is where the outer oxide layer is composed of fast forming Cr_2O_3 over slower forming internal Al_2O_3 regions, and mechanism III is the growth of a continuous Al_2O_3 layer under the external Cr_2O_3 [*39*].

Depending on the conditions and relative presence/concentration of reactive elements, there may be localized differences in oxidation mechanisms due to microsegragation. This difference can be easily noted when comparing the initial oxidation behavior between the dendritic and interdendritic regions of the superalloy. In addition, since the formation of various oxides is highly dependent on temperature, diffusion, presence of defects or impurities and oxygen partial pressure, the oxidation mechanism can change as the oxides develop and thicken. This is especially true after the initial coherent oxide film has developed, where subsequent oxidation requires solid-state diffusion of cations (M^{n+}) and anions (O^{2-}) through the oxide film [*32*, *39, 40*]. If the diffusion of cations is dominant, the oxide scale will grow at the scale/gas interface; however, if the diffusion of anions is dominant, the oxide scale will grow at the scale/substrate interface. Anion dominant scale growth is generally not beneficial since growth of new scales under existing oxide layers generates high growth stresses, which may result in oxide cracking or spallation [*3*].

Since Ni-based alloys have superior fatigue and creep resistances at high temperatures, these alloys are often used in temperatures exceeding 1000 °C. Therefore, there is a need to form a thicker, more durable oxide scale to increase the protection against hot corrosion and oxidation [*3*].

2.3.2 Alumina Scale

Alumina formation is highly sought after because of its dense, protective scale characteristics, which make it excellent for high temperature oxidation and Type I hot corrosion resistance. Alumina forms when sufficient Al is subjected to an oxidizing atmosphere. Often, additional Al is added to the substrate material by the application of a coating in order to provide an Al reservoir to maintain the protective alumina scale during extended high temperature exposure.

The first oxide that forms is often a transient or meta-stable aluminum oxide. Transient alumina, θ- or δ-Al_2O_3 being among the most common forms of transient alumina a having cubic structure, will initially form very quickly with plate like or needle-like morphology [*3*]. These forms of alumina have various distortions in the lattice crystal, making diffusion much quicker thereby speeding up the formation of additional transient alumina [*3*]. Over time, the transient alumina will transform into the most thermodynamically stable α-Al_2O_3, which can be thought as having no distortions in the now hexagonal crystal lattice. However, this transition to a more stable and protective form of alumina comes at a cost. Since this lattice has a close to perfect crystal structure, there are no distortions, which causes an approximate 5% reduction in volume associated with this change in phase. This volume reduction results in an increase in oxide stresses, providing a means of oxide failure, as discussed in Section 2.5.

Once α-Al_2O_3 forms, it becomes the dominant form of aluminum oxide during steady state oxidation. This is where continued transport of Al to the oxide and O through the oxide scale will continue to produce α-Al_2O_3 until Al concentrations below the oxide/metal interface fall below a critical value [*3*]. At which point, the alumina scale will no longer self heal after spallation.

2.3.3 Thermodynamics of Oxidation

The driving force of oxidation, and other degradation mechanisms of metals in a reactive environment, is thermodynamics [*3*]. Therefore, an important tool for understanding oxidation processes is equilibrium thermodynamics. However, since equilibrium thermodynamic expressions are formulated under equilibrium conditions, prediction of corrosive products is not possible. Nevertheless, equilibrium thermodynamic calculations do allow for the evaluation of reaction products, (if the products will evaporate, or form an unstable or stable compound) [*23*].

For standard temperature and pressure and a reaction between a metal and a gas, the second law of thermodynamics as described by Gibbs free energy (G') of a system, Equation (3), provides a starting point for thermodynamic analysis of an oxidation reaction [*3*].

$$\Delta G' = \Delta H' - T\Delta S' \tag{3}$$

where $\Delta\mathrm{G}'$ is Gibbs free energy, $\Delta\mathrm{H}'$ is the enthalpy, $\Delta\mathrm{S}'$ is the entropy and T is the absolute temperature. For these conditions Equation (3) states that if $\Delta\mathrm{G}' < 0$, the reaction will be spontaneous, if $\Delta\mathrm{G}' > 0$, the reaction will be nonspontaneous, if $\Delta\mathrm{G}' = 0$, the reaction is at equilibrium [*3*].

For the oxidation of a metal given by Equation (4), Gibbs free energy can be written in the form of Equation (5) [*3*].

$$aM + \frac{b}{2}O_2 = M_aO_b \tag{4}$$

where M is the reacting metal in an oxygen rich environment, and M_aO_b is the product oxide and a and b are the reacting moles of their respective reactants.

$$\Delta G' = \Delta G^{\circ} + RT \ln\left[\frac{a_{oxide}}{{a_M}^a \cdot {a_{O_2}}^{b/_2}}\right] \tag{5}$$

where ΔG° is the standard Gibbs free energy, R is the universal gas constant and a is the reactivity of the reactants and products. At high temperatures, the activity of oxygen can be approximated by its partial pressure during the reaction. Therefore, at equilibrium, $\Delta G' = 0$ and Equation (5) can be re-written as shown in Equation (6) [*3*].

$$\Delta G^{\circ} = -RT \ln\left[\frac{a_{oxide}}{{a_M}^a \cdot {a_{O_2}}^{b/_2}}\right] \tag{6}$$

For an oxidation reaction to occur, the oxygen partial pressure must be greater than the oxygen partial pressure at equilibrium. Therefore, ΔG° must be less than zero [*23*]. Using Equation (6) the activity of oxides at various temperatures and oxygen partial pressures can be plotted to form an Ellingham diagram, similar to the one shown in Figure 1. These diagrams can be used to identify the occurrence and stability of an oxide on a particular alloy or coating under various temperatures and oxygen partial pressures. Knowledge of the stability of an oxide can aid in the development of alloys and coatings for any high temperature application. Careful selection of elements to promote the formation of stable oxides will help protect the base material from further oxidation.

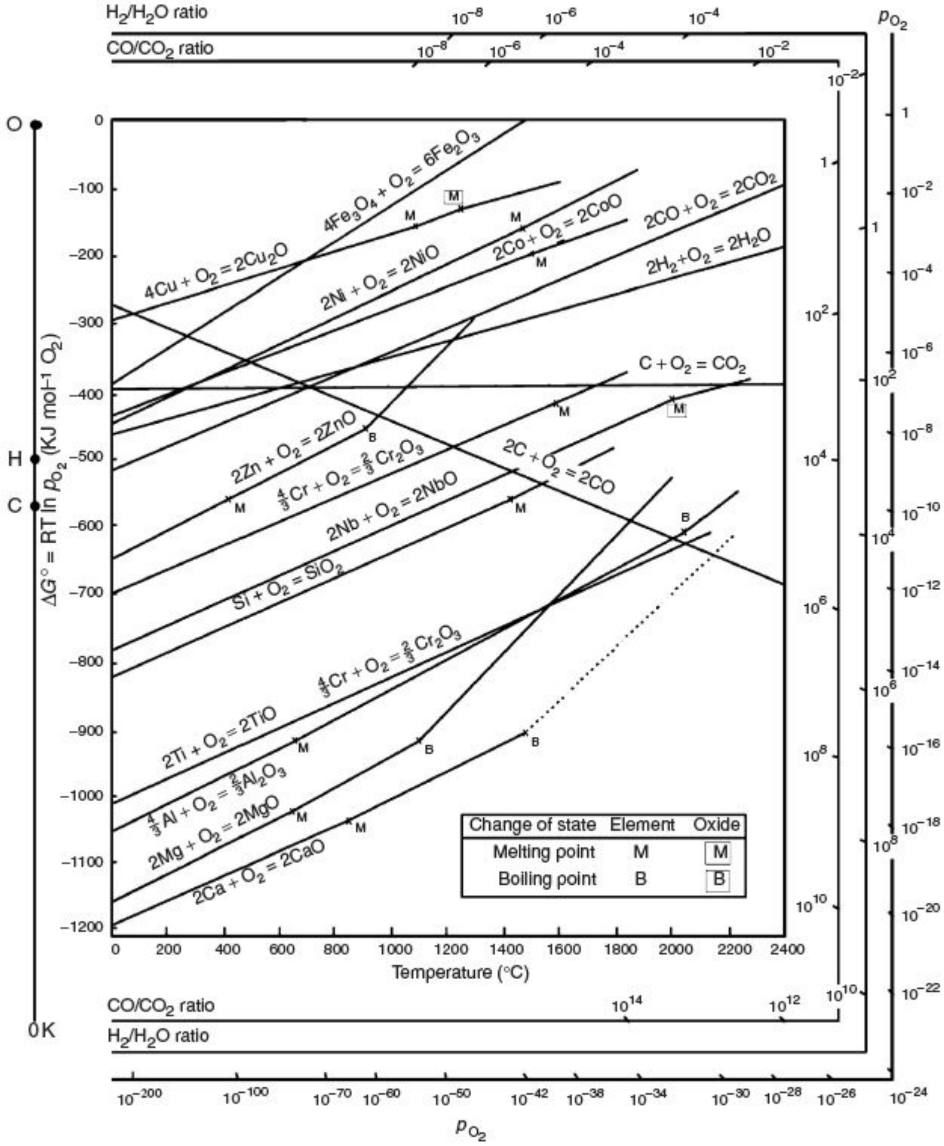

Figure 1: Ellingham diagram illustrating common oxides at various temperatures. Taken from Introduction to the High Temperature Oxidation of Metals [*23*]. Reprinted with the permission of Cambridge University Press.

The more negative the Gibbs free energy, the more stable the oxide is. For example, Al_2O_3 is more negative than NiO, and therefore more thermodynamically stable. However, the stability of the oxide does not necessarily mean that the oxide will be protective (for example Cr_2O_3 is protective until 1000 ℃) or that the oxide will form fast enough to provide protection [*3, 25*]. Therefore, it is also important to know the oxides growth rate (kinetics).

2.3.4 Diffusion Kinetics of Oxidation Processes

A kinetic analysis of an oxidation process provides information regarding the rate of the oxidation reaction. Often, kinetic analysis is done to complement the thermodynamic approach in order to more fully explain the mechanisms of oxidation [*25*]. From early work done on oxidation [*41, 42*], oxidation kinetics of metals and alloys obtained from thermogravimetric analysis can be described by a parabolic rate law given in Equation (7) [*43*].

$$\Delta m^2 = k_p t \tag{7}$$

where Δm is the mass change per unit area typically given as mg/cm^2, k_p is the parabolic rate constant and t is the time in seconds.

Later work done by Wagner described the parabolic behavior of oxidation of metals as a direct result from the control of the oxide scale growth by diffusion, thereby making the parabolic rate constant controlled by self-diffusion coefficients of cations or anions across the oxide scale [*23, 43*]. Wagner’s theory was applicable under the following assumptions [*23*]:

1) The oxide scale is dense, compact and perfectly adherent allowing for ion/electron migration
2) The diffusion of ions/electrons within the scale is the rate controlling step
3) Thermodynamic equilibrium at the interfaces and throughout the scale is established

A detailed derivation of Wagner's Theory on oxidation can be found in literature, [*23, 25*]. Since thermodynamic equilibrium is assumed, purely parabolic law is rarely observed during actual oxidation testing, making it only applicable to a limited number of pure metals. As such, variations in rate laws are often reported in literature, which include sub-parabolic, linear, logarithmic and inverse logarithmic [*3*]. Logarithmic and inverse logarithmic rate laws are typically only observed at lower temperatures, with thin films or at the start of oxidation, and as such will not be discussed as apart of this work [*3*].

Linear oxidation occurs when a non-protective oxide scale develops, which does not prevent or retard further oxidation. This is seen as a steady increase in mass with exposure time. The kinetics is described by Equation (8).

$$\Delta m = k_l t \tag{8}$$

where k_l is the linear rate constant, Δm is the change in mass per unit area in mg/cm^2 and t is the time in seconds [*3*].

Sub-parabolic oxidation occurs when the initial oxide that forms is non-protective, indicated by a linear trend between mass gain and oxidation time. Later, the non-protective oxide is replaced by a more protective and adherent oxide, which is indicated by a near parabolic or parabolic relationship between mass gain and oxidation time [*3*]. Sub-parabolic kinetics can be described by Equation (9) [*3*].

$$t = A + B(\Delta m) + C(\Delta m^2) \tag{9}$$

A, B and C are constants where $\frac{1}{k_l}$ and $\frac{1}{k_p}$ correspond to B and C respectively [*3*].

An alternative to calculating the rate constants based on plots of mass change vs. time, the Wagner Theory can be adapted to produce oxidation constants based on oxide thickness. This is especially useful for coated materials that may not have significant mass change during high temperature exposure. Equation (10) describes parabolic oxidation kinetics based on oxide thickness [*44*].

$$\xi^2 = k_p t + C \tag{10}$$

where ξ (in meters) is the oxide thickness after exposure time t (in seconds), k_p is the parabolic rate constant and C is an integration factor [*44*].

Modification of Equation (10) to account for sub-parabolic oxidation gives the following Equation (11) [*44*].

$$\xi^n = k_n t + C_n \tag{11}$$

where n is the growth exponent and k_n is the sub-parabolic rate constant, and C_n is the initial oxide thickness [*44*]. If n=2 Equation (11) becomes equivalent to Equation (10) and the state of oxidation is said to be ideally parabolic as described by Equation (7).

Oxidation kinetics is influenced by many factors such as: temperature, pressure, grain size, presence of defects and the relative activity of elements to name a few [*3, 23, 25*]. This makes comparison between separate tests, or results reported in literature difficult since the exact oxidation parameters cannot be accurately duplicated. Therefore, it is often assumed that the oxidation kinetics is perfectly parabolic for ease of comparison between experiments [*44*]. Nevertheless, oxidation kinetics provides a way to semi-quantify the growth rate of oxides and provides a measure of how rapidly the material is deteriorating from the consumption of beneficial elements. Hence, knowledge of the kinetics can be a useful tool for prediction of the operational life of a component if used to complement thermodynamic analysis. However, thermodynamic and kinetic processes may not be the only mechanisms operating in an alloy during high temperature exposure. For instance, creep, thermo-mechanical fatigue and oxide growth stresses may also play a roll in oxide/alloy damage [*3, 23, 25*].

2.3.5 Oxide Growth Stresses During Oxidation

Thermodynamic and kinetic analyses provide information regarding the stability and rate of oxide formation during high temperature exposure, as discussed in Sections 2.3.3 and 2.3.4. However, thermodynamics and kinetics are not the only mechanisms that determine how long, or even if the scale will remain attached to the metal. If the oxide that forms is stable, dense, adherent and slow growing, the material may still be left unprotected if the oxide scale is unable to withstand the stresses associated with external applied loads and internal stresses produced by the oxidation process itself. These internal stresses, commonly referred to as oxidation or growth stresses, can arise from many different sources, some of which are outlined in this section.

Stress Due to Differences in Volume:

Differences in volume occur in any changes in state or phase. As such, the oxidation of metal to form various oxides at the metal/oxide or oxide/gas interface results in various changes in volume, which depend on the type of oxide produced. Pilling and Bedworth were the first to attempt to understand how metals react with gaseous environments, and were the first to quantify the change in volume associated with the oxidation of metals [*25*]. This led to the development of the Pilling-Bedworth Ratio given in Equation (12) [*3, 23, 25*]:

$$PBR = \frac{V_o}{V_m} \tag{12}$$

where PBR is the Pilling-Bedworth Ratio, V_o is the volume of the oxide and V_m is the volume of the metal consumed. If the ratio was less than one, the oxide scale was said to be unprotective with tension stresses resulting from the volume decrease; if it was greater than or equal to one, the oxide scale was said to be protective since the oxide had a larger volume than the metal and therefore was able to completely cover the metal and slow down oxidation. Compressive stresses dominate in this instance. If the ratio was larger than 2, the oxide was growing at the metal/oxide interface and large compressive stresses would develop, leading to early spallation of the scale [*3, 23, 25*].

The PBR, being a simple model, was not very accurate in the prediction of protective and non-protective oxides. Firstly, the assumption of inward diffusion of oxygen ions is primarily the reason for this method's dismissal. Many studies have shown that most oxides grow by outward diffusion of the metal ions to the oxide/gas interface. Additionally, this theory did not account for other mechanisms, like stress relief, making it a very simplistic approach for determining how protective an oxide is and how long the life of the oxide will be [*23, 25*].

Stress Due to Compositional Changes:

Compositional changes can result in the creation of stresses within the alloy or oxide scale by several different mechanisms. First, selective oxidation can cause changes in the lattice parameters of the alloy, resulting in small volume changes within the substrate material itself. As more elements are selectively oxidized, these stresses increase and may cause voids or sites where microcracks can form. Similarly, the products of the selectively oxidized elements can result in volume changes, thereby introducing additional stresses in the material. Again, as the formation of these compounds increases, the stresses increase which may lead to cracking or spallation of the oxide scale [*25*].

Thermally Induced Stresses:

If the relative stresses in the oxide or base material are low, the oxide scale may remain attached so long as these growth stresses do not increase and there is no change in the external applied load. However, upon changing temperature, differences in the coefficient of thermal expansion (CTE) may result in extremely high thermal stresses between the oxide and base material or between different oxides. Typically, these stresses cause extensive spallation of the oxide scale upon cooling. More discussions regarding how thermally induced stresses in nickel-based superalloys are presented in Section 2.5.1 [*23*].

2.4 Types of Protective Coatings

As outlined above, the composition and type of protective coating may vary depending on the application in which the base material is to be used. Since the early gas turbine engines, there have been many developments in the area of protective coatings in order to produce coatings that will extend the life of the base material, while not compromising any of the mechanical or chemical properties of the substrate being protected. As such, many different coating deposition processes have also been developed in order to maximize the efficiency of the deposition processes and to control the properties of the coated material. The next sections outline three types of protective coatings, diffusion, overlay and TBC. The numerous types of deposition processes and their effect on the properties and performance of the protective coatings are not apart of this work. However, some common deposition methods are given for each coating type for general comparison purposes.

2.4.1 Diffusion

Diffusion coatings, like their name suggests, are coatings that form due to the interdiffusion of the coated material, usually Al or Cr, and the base material that will eventually form a protective oxide layer to prevent hot corrosion and oxidation [*3*] [*36*]. Diffusion coatings usually have better fatigue characteristic when compared to overlay coatings [*45*].

Most of these types of coatings today are formed by Chemical Vapor Deposition (CVD) process. This gas phase aluminide coating process replaced the traditional pack cementation processes in 1977 when Pratt and Whitney introduced gas phase coating to protect internal air-cooling systems. This allows complete coverage of a part by the diffusion coating, including internal air-cooling ducts on modern turbine blades, by passing a reactive gas through and over the turbine airfoil [*36, 45*]. A benefit of this process is the precise control of the CVD system allowing several elements to be added into the coating in trace amounts. CVD processes are also very clean, allowing for less contamination of the coated material and improving oxidation resistance [*36*]. In Ni-based superalloys, diffusion coatings can be classified as inward diffusion types, which are those where Al or Cr moves into the substrate material due to lower Al concentrations in the substrate, and outward diffusion types, where Ni in the base material diffuses into the coating due to lower Ni concentrations in the coating [*1*].

2.4.2 Overlay

Between mid 1960's and mid 1970's an innovative new type of protective coatings was developed. The new coatings were the MCrAlY type (where M represents Ni, Co or Fe), or overlay coatings, as they are more commonly known [*3*] [*45*]. Unlike diffusion coatings, these coatings can be developed independent of substrate composition since they do not rely on the diffusion of substrate and coating elements to form a protective layer, allowing them to be customized to many different applications [*1*]. For example, higher Cr content allows for better protection against Type II hot corrosion, while higher Al content allows for protection against Type I hot corrosion [*36*]. Unlike diffusion coatings, overlay coatings do not require diffusion between the coating and substrate to form an oxide. Therefore, there is a reduction in the incorporation of unfavorable elements from the substrate (like Ti) in the formation of the oxide layer, increasing the oxidation and hot corrosion protection [*45*].

Overlay coatings are commonly deposited on the substrate material using electron beam physical vapor deposition (EB-PVD) or more recently through low pressure plasma spraying (LPPS), between 150-300 μm in thickness. The latter method has proven to be faster and simpler permitting automation for high volume coating application such as turbine blade manufacturing [*1, 3, 45*]. A more in-depth look at the deposition techniques of overlay coatings is presented in Section 2.6.

Although overlay coatings have 4-5 times better oxidation protection, when compared to diffusion coatings, they do have their limits. Overlay coatings are highly susceptible to TMF.

TMF is unavoidable in jet engine applications and is a result of the varying shape and cross-section of the turbine blades and changes in temperature resulting from variations in engine power. Temperature changes can vary from 1100 °C at the leading/trailing edge of the turbine blade to 650 °C at the center of the blade [*36*]. Increasing the engine power will increase the temperature gradient experienced by the turbine blades. Since the thin sections will heat up faster as compared to thicker sections, the subsequent expansion of the thin cross-section will be constricted by the slow expansion of the thicker cross-section resulting in compressive stresses. The opposite effect will happen when the engine power is reduced. The difference in expansion of the turbine blades results in thermal fatigue stresses. A combination of these thermal stresses with high rotational loading and vibrations leads to TMF.

The change from polycrystalline materials to single crystals was brought about to reduce the deformation experienced by the base material in order to reduce the effects of TMF on the overlay coating [*1, 45*]. The presence of a temperature gradient also results in differences in the types of hot corrosion experienced by the blade geometry

[*36*]. Fortunately, overlay coatings are very tailorable in their composition and can accommodate these variations.

Due to their ability to be tailored to specific applications, overlay coatings have advanced into a unique form of protective coatings that can adapt to specific changes in heating conditions to provide protection against both Type I and II hot corrosion. These types of coatings are called SMART overlay coatings. The principals behind SMART coatings are the treatment of an overlay coating to form an intermediate Cr rich zone. Exact methods to manufacture such coatings are proprietary but the following paragraph outlines the basic concept behind SMART coatings [*3*].

Under high temperature conditions, like those seen in Type I hot corrosion or high temperature oxidation, the SMART coating forms a protective aluminum oxide layer, which provides maximum protection from such environments. At this point the Cr rich intermediate layer acts as a diffusion barrier for Al trying to diffuse into the substrate and slows the diffusion of Al from the substrate into the coating. Under lower temperature conditions, like those needed for Type II hot corrosion, the slowly forming alumina layer is destroyed allowing the harsh environment to reach the Cr rich intermediate layer. At this point, a chromium oxide will form to continue to protect the substrate material [*3, 18*]. SMART coatings can also repair themselves if the protective coating is damaged, so long as there is a sufficient level of Cr or Al to form a continuous oxide barrier [*18*].

2.4.3 Thermal Barrier

Thermal barrier coatings are attractive for use in high temperature applications, particularly on gas turbine blades, since they create a substantial reduction in temperature at the metal surface while protecting the base material from high temperature oxidation and hot corrosion. This is achieved by applying a ceramic layer on top of a diffusion or overlay coating through thermal spraying or EB-PVD [*36, 46*]. Reduction in temperature can reach 170 ℃ for most modern thermal barrier coatings in high temperature environments [*1, 36*]. This means the turbine inlet temperature (TIT) can be increased, resulting in an increase in engine efficiency [*3*] [*45*]. The smoother the surface of the TBC, the higher still the thermal protection, due to the formation of a boundary layer at the surface of the coating and the hot gases [*45*].

Despite the substantial thermal protection, there are limitations to TBC's. After prolonged exposure to high temperatures, 'peg' like structures can form in the TGO/coating interface or in the TGO/substrate interface. At the tips of these peg structures are areas of increased stress. With any change in temperature or other stress inducing processes, the tips of the pegs will cause stress concentration resulting in crack initiation and propagation in the direction parallel to the surface of the metal. Continued cracking will result in the spallation of the ceramic topcoat thus exposing unprotected metal [*7, 8, 9, 10, 11*]. Since temperatures are usually increased in applications protected by TBC's, spallation of this ceramic layer will subject the base material to higher than normal temperatures, resulting in faster oxidation/failure if protective oxides cannot be formed [*45*].

2.5 Failure Mechanisms and Degradation of Coatings

As mentioned earlier, overlay coatings provide extended protection from oxidation and hot corrosion, thereby extending the life of turbine blades. However, eventually the protective coating, in particular the oxides that form, will degrade to the point where they can no longer protect the substrate material. The point at which the coating can no longer protect the substrate is adequately termed the failure point. There are several mechanisms that lead to coating failure. It is important to note that it is highly unlikely that only a single mechanism is the cause of coating failure. Rather, it is more likely that most or all of these mechanisms have an effect on the coating's performance at some point during high temperature exposure. Since each mechanism is highly sensitive to the elements present and their relative concentrations, as well as the oxidizing environment, surface conditions and phases present, one or more mechanisms may contribute more to coating failure than the others. It is therefore important to understand which failure mechanisms are in play and how the coating can be altered through various additions or alterations in the composition of both the alloy and coating in order to extend the endurance of the coating material [*4-6, 12, 17, 20, 27-31, 35, 47-49*]. Some of the primary coating failure modes are discussed in the following sections.

2.5.1 Coefficient of Thermal Expansion (CTE) Mismatch

In alumina forming coatings, CTE mismatch, along with the reduction in volume between the transient and stable forms of alumina as described in Section 2.3 are the primary cause of spallation from the coated material. The reduction in volume leads to the formation of tensile stresses within the oxide. As these stresses increase through the change in operating temperature, the difference in CTE will cause the high stresses in the regions of volume change to move past the critical value. As a result, crack nucleation and subsequent coalescence of crack sites will result in the spallation of the oxide layer [*5, 9, 15, 17, 44, 47*]. In addition, any additional stresses introduced into the system, like increase in mechanical loading or growth stresses, will also result in crack formation along the regions of high thermal stresses [*3*]. Needless to say, the formation of α-Al_2O_3 can be both beneficial and detrimental to the health of the coated system. In addition, the formation of needle-like precipitates (σ-phase) or needle α-Al_2O_3 will also result in a region of high stresses, particularly at the tips of the needles. If these phases precipitate within or near areas that have experienced volume changes, or undergo significant temperature changes, the increased stress will result in spallation of the oxide [*3, 12, 15, 17, 19, 47*].

2.5.2 Depletion of Oxide Forming Elements

Depletion of protective oxide forming elements like Cr and Al is another common failure mechanism [*20, 47*]. Since α-Al_2O_3 is stable and protective at high temperatures, it is critical that significant Al remains in the substrate and/or coating to form and heal the oxide scale. However, selective oxidation of Al at the surface will deplete Al reserves, resulting in the inability of the material to form new protective oxides after spallation has occurred. The Al depletion process is accelerated if the coating is continually subjected to conditions that result in continuous and rapid spallation of the protective oxide and subsequent re-formation of new oxide layers (like cyclic thermal loading in aircraft gas turbine engines). Accelerated usage of the Al reserves has the potential for unexpected catastrophic failure of the turbine blade [*47*].

Diffusion rates can be changed through the addition of reactive elements (RE), like Re, Y, Hf, Zr, Ta and Pt to stabilize the scale adherence or slow the rate of inward diffusion of oxygen or outward diffusion of Al. Furthermore, the formation of undesirable phases, such as tcp phases or carbides may use up important RE like Ta, Mo, Ti, thereby accelerating the diffusion of Al [*5, 6, 15, 28, 30, 47-49*].

2.5.3 Wrinkling/Rumpling of the Interface Between the Substrate and Coating

Rumpling or wrinkling of the surface appears as large undulations at the surface of the overlay coating when exposed to thermal cyclic conditions. The effect of rumpling between the substrate and coating can be attributed to the initial surface condition of the substrate, thickness of the coating and the composition of the coating itself. However, the exact mechanisms by which rumpling occurs is still largely distributed but it is generally accepted that temperature and the number of cycles are primary contributors to the degree of rumpling observed [*20, 50, 51*].

This type of failure can be reduced by proper treatment of the substrate surface before coating application, and properly tailoring the coating composition to reduce the rumpling effect [*20*]. Minor additions of Hf and C have shown to improve the resistance to rumpling by increasing creep resistance and strengthening of the alumina scale [*31*].

2.5.4 Surface Roughness

Surface roughness is important for some applications in order to increase the mechanical bonding between the substrate and the deposited coating, but it can also have a detrimental effect on oxidation characteristics [*3*]. Experiments by Gil *et al.* [*12*] have shown that surface roughness, used to increase the mechanical adhesion of some coatings, may also enhance the rumpling effect and the eventual degradation of the coating leading to early spallation. The study showed the convex areas of a rough surface have higher rates of Al depletion due to the greater surface to volume ratio. In addition, Y-Al oxide pegs were also formed in these regions, thus creating higher stresses resulting in the potential for failure [*12*].

2.5.5 Buckling

Buckling of the oxide scale occurs at the coating/oxide interface when the oxide is relatively strong and the coating/oxide interface is relatively weak [*3*]. The exact initiation mode for buckling is not well understood, however recent work by Evans *et al.* [*52*] has shown that minor undulations or rumpling of the oxide/metal interface with compressive stresses within the oxide scale contribute significantly to the initiation of buckling [*52, 53*]. Upon reaching a critical compressive stress, buckling is initiated, where the buckling mechanisms have been shown to progress along a similar sequence as shown in Figure 2 [*52, 53*]. The critical stress to produce the initial stages of the buckling sequence for elastic conditions is described by Equation (13) [*53*].

$$\sigma_{cr} = \frac{1.22E_{ox}}{1-\upsilon_{ox}^2}\left(\frac{\xi}{R_{deco}}\right)^2 \tag{13}$$

where σ_{cr} is the critical stress to initiate buckling, E_{ox} is Young's modulus of the oxide, υ_{ox} is Poisons ratio of the oxide, ξ is the oxide thickness and R_{deco} is the radius of the area of decohesion. The sequence taken has been shown to be dependent upon the mechanical properties of the coating/oxide and the base material. TABLE I summarizes the relation between the buckling mechanisms and the material properties [*52*].

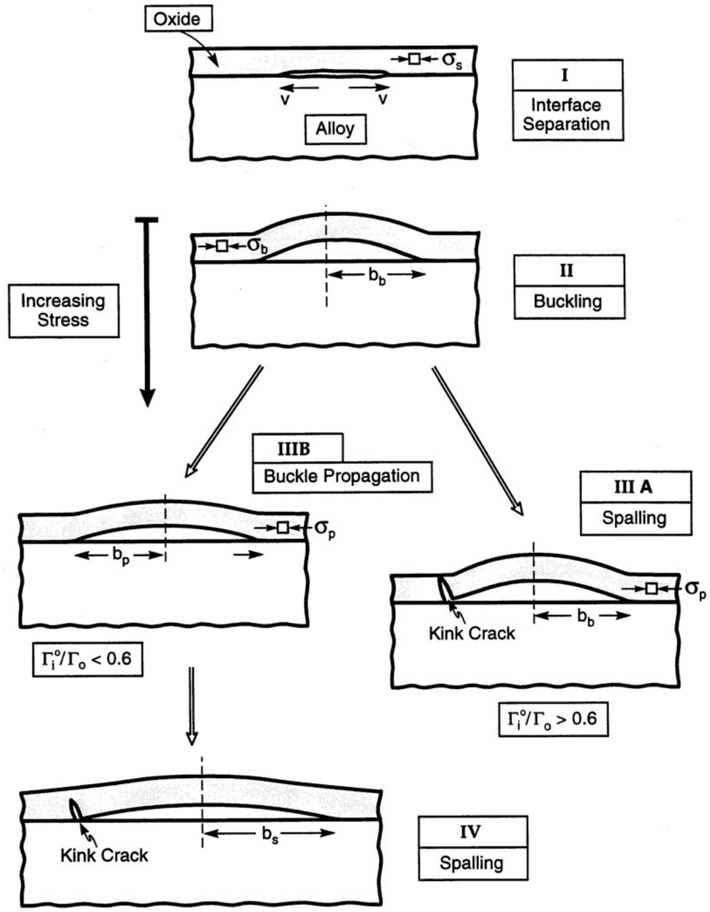

Figure 2: Sequence of buckling events in thin films under compressive loading. Taken from [*52*]. Reprinted with the permission from Elsevier.

TABLE I: BUCKLING MODES OF THIN COATINGS/OXIDES UNDER COMPRESSION LOADS [*53*].

Film	Substrate	Condition of Interface bonding	Buckling Mechanism
Brittle	Ductile	Good	Buckling propagates within film
		Bad	Buckling propagates at interface
Brittle	Brittle	Good	Buckling occurs in substrate (substrate splits)
		Bad	Buckling propagates at interface

From Equation (13) a strong dependence on coating/oxide thickness and decohesion area is observed. For thinner coatings and oxides, the critical stress to induce buckling is lower, and therefore buckling of a thin film is initiated easier. This is also true for larger regions of interface decohesion. However, for high critical stresses typically generated in thicker films and smaller decohesion regions, an alternative mode of coating/oxide failure is observed. This mode of failure is commonly known as wedging [*52, 53*]..

2.5.6 Wedging

For stronger interface adherence relative to coating/oxide properties, typically observed with thicker films and smaller regions of decohesion, wedging is a dominant failure mode [*3, 52, 53*]. Initially, compressive shear cracking of the coating/oxide occurs at pre-existing defects like voids or regions of high stresses. Further stressing, either from volume changes associated with CTE mismatch or external loading, drives the initial cracks down to the interface where localized decohesion occurs. Figure 3 illustrates this process. Continued loading results in a wedge-like section of the coating/oxide to be driven out of the film.

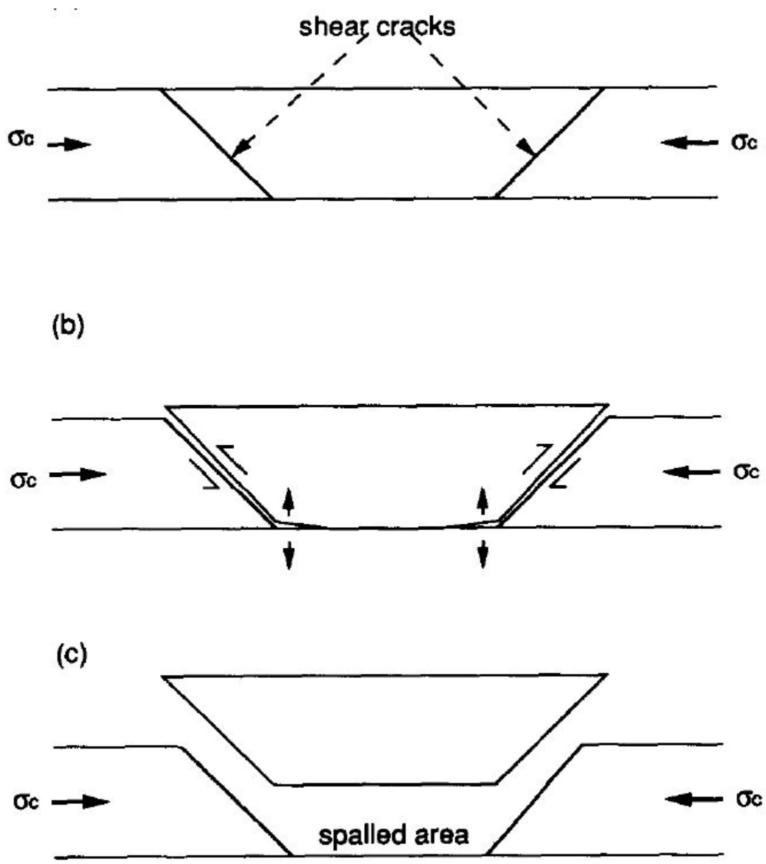

Figure 3: Schematic illustrating the stages of wedge cracking of a thin film under compressive stresses. Taken from [*53*]. Reprinted with the permission of Elsevier.

As with buckling, the critical stress for wedging failure can be developed from a fracture mechanics perspective assuming elastic behavior. Equation (14) describes the critical stress to initiate wedging [*53*].

$$\sigma_{cr} = \frac{K_{IC}^{Cr}}{\sqrt{(\xi)}} \tag{14}$$

where σ_{cr} is the critical stress, K_{IC}^{Cr} is the critical fracture toughness for mode one fracture, and ξ is the coating/oxide thickness. The academic community has criticized this model because it does not take into account the size or geometry of the defects in the material. Other models using an energy balance approach have since been developed, but they too have been seen as overly simplified [*53*].

2.5.7 Foreign Object Damage

The last mode of failure is something that cannot be avoided. Foreign object debris is always a concern, particularly with TBC systems. Foreign object damage (FOD) can result when debris impacts the turbine blade causing an indentation on the blade surface. This indentation can result in a local hotspot causing internal oxidation of the substrate material and eventually leading to failure of the blade. However, steps can be taken to reduce the amount of debris that is ingested by the gas turbine engine, such as intake alterations, regular maintenance and a debris 'free' operating environment [*3*].

2.6 Deposition Processes of Overlay Coatings

As previously mentioned, overlay coatings do not rely on substrate/coating interactions to form a protective layer. This allows for coatings to be specifically tailored to any application and opens up the possibility to deposit more difficult-to-deposit reactive elements such as Y and Hf. There are many different techniques that are used to deposit overlay coatings, however physical vapor deposition (PVD) techniques are commonly used. A graphical representation of some deposition techniques is shown in Figure 4 and a comparison of various processing parameters for several deposition techniques are summarized in Table II.

Since each process deposits the coating under different conditions, there is variability in coating properties; consequently each coating will perform differently when subjected to corrosive or high temperature environments. It is therefore important to know how each process affects the deposited coating properties, and how subsequent exposure to harsh environments will react with the deposited materials, which are discussed in literature [*23, 54*].

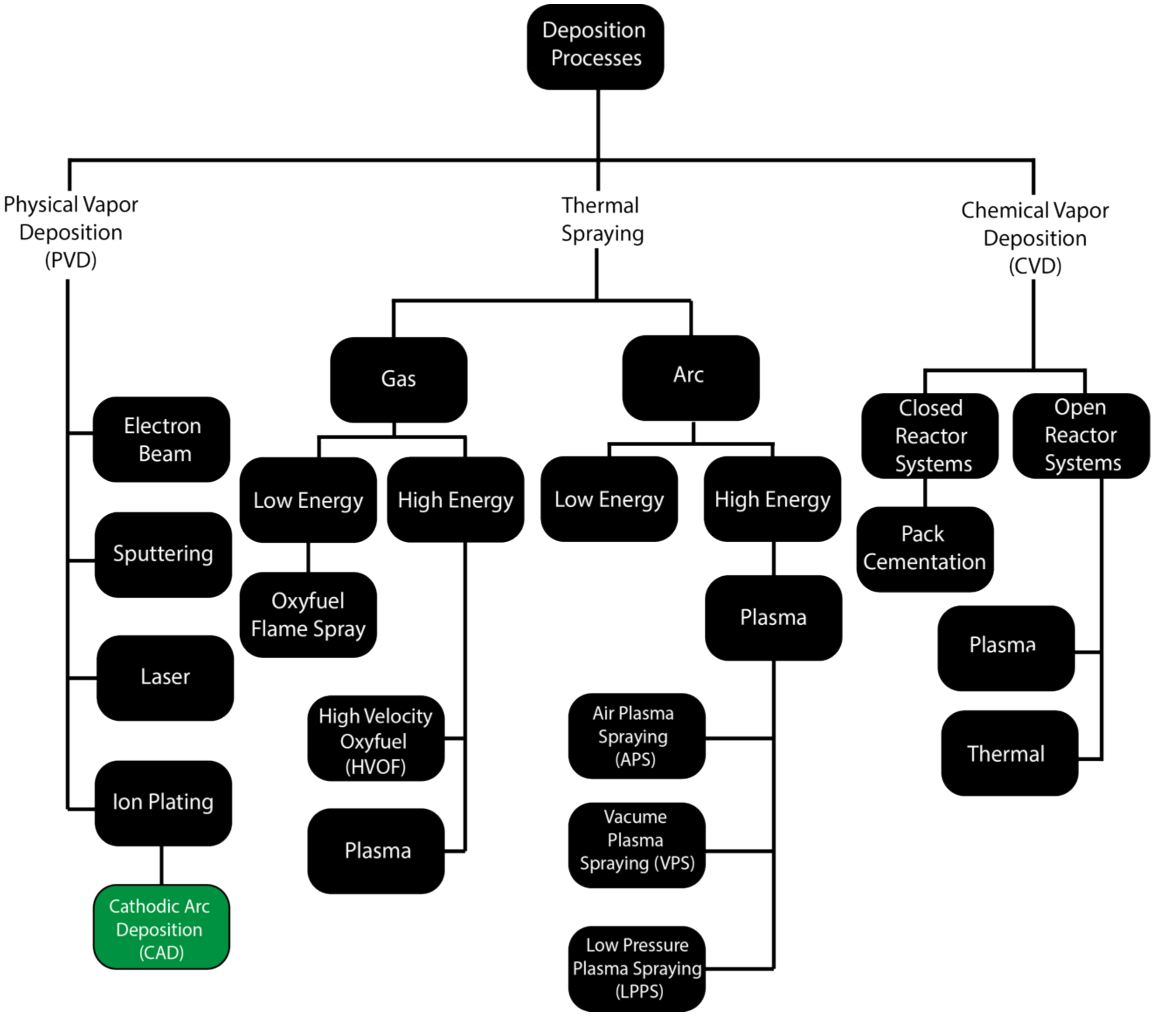

Figure 4: Some commonly used deposition processes for overlay coatings. The process used for coting material in this work is indicated by a green background [*23, 54*].

Table II: Comparison of various processing parameters for some coating techniques [*54*].

Process	Thickness (μm)	Surface Hardness (HRC)	Corrosion resistance	Line-of-Sight	Substrate Temperature (℃)	Processing Pressure (kPa)	Processing Time (hrs)
CVD	1 - 1300	0.04 - 50	Very Good	No	820 - 1200	0.013 - 10	10 - 60
PVD	0.025 - 10	0.001 - .04	Excellent	Yes	200 - 540	10^{-8} - .013	1 - 10
Thermal Spraying	100 - 2500	50 – 100 (WC)	Excellent	Yes	95-260	atm	1 – 10 (>10 for large areas)

This section outlines some of the frequently used deposition methods. Some of the applications of each method, the advantages and disadvantages, as well as general set-up and processing parameters for each method are discussed.

2.6.1 Electron Beam PVD

One of the common methods of coating substrate materials is through the use of electron beam physical vapor deposition (EB-PVD). This technique, like the name implies, uses an electron beam to vaporize the coating material. The use of an electron beam allows for greater control over the vaporization process, as well as allows for the beam to be manipulated for impingement around corners making it a non-line of sight technique. The coating material, especially alloy coating materials, must have elements that have relatively the same evaporation rates in order to ensure proper compositional control of the deposited coating. If the relative evaporation rates are too dissimilar, alternative allowances must be made to create the proper coating composition. Typically, MCrAlY coatings have shown to be successful using this technique [*23, 55*].

The EB-PVD process starts by placing the specimen in a vacuum chamber where the pressure is reduced to below 13 mPa. Once the pressure has been reduced to specified amounts, using 10 to 20 kV, the electron guns are directed to impinge on ingots made up of the coating material, known as targets. Vaporization of the coating material occurs while using 10 to 50 kW of power. This vapor is then directed towards the substrate material where it is condensed to form a columnar structure on the substrate surface. Deposition rates are relatively high, up to 50μm/sec have been reported and vaporization rates can be as high as 10 – 15 kg/h for some target materials [*55*].

Tight process control and large specialized equipment make this technique one of the most expensive ones to operate. However, if control of coating composition and microstructure is required, EB-PVD is the preferred technique. Most often, this is the preferred technique for TBC systems rather than overlay coatings since multi coating layers can be deposited simultaneously [*55*].

2.6.2 Thermal Spraying

Thermal spraying is a general term used to describe a cluster of processes that apply coatings by vaporizing, atomizing, or by production of finely dispersed molten globules of coating material. TABLE III provides a summary of the distinctive processing parameters of several different thermal spraying processes.

TABLE III: COMPARISON OF VARIOUS THERMAL SPRAY PROCESSING PARAMETERS [54].

Process	Gas Temp. (℃)	Particle Velocity (m/s)	Adhesion (MPa)	Oxide Content (%)	Porosity (%)	Spray Rate (kg/h)	Relative Cost	Deposit Thickness (mm)
Flame	3000	40	8	10 – 15	10 – 15	2 – 6	Lowest	0.1 – 15
Arc Wire	N/A	100	12	10 – 20	10	12	Low	0.1 - >50
HVOF	3000	800	>70	1 – 5	1 – 2	2 – 4	Medium	0.1 - >2
Det. Gun	4000	800	>70	1 – 5	1 – 2	.5	N/A	0.05 – 0.3
APS	12000	200 - 400	4 - >70	1 – 3	1 – 5	4 – 9	High	0.1 – 1
VPS	12000	400 - 600	>70	ppm	<.05	4 – 9	Highest	0.1 - 1

Thermal spraying is one of the most versatile coating deposition processes and can be used to coat almost any coating material (ceramic, metal, plastic). Typically, spraying is done with a cold substrate, which ensures the substrate will not be distorted or endure any microstructural changes or physical degradation during the spraying process. Reduction in microstructural changes during processing is essential, since any alteration in microstructure will have an effect on the mechanical properties of the material at elevated temperatures [*54, 55*].

One of the significant drawbacks to this process is that the deposition is limited to line of sight, often requiring manipulation of the coating vapor plume to coat the entire surface. In addition, lower energy techniques like flame spraying rely heavily on mechanical bonding of the deposited coating. Therefore, the substrate must be perfectly clean and suitably rough to ensure good adhesion. Also, lower energy techniques produce coatings that have relatively high porosity, which can be problematic for proper corrosion or high temperature oxidation protection. However, problems with porosity and adhesion are often solved by using higher energy techniques such as APS, VPS, LPPS and HVOF [*54, 55*].

The general process of thermal spraying starts by creating a vaporized plume of coating material. This can be achieved by two separate methods, electric arc or gas combustion. In electric arc, two oppositely charged rods with the composition of the coating material are brought together to generate an arc with very high temperatures, thus a creating molten material. This material is subsequently atomized in a carrier gas and directed to the substrate forming a high velocity jet. In the gas combustion process, a combustible gas is fed into a chamber where it is heated by an electric arc. Subsequent combustion and continued heating create high velocity plasma that melts and carries the coating powder to the substrate material. Gas combustion processes can also use lower energy oxyfuel combustible gas to achieve the same effect during flame spraying. A schematic of a typical plasma torch used for thermal spraying is shown in Figure 5 [*54, 55*].

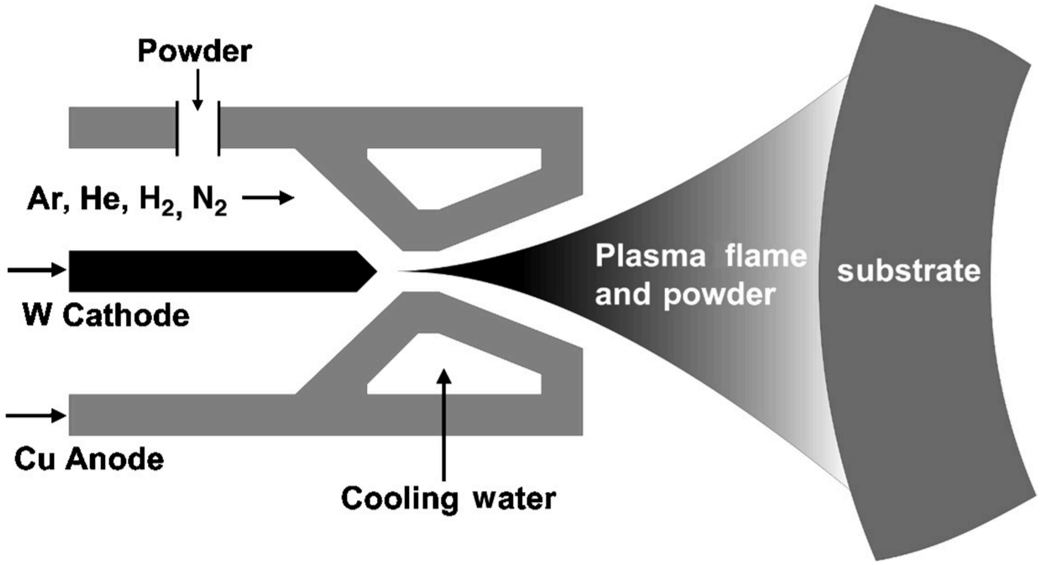

Figure 5: Schematic of a typical plasma torch used for thermal spraying. Taken from Introduction to the High Temperature Oxidation of Metals [*23*]. Reprinted with the permission of Cambridge University Press.

The mechanical properties, such as wear rates, corrosion resistance and hardness of the as-deposited coating depend on the porosity of the final product but also more significantly depend upon the deposited glob/glob and the glob/substrate interfaces, morphology of the globules and composition of the coating. Subtle changes to one or more of the processing parameters may have great influence on the final properties of the coating material. For this reason, there is no universal catalog for coating parameters and final product. Therefore, it is necessary to develop an optimum coating process for each system (coating and substrate material) through proper experimental trials to ensure the effectiveness of the coated material for any given application [*54, 55*].

2.6.3 Cathodic Arc Vapor Deposition Method

Cathodic arc vapor deposition method, also known as cathodic arc deposition (CAD), was used to apply the coatings to the substrate material in this project. This method is a commonly used deposition technique that falls in the ion-plating category.

In CAD deposition a metal cathode (also known as a target), which has the composition of the material to be coated, is inserted into the equipment along with the substrate to be coated. Once all the materials have been properly secured in the equipment, the deposition chamber is evacuated of air. An arc is then produced and made to strike the cathode surface with very high current and power densities of 10^{12} A/m^2 and 10^{13} W/m^2, respectively [*56*]. These localized arcs, typically as small as 1

μm, are called cathode spots, which are usually very short lived (sub-nanosecond) but have sufficiently high temperatures to fully vaporize the target material into an ionized plasma plume [*56*]. The plasma plumes rapidly expand into the vacuum chamber in the order of 1 – 2 X 10^4 m/s (10 – 20 km/s). These high velocity plasma particles are then directed to impact the substrate material through the use of magnetic fields and voltage bias placed on the substrate material [*56*].

Since the arcs vaporize any material contained on the surface or within the target material, there is a small amount of contamination that may enter the plasma plume during the coating process. In addition, some material may not fully vaporize, resulting in small molten/semi-molten droplets. Therefore, filters are often used to remove these droplets, which typically range in size between .1 and 10 μm, from the plasma, [*56*]. Filtering of the plasma is possible through some manipulation of the plasma stream through the use of magnetic fields. This is achieved by bending the plasma with a magnetic filed inside a solenoid. The multiply charged ions will follow the magnetic filed, and pass through the solenoid to be deposited on the substrate, while the heavier droplets and unwanted contaminants will not be able to follow the curvature of the plasma stream due to their higher mass to charge ratio [*56*]. Figure 6 shows an example of a typical plasma filter used in CAD systems.

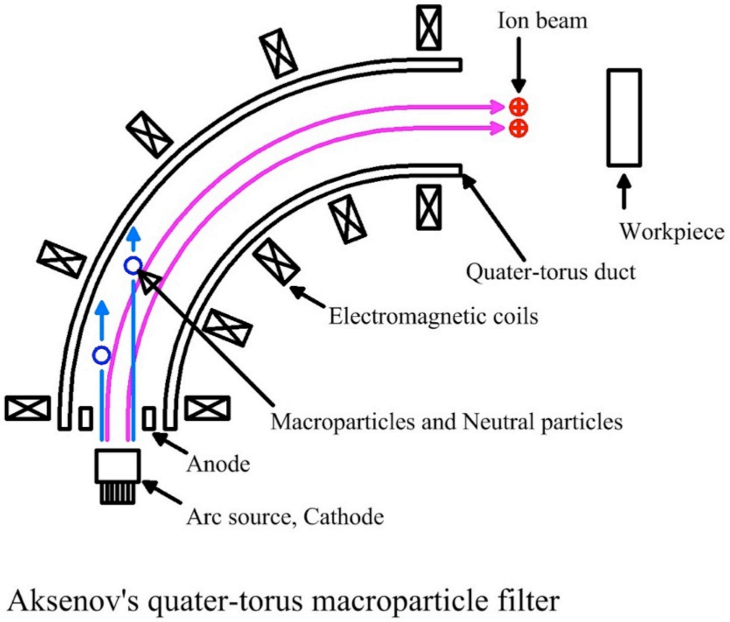

Figure 6: Illustration of an Aksenov Quarter-torus filter used in CAD [57].

In addition to plasma filtering, the ability to control the path of the plasma plume from the target to the substrate leads to the enhancement of coating uniformity and coverage. When path control is coupled with various operational modes like pulsed or continuous operation, high deposition rates and part throughput can be achieved. The CAD technique has the ability to deposit many different coating materials with excellent film properties and controllability making it a very versatile application technique for industrial purposes.

3.0 Experimental Procedure

This section outlines the experimental procedure used for isothermal oxidation testing at 1100 °C for both the un-coated and coated samples. This section includes discussion on sample preparation of the base material and experimental set up prior to oxidation. Also, the oxidation equipment and processes are outlined and discussed. Finally, the characterization techniques, including equipment and theoretical methods used, are described.

3.1 Sample Preparation

In this section the sample preparation of the un-coated and coated materials are discussed. Some of the specifics that are included are base material preparation prior to oxidation and/or coating, dimensions and composition of the base material used, as well as pre-oxidation heat treatments performed.

The nominal compositions of typical CMSX-4 and CMSX-486 in the as-cast condition are given in TABLE IV along with the composition of the coating target material. All samples used in this work were created from the same bar of as-cast material to minimize the effects of variation between casting batches. Micrographs of the as-cast alloy are show in Figure 7 and Figure 8.

TABLE IV: COMPOSITIONAL DATA OF CMSX-4 AND CMSX-486 NI-BASED SUPERALLOYS AND COATING, COMPOSITION GIVEN IN WT% .

Alloy	Ni (Base)	Co	Cr	Ta	W	Al	Re	Ti	Mo	Hf	C	B	Zr
4[†]	**61.8**	**10.0**	**6.0**	**6.0**	**6.0**	**5.6**	**3.0**	**1.0**	**.6**	**.1**	**-**	**-**	**-**
486[‡]	**63.0**	**9.3**	**5.0**	**4.5**	**8.6**	**5.7**	**1.2**	**.7**	**.7**	**1.2**	**.07**	**.015**	**.005**
Coating	**80.0**	**-**	**5.0**	**-**	**-**	**15.0**	**-**	**-**	**-**	**-**	**-**	**-**	**-**

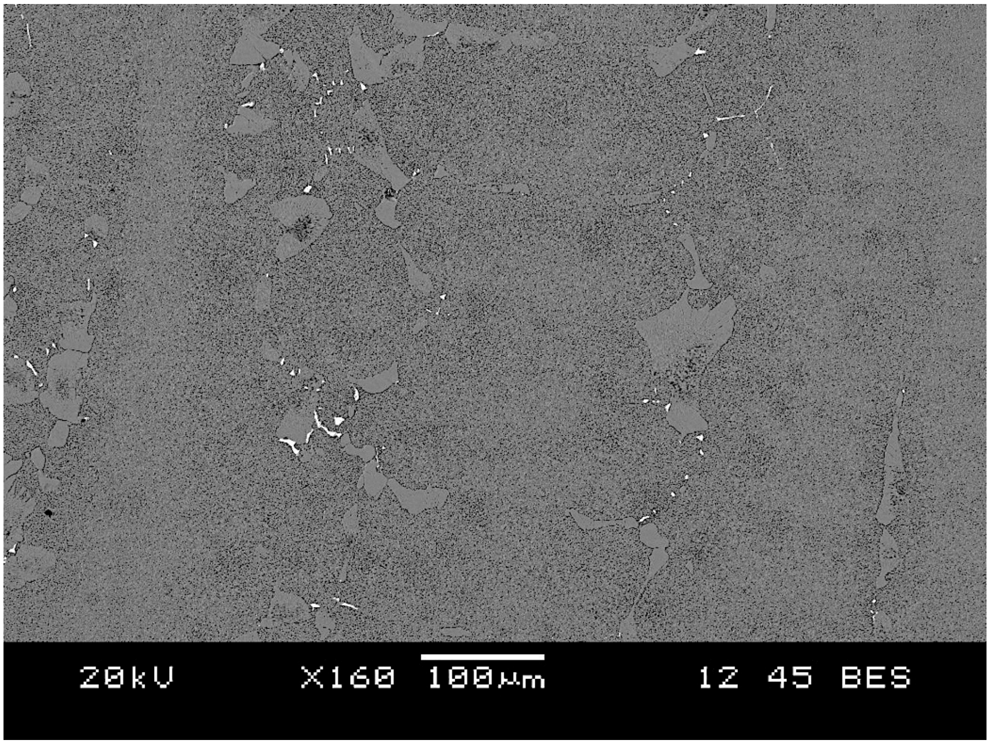

Figure 7: Backscattered image of CMSX-4 in as-cast condition. Minor carbides, (the bright particles) were observed in the microstructure.

[†] CMSX-4

[‡] CMSX-486

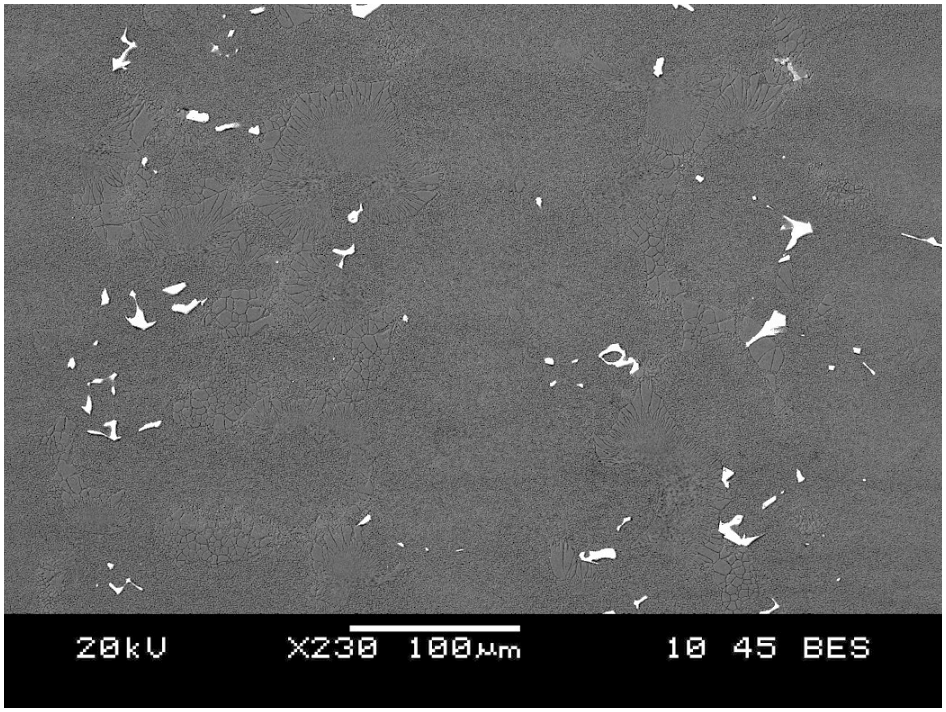

Figure 8: Backscattered image of CMSX-486 in as-cast condition. Larger carbides are indicated as white spots.

Minor Ta-rich carbides were present in CMSX-4 while the carbides had a greater presence in CMSX-486 in the as-cast condition. However, CMSX-486 also showed a few localized Hf-rich intermetallic particles at the ends of eutectic products. Additional heat treatments were performed on the as-cast material as outlined in the following sections.

3.1.1 Un-Coated Sample Preparation

The un-coated CMSX-4 and CMSX-486 samples were prepared from an as-cast bar approximately 12mm in diameter. Each sample was cut using a Hansvedt DS-2 traveling wire electrical discharge machine (EDM) to an approximate thickness of 3mm, creating a 3 mm thick by 12mm diameter disk as shown in Figure 9.

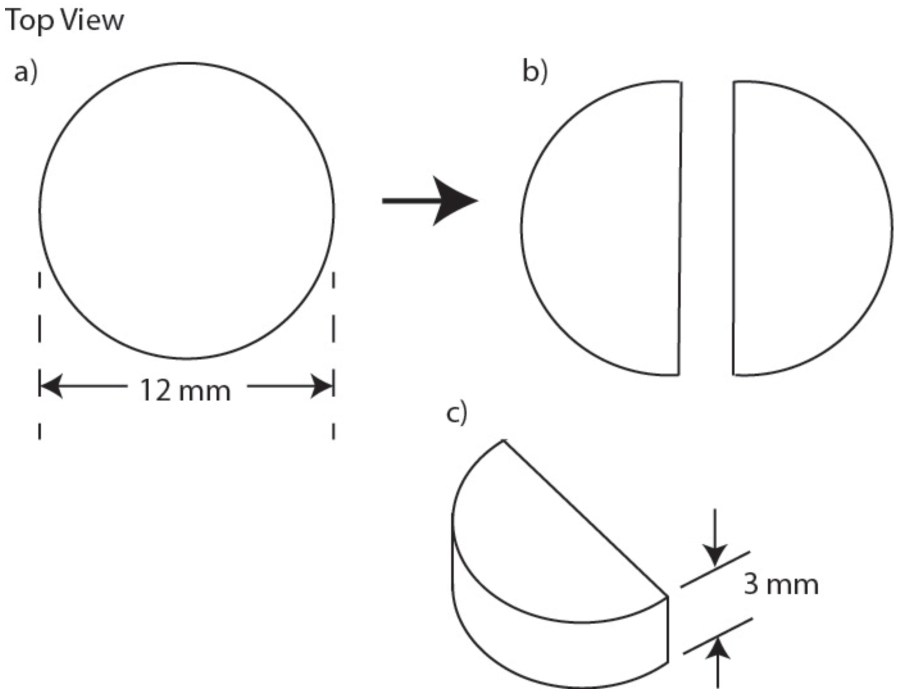

Figure 9: Schematic diagram of the specimen geometry used for the isothermal oxidation test. a) Top view of as-cast bar prior to cutting into sample size. b) Top view of sample after it has been cut from as-cast bar into two separate samples. c) 3D view.

Each disk was then cut into half (creating a half disk), which was used as a test sample. Each sample was ground to 600 grit to remove all surface oxides and ultrasonically cleaned in ethanol for 10 minutes to remove any oil or residue that may have contaminated the sample during the cutting and grinding processes.

3.1.2 Coated Sample Preparation

As-cast material was heat treated before sample preparation commenced. The heat treatment for CMSX-4 included 1305 °C for 6 hrs, followed by air cooling; as for CMSX-486, the heat treatment consisted of 1238 °C for 1 hr, 1243 °C for 1 hr and 1249 °C for 1 hr followed by air cooling. Preparation of the specimens to be coated with Ni-5Cr-15Al overlay coating initially followed the same procedure as the un-coated samples described in Section 3.1.1 for sample cutting and grinding. One surface of the samples were then polished using 1 micron colloidal diamond solution. Once initial preparation was completed, 30 samples of each alloy were sent to the National Research Council of Canada (NRC) located in Ottawa, Ontario, to undergo cathodic arc PVD process to apply the Ni-5Cr-15Al-coating.

Prior to insertion of the samples into the coating jig, all the samples were cleaned with acetone + anhydrous ethanol solution to remove any oil or residue on the samples. The deposition process consisted of two stages. The first stage was plasma cleaning to remove any contaminants left on the surface that prior cleaning stages did not remove. The next stage was the coating deposition stage. The process parameters for each stage are summarized in TABLE V.

During the cleaning and deposition stages, 30 samples of each alloy were held in a special jig so each alloy sample would be subjected to the same processing parameters and conditions. The parameters were held constant for both alloy deposition processes. Figure 10 shows the jig used for holding the samples and Figure 11 illustrates the jig inside the vacuum chamber of the CAD equipment, which is shown in Figure 12.

TABLE V: PROCESSING PARAMETERS FOR SAMPLE COATING AS SUPPLIED BY THE NRC.

Stage	Cathode Current (A)	Working Pressure of Argon (mbar)	Substrate Bias (V)	Duration (hrs)
Cleaning	80	2.0×10^{-4}	-280	.5
Deposition	90	2.0×10^{-2}	-100	4

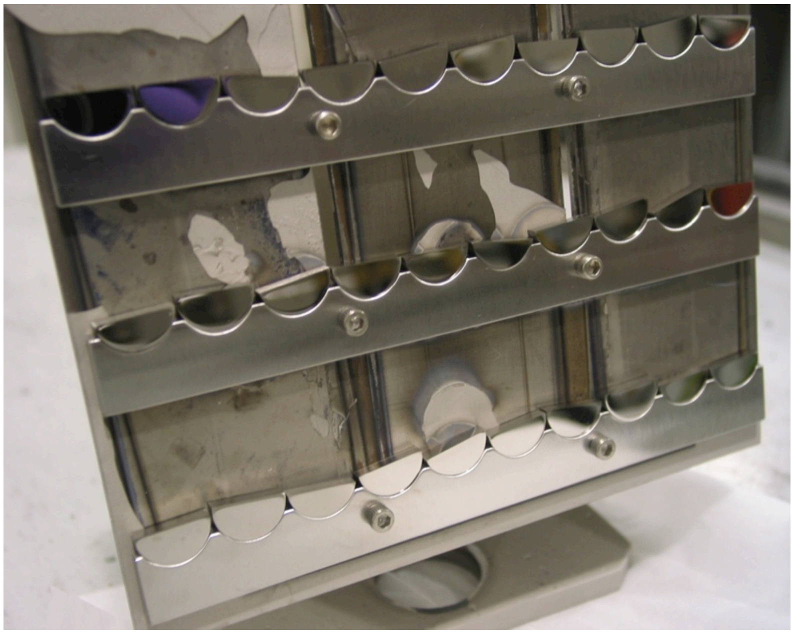

Figure 10: Sample jig used to hold 30 samples at a time for the deposition process.

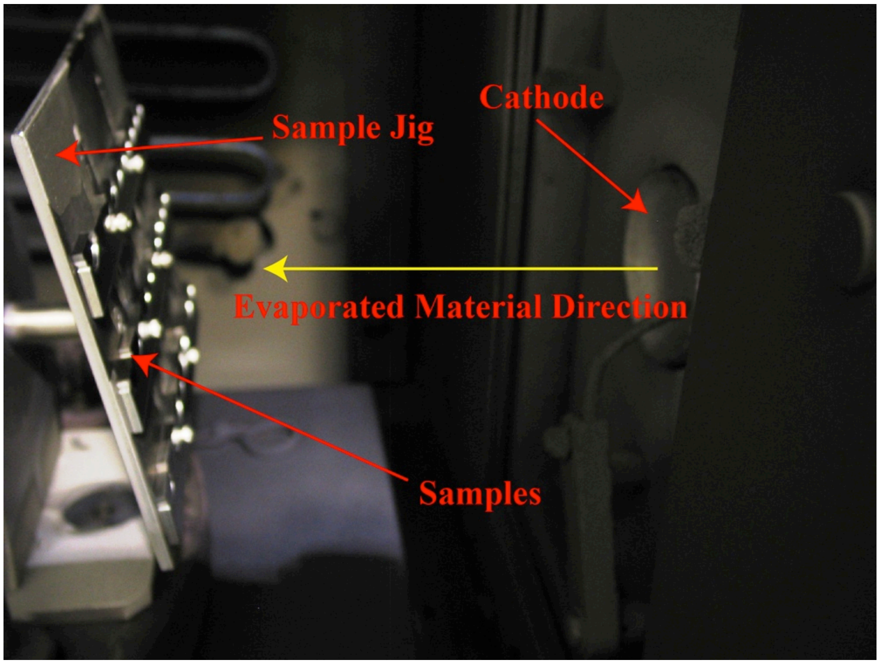

Figure 11: Jig inside the vacuum chamber of the CAD equipment.

Figure 12: Sulzer Metaplas MZR304 CAD equipment used for deposition of the Ni-5Cr -15Al overlay coating.

Once the samples were coated, they were sent back to the University of Manitoba for heat treatment. The heat treatment involved heating the coated samples to 1140 ℃ for 6 hrs under vacuum (approximately 15 μbar) followed by furnace cooling. After the samples had cooled to room temperature, they were lightly polished using 0.5 micron silica solution to remove any surface roughness that remained due to the deposition or heat treatment processes in order to eliminate the effect surface roughness has on the oxidation process.

3.2 Isothermal Oxidation Testing

This section describes the set-up that was used for isothermal oxidation testing of both substrate materials for the un-coated and coated experiments. Discussion of the equipment and materials used as wells as problems encountered with applicable solutions are presented.

3.2.1 Isothermal Oxidation

For isothermal oxidation 10 samples of each alloy were prepared following the same procedure as outline in Section 3.1. Before oxidation, the samples and the crucibles were weighed using a digital scale sensitive to $\pm$0.0001g. After the weights of both the samples and the crucibles were acquired, the samples were placed in the crucibles. The placement of the samples in the crucible, shown in Figure 13, was such that the face to be oxidized was perfectly flat in the bottom of the crucible and exposed to the oxidizing environment. The crucibles were organized in a fixed sequence on an alumina plate, which is shown in Figure 14. The samples were kept in this arrangement throughout the duration of the experiment to allow for easy identification of each sample once removed from the box furnace. The Blue M furnace used for oxidation testing is shown in Figure 15.

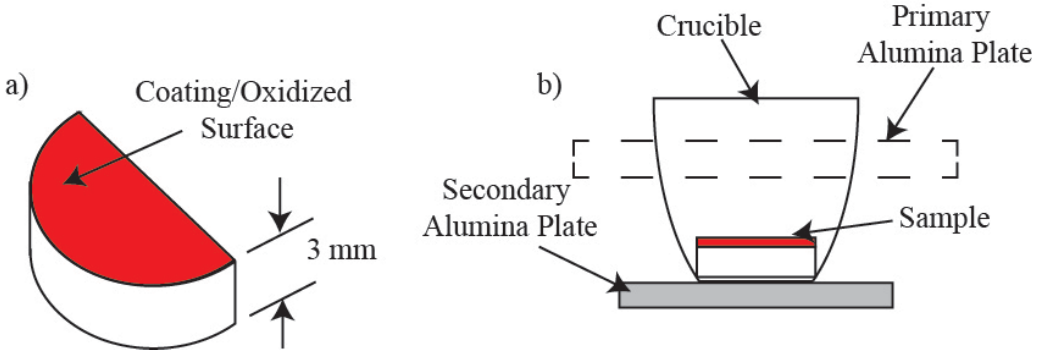

Figure 13: a) Sample showing primary coating/oxidation surface. b) Sample placement inside crucible, showing interaction between primary, secondary plates and crucible.

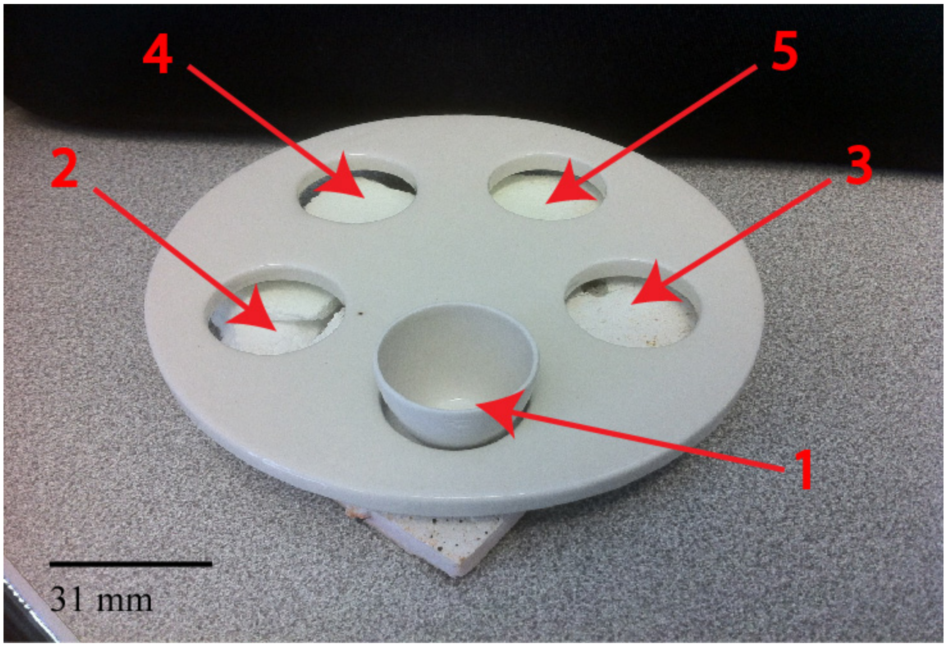

Figure 14: Sample arrangement on the primary plate indicated by numbers 1 - 5.

Figure 15: Blue M box furnace used for oxidation of samples at 1100 ℃.

In addition to keeping the crucibles in a fixed sequence during placement in the box furnace, the primary alumina plate also held the crucibles in an upright position during the isothermal oxidation, keeping the crucibles from falling over when handling other specimens in the furnace. Due to the difference in thermal expansion between the crucibles and the alumina plates, a secondary plate was needed under the crucibles to create a small gap between the plate and crucible during oxidation. This small gap allowed each item to expand at different rates reducing the risk of the crucible breaking or becoming wedged in the plate during testing. The primary and secondary plates in the arrangement used during oxidation can be seen in Figure 16.

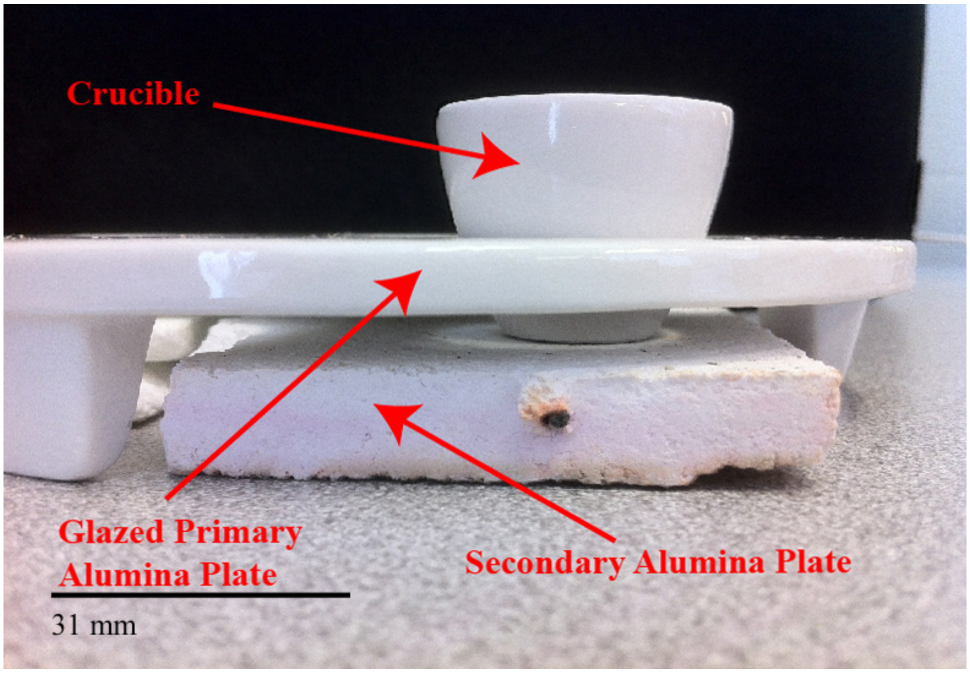

Figure 16: (top) Primary glazed alumina plate. (bottom) Secondary unglazed alumina plate.

Both the secondary and primary plates with the 5 samples in each arrangement were placed in the furnace set initially at 550 °C. The temperature was ramped to 1100 °C over 2 hours to ensure the crucibles and plates did not crack during the heating process. The plates remained in the furnace during the entire time of the experiment. The samples and crucibles were oxidized at 1100 °C and removed at 5 hr, 10 hr and 24 hrs at which point the remaining samples were removed after a 24 hr period up to a maximum exposure time of 192 hrs. After removal of the samples and crucibles their oxidized weights were established and mass gain calculated. Any spalled material left in the crucibles were collected and sealed inside test tubes to be used in the powder x-ray diffraction (XRD) equipment for XRD analysis. The samples were cut in half and the cross-sections mounted in Bakelite resin for SEM analysis.

3.3 Microscopy and Instrumental Techniques

Three different instrumental techniques were used as the primary means of analyzing the samples before and after oxidation, SEM, EDS and XRD analyses. Instrumental setup and the analysis techniques used for post-oxidation analyses of the un-coated and coated samples are discussed in the following section.

3.3.1 Scanning Electron Microscopy and Energy Dispersive Spectroscopy

First, the scanning electron microscope (SEM) was used in conjunction with an energy dispersive spectroscopy (EDS) detector to identify areas of interest within the samples. For this project the SEM used was JEOL JSM-5900L V scanning electron microscope with a precentered tungsten hairpin filament with a resolution up to 100 nm.

Interestingly, some problems with electron charging were encountered due to the relative proximity of the area of interest to the edge of the sample. Interference from the Bakelite, through Bakelite charging, made it difficult to distinguish features for analysis. Therefore, a thin carbon coat layer, 20 - 25 nm was applied to reduce the charging effects caused by the Bakelite and this produced clearer images, which enabled identification of areas of interest.

High-resolution images of the oxide growth after oxidation were used in order to identify regions of interest such as, external/internal oxidation regions, cracking of the oxide/coating or other microstructurally significant regions. These regions were then compositionally analyzed using the EDS technique. EDS spectra were acquired using the same JEOL SEM equipped with an Oxford 50 mm^2 X-Max EDS detector. Figure 17 illustrates the arrangement.

Figure 17: SEM equipment used for analysis of samples.

3.3.2 X-ray Diffraction (XRD) Analysis on the Un-Coated Samples

For this work, the powder X-ray diffraction equipment in the Geology and Mineralogy Lab in the Department of Geology at the University of Manitoba was used. The powder collected in the crucibles due to oxide spallation during oxidation was crushed to a uniform texture using an alumina mortar and passel. A few drops of acetone supplied lubrication during the crushing process. After the powder was crushed to a uniform consistency, it was placed on a zero background quartz plate and secured in the Siemens D5000 X-ray powder diffractometer. A copper target was used as the X-ray source. Figure 18 illustrates the setup used.

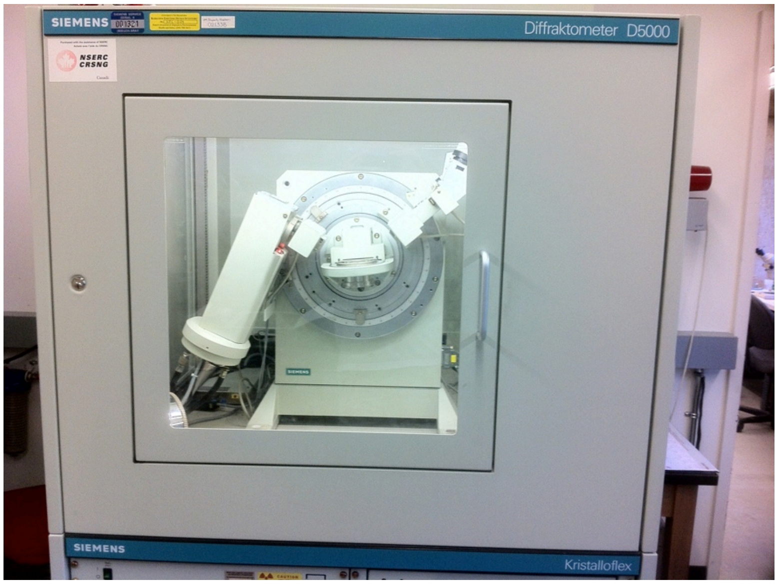

Figure 18: Powder XRD equipment used.

X-rays were collected from 4° to 80° of 2θ angle using an increment of .05°/step and a scan duration of 3sec/step. Diffraction patterns were collected using Diffracplus XRD Commander software and peak identification was performed using MID JADE 7 software.

3.3.3 X-ray Diffraction (XRD) Analysis on the Coated Samples

For this work, the single crystal X-ray diffraction equipment in the Geology and Mineralogy Lab in the Department of Geology at the University of Manitoba was used. XRD analysis on the coated samples was done using Bruker D8 discover SuperSpeed Micro-Powder Diffractometer, shown in Figure 19 and GADDS software for data acquisition. X-ray alignment was done using a laser-video alignment assembly with a specially adapted Gandolfi camera attachment for presentation of extremely small volume samples. A .3/.1 mm monocap collimator was used to reduce the size of the incident X-ray beam in order to reduce background noise and focus on the sample mount. A Hi-Star multiwire proportional 2D detector was used to gather the diffraction patterns.

Samples were analyzed using 2 frames at 35° and 60° with a frame width of ± 17° using a generator setting of 50KV/60 mA and a constant 15 cm detector distance from the samples. This yielded diffraction patterns for a 2θ between 20° and 80°.

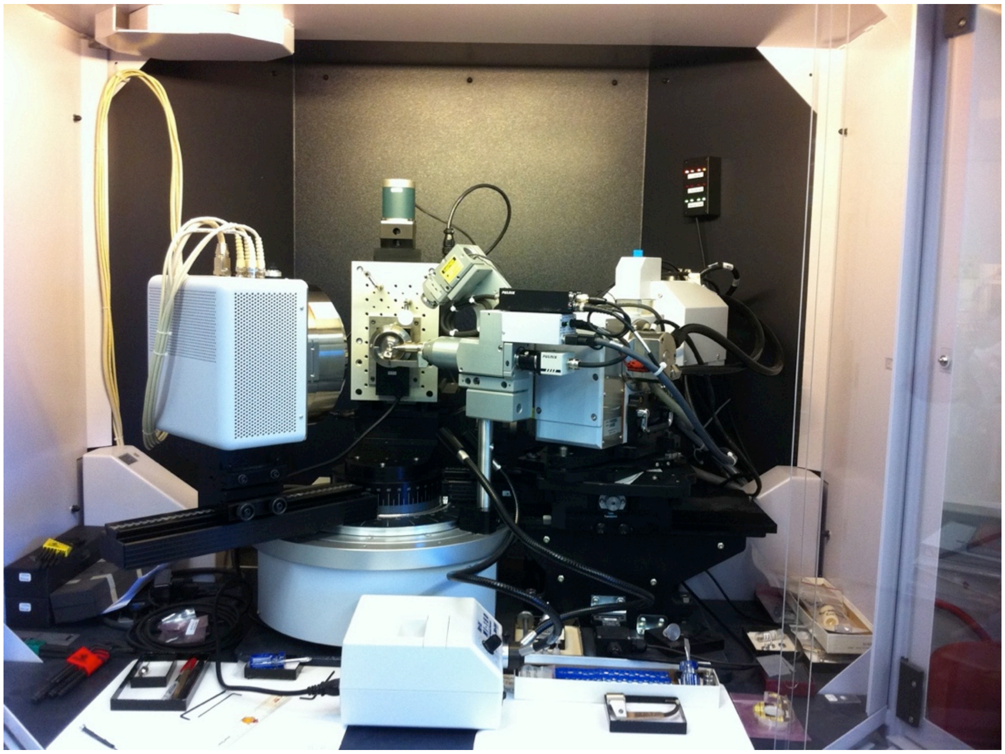

Figure 19: XRD single crystal equipment used for analysis of oxides from the coated material CMSX-4 and CMSX-486.

Samples of the oxide were carefully scraped from the surface and mounted in a 20 μm microloop and held in place by epoxy. The microloop was then mounted in the XRD equipment and the 100 μm beam aligned and centered on the microloop. While the equipment was in operation, the microloop rotated 360° while keeping the sample centered in the x-ray beam for best diffraction results.

4.0 Part A: As-Cast, As-Coated and Heat Treated Materials

As outlined in Section 3.1.2, the substrate materials to be coated consisted of as-cast CMSX-4 and CMSX-486, which were subsequently heat-treated, coated then heat treated again. Part A of the thesis will present and discuss experimental results on the as-cast, as-coated and heat-treated materials. Microstructural observations are presented from SEM analysis, in addition to compositional observations performed by EDS and XRD analyses.

4.1 Results of Heat Treatment on As-Cast Material

By comparing Figure 7 with Figure 20 some minor changes in γ' and eutectic regions were observed. Primarily, the most significant change is the occurrence of smaller γ' particles and the reduction in the size of the eutectic regions as a result of re-solutioning of the eutectic regions and re-precipitation of γ' particles during heat treatment at 1305 °C for 6 hrs. followed by furnace cooling.

Some minor carbides can also be noticed as bright features in Figure 20, which have similar composition to the carbides observed in the as-cast condition.

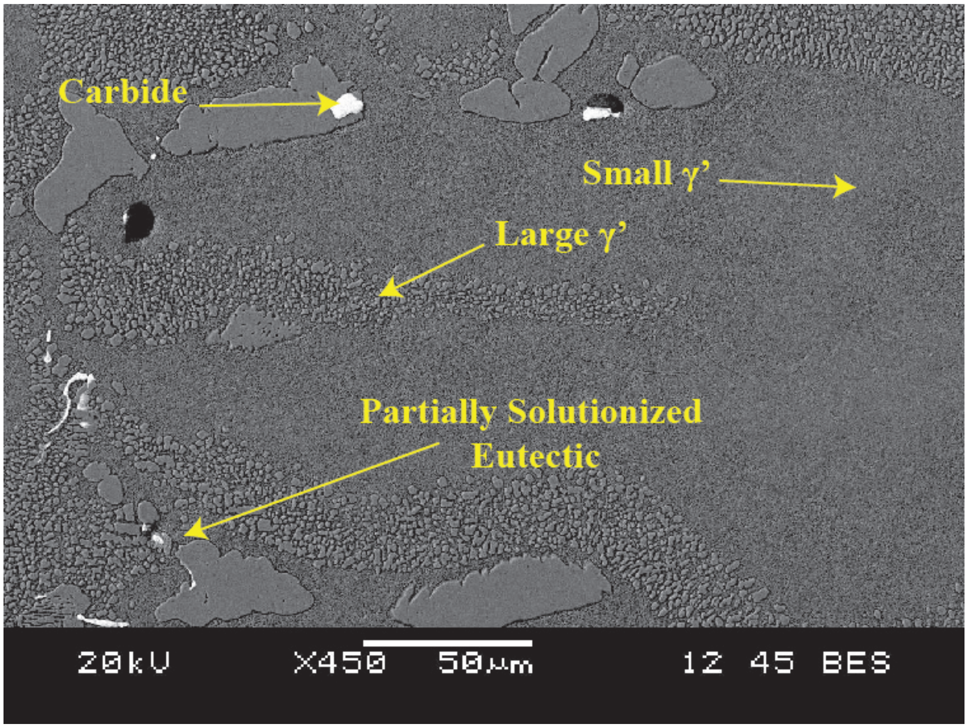

Figure 20: Backscatter image of heat-treated CMSX-4. White particles indicate heavier elements such as those found in carbides.

By comparing Figure 8 with Figure 21 some minor changes in γ' and eutectic regions were observed. Primarily, the most significant change is the occurrence of smaller γ' and coarsening of larger γ' particles, as well as the reduction in the size of the eutectic regions as a result of re-solutioning of the eutectic and re-precipitation of γ' particles during heat treatment at 1238 °C for 1 hr, 1243°C for 1 hr and 1249 °C for 1 hr followed by air cooling.

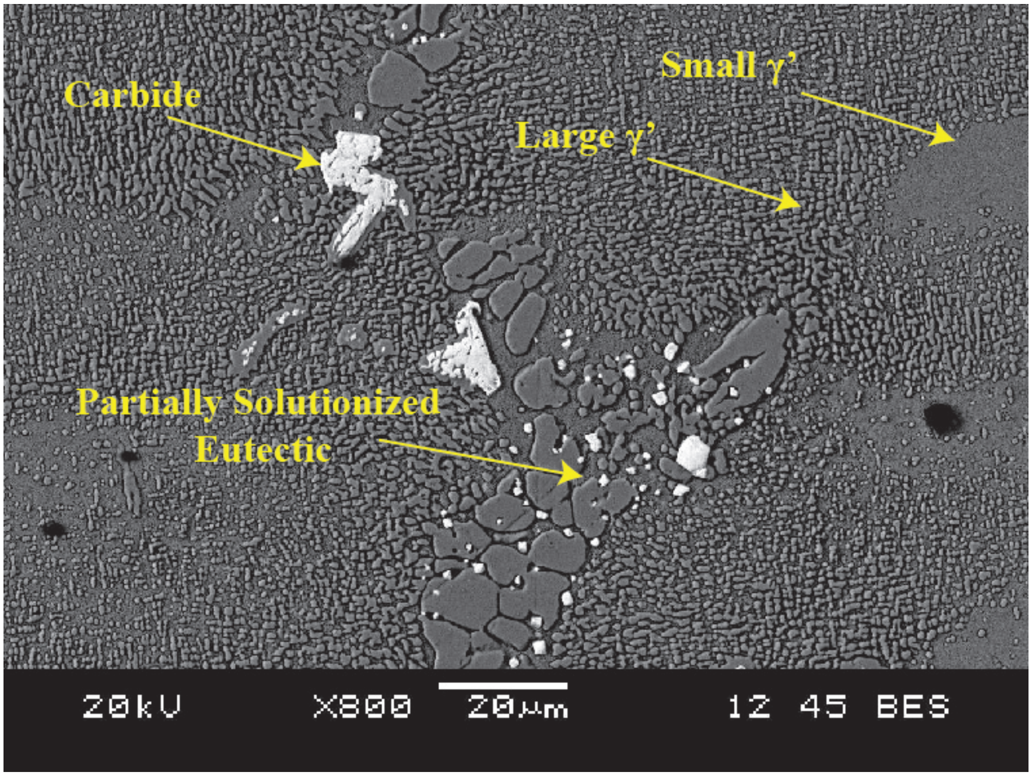

Figure 21: Backscatter image of heat-treated CMSX-486. White particles indicate heavier elements such as those found in carbides.

In addition, Hf-rich intermetallic particles and carbides were also observed in the heat-treated material with similar compositions to those found in the as-cast alloy.

4.2 Results of Coated and Heat Treated Materials

As outlined in Section 3.1.2, the coated materials were heat treated in vacuum at 1140 °C for 6 hrs followed by furnace cooling. After heat treatment, one sample of each alloy was randomly chosen, and a cross-section prepared for viewing in the SEM. Figure 22 and Figure 23 show the cross-sections of as-coated CMSX-4 and CMSX-486, respectively.

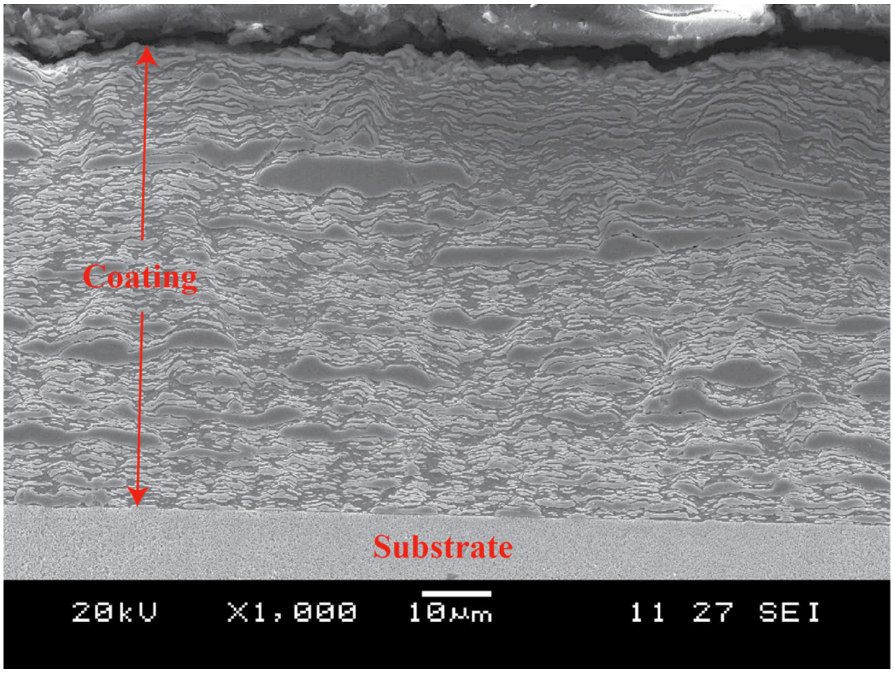

Figure 22: Cross-section view of as-deposited Ni-5Cr-15Al coating on CMSX-4 substrate.

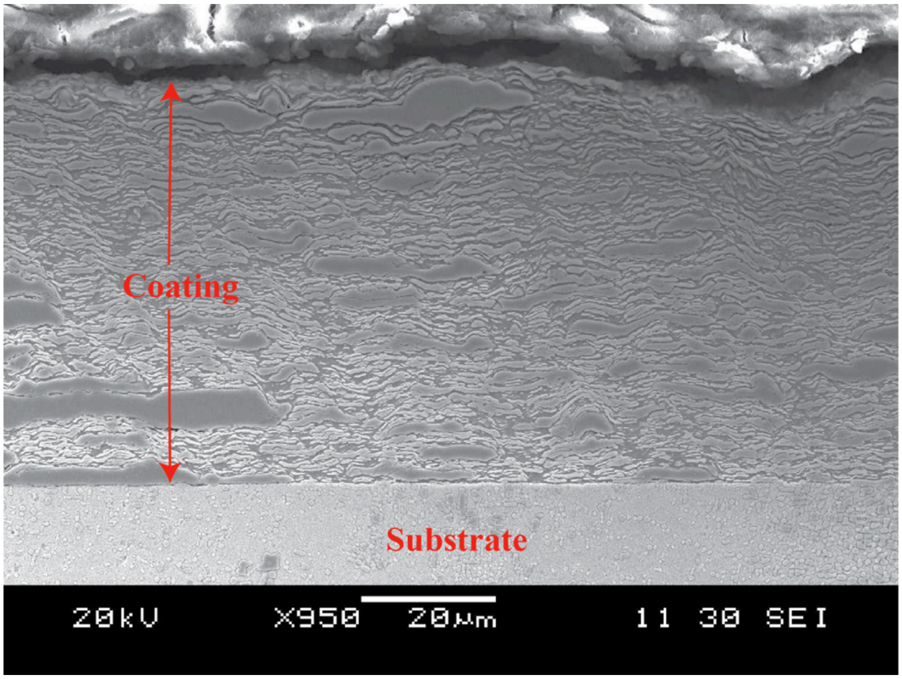

Figure 23: Cross-section view of as-deposited Ni-5Cr-15Al coating on CMSX-486 substrate.

Compositional analysis shows the coatings on both substrates were comparable to each other, with an approximate composition of 9.5 wt% Al, 6.5 wt% Cr and the remainder Ni. The localized darker globs show higher amounts of Al, while the regions between dark globs show higher Cr contents.

After coating deposition, the coated samples underwent heat treatment as described in Section 3.1.2. Again, after heat treatment a random sample was chosen from each alloy and analyzed with the SEM. Figure 24 and Figure 25 show cross-sections of the heat-treated coating on CMSX-4 and CMSX-486, respectively. Zone 1 signifies the substrate material, while zones 2 – 4 are within the deposited coating material.

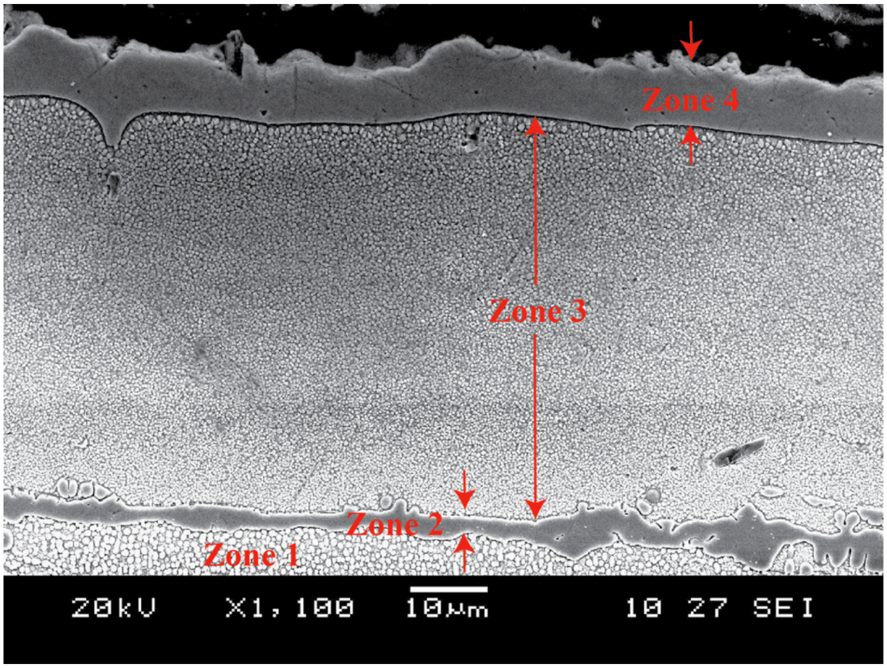

Figure 24: Secondary electron cross-sectional image of heat-treated coating on CMSX-4 substrate.

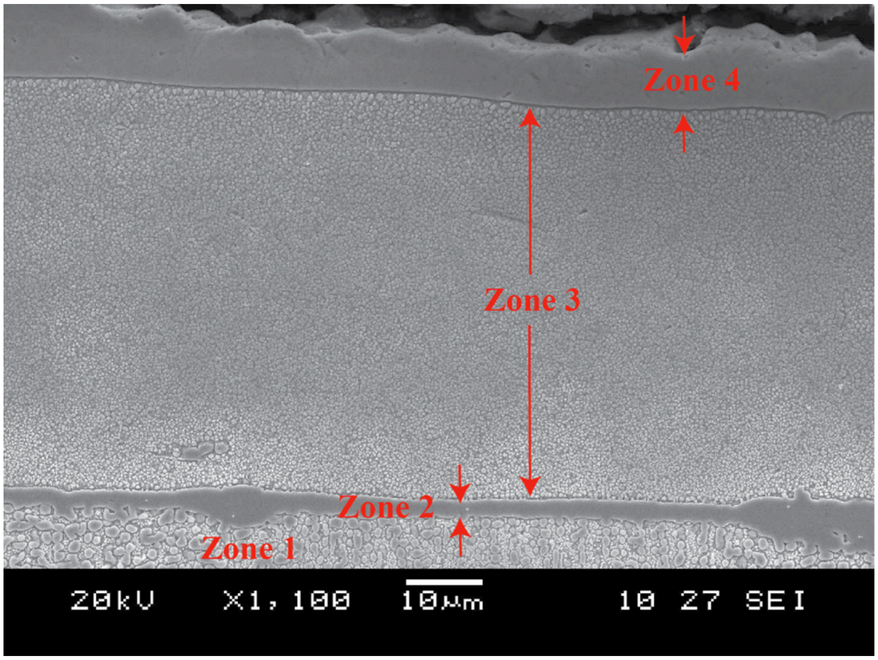

Figure 25: Secondary electron cross-sectional image of heat-treated coating on CMSX-486 substrate.

Analyzing and comparing the cross-sections of the heat-treated coating material revealed four distinct zones on both alloys. EDS compositional analysis on each of these zone was performed, (Table VI) and the results checked against a phase diagram section for Ni-Al-Cr at 1100 °C, as shown in Figure 26, to obtain possible phases present for each zone.

TABLE VI: APPROXIMATE COMPOSITION OF EACH ZONE FOR COATED AND HEAT-TREATED MATERIALS

	CMSX-4 (at%)				CMSX-486 (at%)			
	Zone 1	Zone 2	Zone 3	Zone 4	Zone 1	Zone 2	Zone 3	Zone 4
Ni	71.32	72.56	74.88	73.14	71.66	71.1	71.65	72.56
Al	9.51	17.52	19.56	25.21	12.00	19.9	22.05	25.06
Cr	5.79	2.747	5.55	1.65	5.25	3.09	5.61	2.39
Co	7.77	2.55	-	-	5.37	2.46	0.69	-
Ta	1.82	2.44	-	-	1.18	1.02	-	-
Ti	1.13	0.75	-	-	0.63	0.69	-	-
W	1.81	1.23	-	-	2.73	1.75	-	-
Mo	0.29	-	-	-	0.26	-	-	-
Re	0.55	-	-	-	0.77	-	-	-
Hf	-	-	-	-	0.15	-	-	-

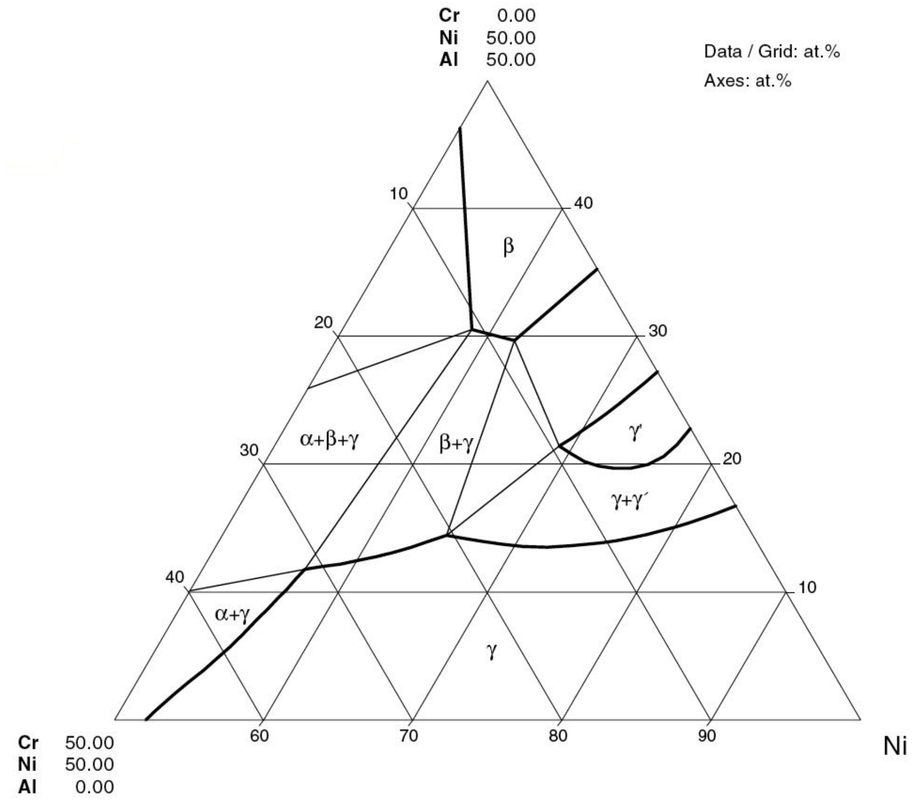

Figure 26: Ni-Al-Cr ternary phase diagram for 1100 ℃. Taken from [*58*]. Reprinted with the kind permission of Springer Science & Business Media.

These results suggest that zone 4 consists of γ' and zone 3 was of $\gamma + \gamma'$, while zone 2 consists of an intermetallic single phase caused by interdiffusion between the coating material and substrate. These results are supported by the micrographs taken from each section with the SEM. Zone 4 and zone 2, as seen in Figure 24 and Figure 25, is a single phase, while zone 3 appears to be made up of many small spherical shaped precipitates within a matrix material. These results, along with how isothermal testing affects each zone, are summarized in Figure 49 and Figure 50 in Section 6.1.2.

4.3 Discussion of Heat Treatment on As-Cast and As-Coated Material

The primary changes observed with heat treatment of the as-cast materials include changes in γ' morphology, the occurrence of secondary γ' and re-solutionizing of the eutectic regions, all of which affect the strength and creep resistance of the materials at high temperatures. These also affect the distribution of elements by the re-solution of carbides in CMSX-4 and the re-solutioning of Hf-rich intermetallic particles and eutectic regions in CMSX-486. As mentioned in the discussion of the un-coated materials, element distribution is important during selective oxidation because there must be sufficient element reserves for Al (and Hf in CMSX-486) in order for a protective and adherent alumina scale to form. Otherwise, element diffusion from within the substrate material and internal oxidation will occur leading to decreased strength and creep resistance.

The heat treatment performed on the as-coated material for both alloys had a more significant effect, as seen in the micrographs presented in Figure 22 to Figure 25. The as-coated globular structure transformed into a multi-layered, multiple phase structure upon heat treatment. A thin interdiffusion zone was created (zone 2) due to diffusion between the substrate and coating, where some Ni and Al diffused from the coating into the substrate and other elements, such as Co, Ta and W diffused from the substrate into the coating. The role of these regions and their connection with oxidation performance are discussed further in subsequent sections.

5.0 Part B: Oxidation Experiments on Un-Coated Materials

This section contains the results of isothermal exposure of the un-coated alloys at 1100 °C following the experimental set-up as described in Section 3.0. The results of CMSX-4 are discussed in Section 5.1.1, which include microstructural and compositional changes during exposure as well as an account of which oxides were present at various stages of oxidation. Similar results for CMSX-486 are given in Section 5.1.2. A discussion of the oxidation characteristics of the two alloys as well as information regarding oxidation performance of CMSX-4 and other alloys similar to CMSX-486 are presented in literature is given in Section 5.2.

5.1 Oxidation Performance of Un-Coated Materials

The mass change plots from oxidation on un-coated alloys are shown together in Figure 27. The entire surface area was used for the calculation of the mass change per area. For CMSX-4 this was approximately 2.654 cm^2 and 2.38 cm^2 for CMSX-486.

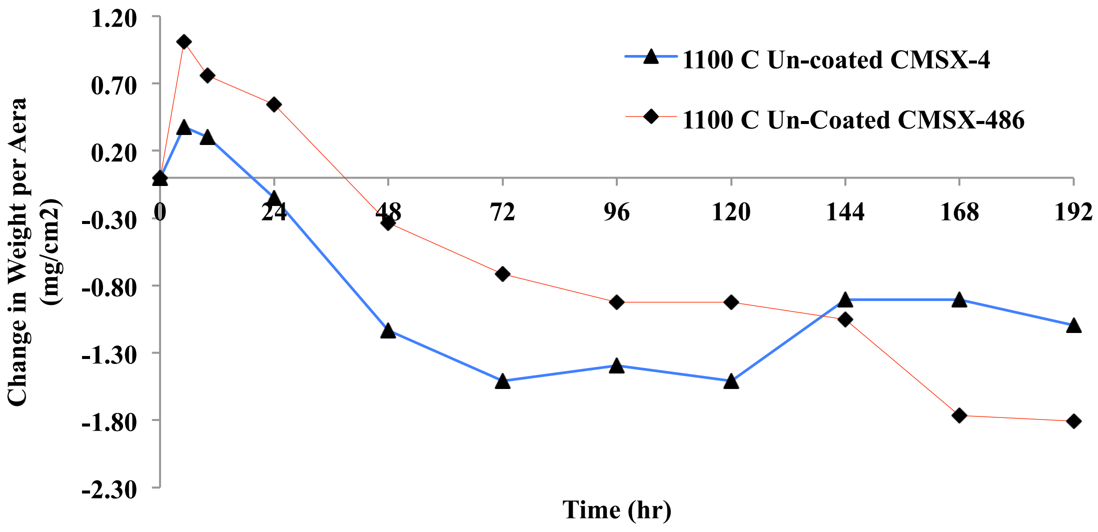

Figure 27: Mass gain plots for un-coated CMSX-4 and CMSX-486 after isothermal oxidation at 1100 ℃.

However, it should be noted that the majority of the oxidation occurred on the top surface exposed to the oxidizing environment as shown in Figure 13 and therefore contributed the most to the mass gain of each sample.

5.1.1 CMSX-4 Microstructure and Composition

This section covers microstructural and compositional changes observed during the oxidation of un-coated CMSX-4. The first section outlines the observed microstructures and oxides present obtained from SEM micrographs. The following section discusses the observed oxidation behavior based on the mass gain, microstructure and chemical composition from SEM, EDS and XRD analyses.

5.1.1.1 Oxide Microstructural Changes with Exposure

As illustrated by the mass gain plots given in Figure 27, a closer inspection of the oxidized samples showed there were very small areas on the oxidized surface that still had oxides attached. The amount of the oxides was sufficient for microstructural and chemical analyses, to understand the progression of oxidation.

5 hr – 10 hr Exposure:

The initial oxide that formed was thin, only 2 – 5 μm. Under this thin layer of oxide, a γ' precipitate free zone (PFZ) developed as well, which was between 2 – 7 μm thick. Finally, under the PFZ, the γ', as well as eutectic $\gamma - \gamma'$ became coarser. A typical microstructure for the 5 hr – 10 hr exposure samples is given in Figure 28, where the thin oxide layer, PFZ and coarsening γ' as well as $\gamma - \gamma'$ eutectic can be seen.

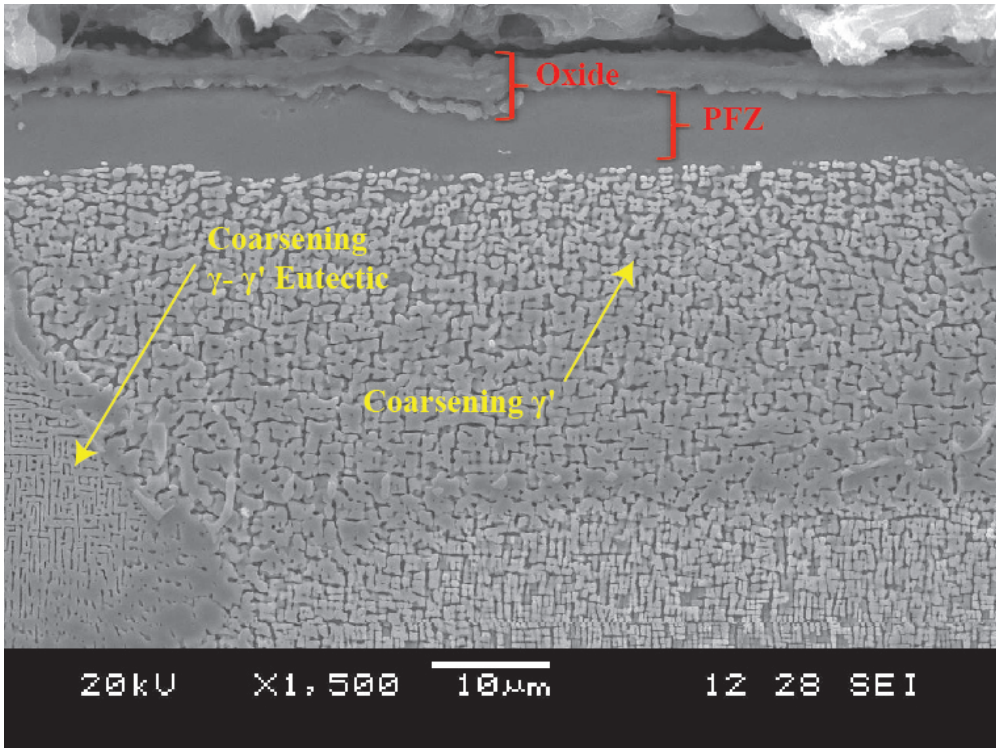

Figure 28: 10 hr exposure at 1100 C of CMSX-4 un-coated.

In some localized areas on the 5 hr and 10 hr samples, there were regions with extreme oxidation. These regions showed both external and internal oxidation scales, which are referred to in this work as super-oxidized regions. These regions consisted of multiple oxide layers built up on parallel planes to the substrate surface. Each layer was distinct and organized along its length. Only a few of these regions were observed on each of the 5 hr and 10 hr samples, with an average height and length of 25 μm and 100 μm respectively. Some small pores and voids were observed along various layers within the oxide and along the surface. Figure 29 illustrates this morphology.

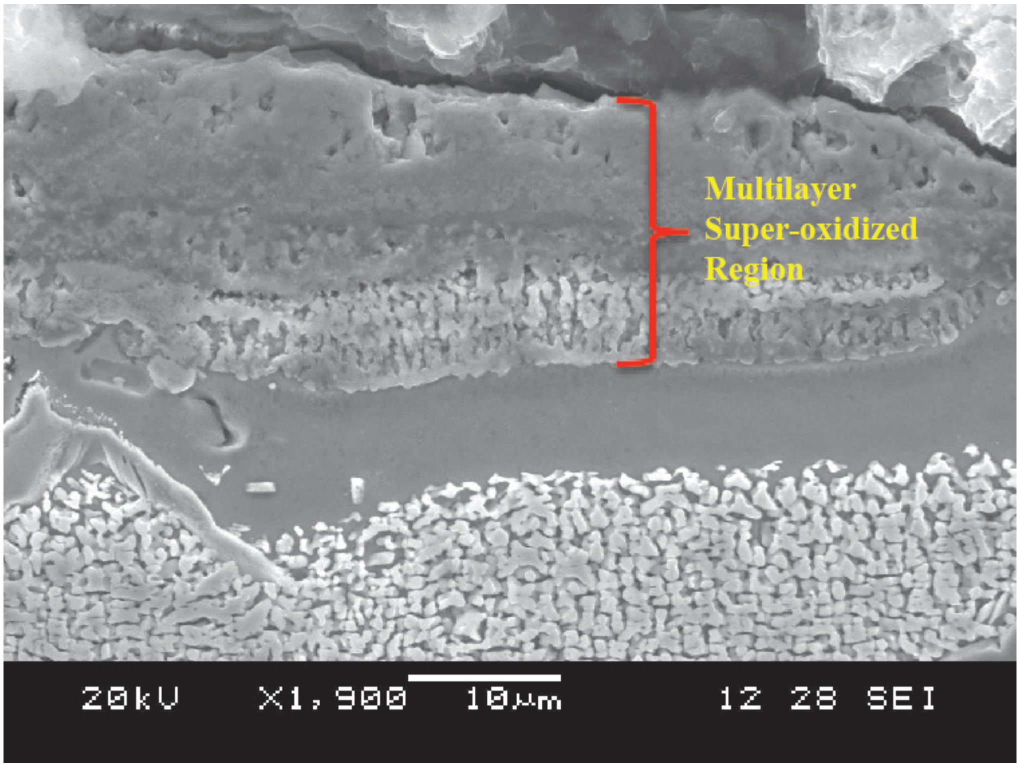

Figure 29: Super-oxidized region of 5 hr oxidized un-coated CMSX-4 sample at 1100 ℃. Multilayer super-oxidized region running parallel to the sample surface above the PFZ.

24 hr – 192 hr Exposure:

After 24 hrs of exposure, typically only super-oxidized regions remained. The super-oxidized regions had significantly increased in size (approximately 50 μm in height and 150 μm in length). In addition, upon a closer inspection of the 24 hr sample with the SEM, small particles were noticed within the PFZ below and separate from the oxide layer. These particles were observed to increase in size and number with longer exposure times and in some cases, completely filling the PFZ. These particles within the PFZ, as well as the larger super-oxidized regions are shown in Figure 30.

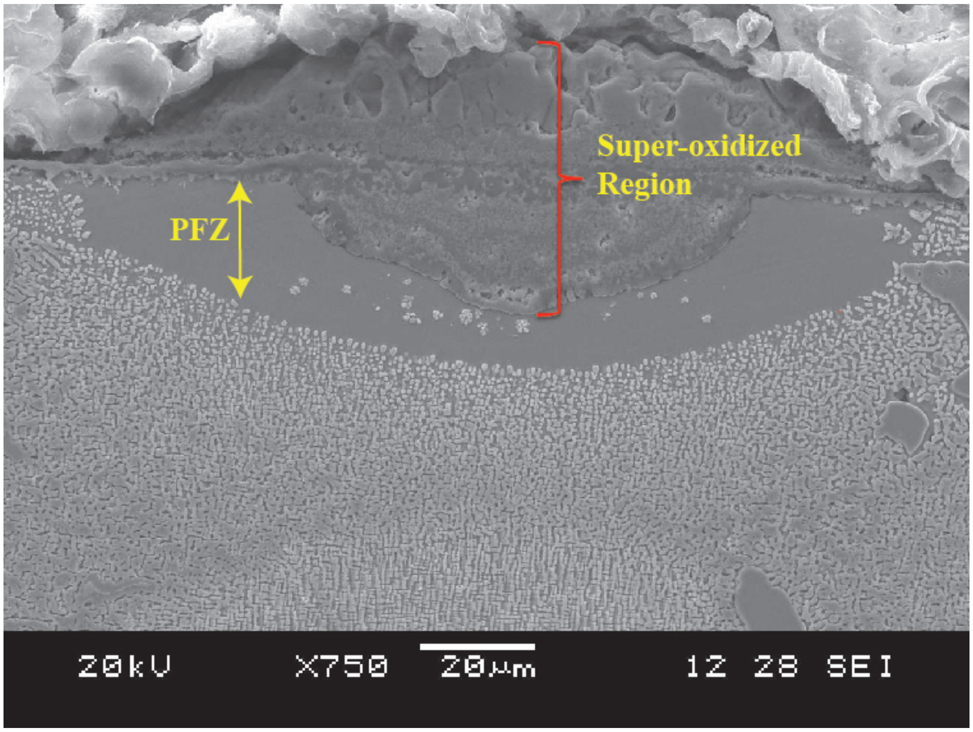

Figure 30: Super-oxidized region on 24 hr exposure CMSX-4 un-coated sample oxidized at 1100 °C.

Unlike the super-oxidized regions observed on the 5 – 10 hr samples, these super-oxidized regions sometimes had cracks running through several layers, or had most/all of the external oxide removed. This phenomenon is shown in Figure 31 and Figure 32.

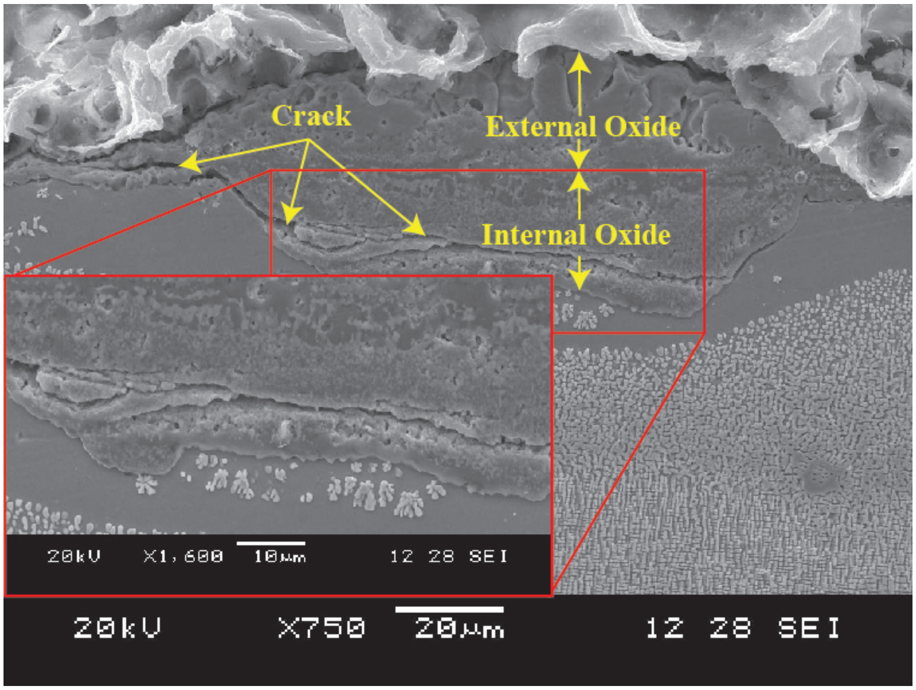

Figure 31: Cracking observed within super-oxidized region of the 24 hr exposure CMSX-4 oxidized sample.

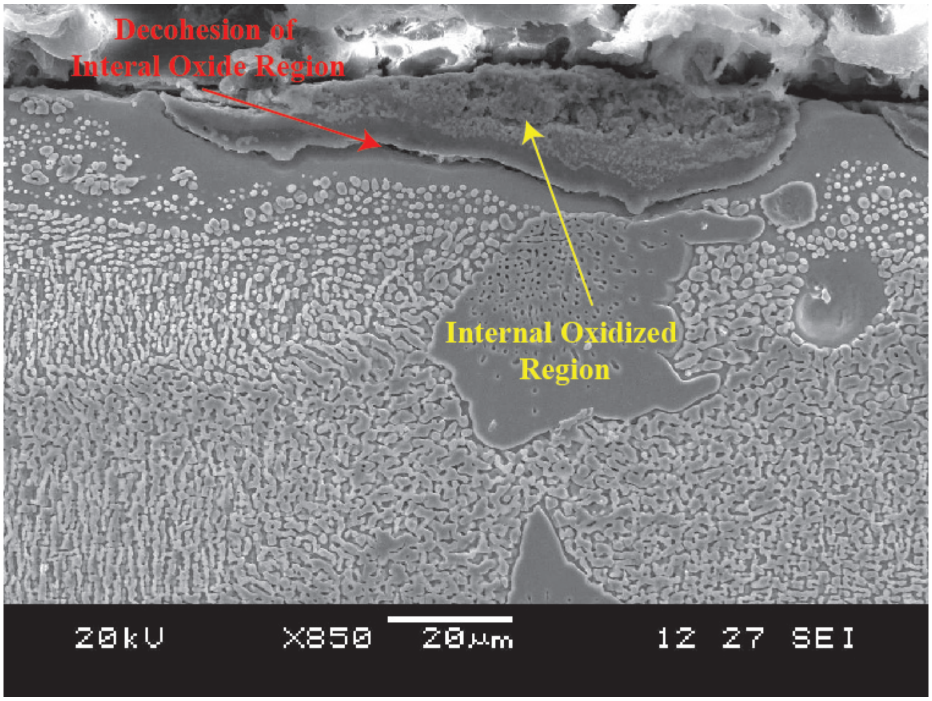

Figure 32: 144 hr exposure CMSX-4 sample showing only internal oxidized region.

Upon longer exposures, there was a noticeable decrease in the amount of thin oxide that still remained attached to the substrate for analysis. Exposed PFZ with no oxide was a common occurrence. As oxidation exposure time increased beyond 24 hrs, the thin oxide scale still attached to the substrate material were typically covering areas with significant oxidation particles present within the PFZ. These thin oxide scale, unlike the thin oxide scale observed in the initial 5 hr – 10 hr samples, only consisted of a single layer of oxide material typically only 1 – 2 μm thick.

5.1.1.2 Oxide Composition Change During Exposure

Compositional analysis was carried out using EDS and XRD analyses as described in Section 3.0. EDS analysis was done on the oxide scales attached to the substrate material, while XRD analysis was performed on the spalled oxide collected in the crucible after oxidation.

5 hr – 10 hr Exposure:

Line scans of the thin oxide layer showed that it was composed of multiple layers. Oxides found on these samples consisted of a Ni rich outer oxide layer, followed by a Ti/Cr rich oxide over a continuous Al rich internal oxide. However, some regions consisted of only Al rich oxide layer. Figure 33 shows a line scan of the thin oxide consisting of multi oxide layers found on the 5 hr – 10 hr samples.

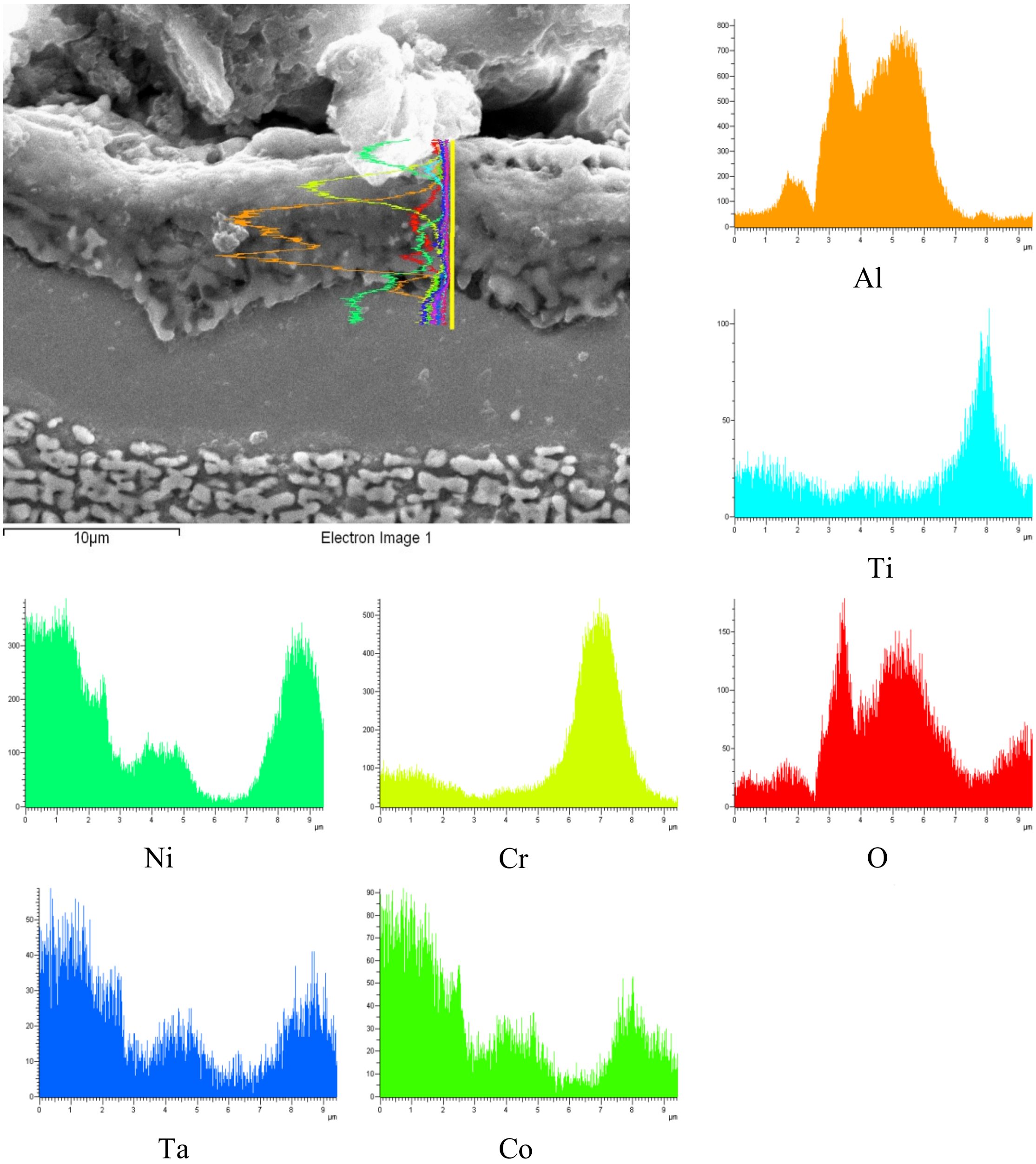

Al

Ti

Ni

Cr

O

Ta

Co

Figure 33: Line scan of the 10 hr un-coated CMSX-4 sample.

Area maps and line scans of the super-oxidized regions observed on the 5 hr – 10 hr samples reveal multiple oxide layers with only slight variation of element presence but large variation in concentration. The PFZ in both 5 hr and 10 hr samples were found to be depleted in Al and Ti.

24 hr – 192 hr Exposure:

Line scans of the single thin oxide layer reveals that it is primarily rich in Al, with trace amounts of Cr, Co, Ti and Ta inside the oxide. These thin, single layer oxides seemed to be infrequently observed on the surface of the material; therefore performing multiple compositional scans of various areas for a larger sample size was difficult.

Area maps and line scans of the larger super-oxidized regions still attached to the substrate for exposures longer than 24 hrs reveal similar compositional distributions to the super-oxidized regions observed on the 5 hr – 10 hr samples.

As previously discussed, cracking was observed through the interface between the Al and Ti rich oxide layers. This resulted in spallation of the external oxidized region leaving only the internal oxide as shown in Figure 32.

The oxide particles, which developed in the PFZ, were identified to be rich in Cr, Al and Co with varying amounts of Ta, Ti, W and Ni, depending on the particle. The presence of these elements within the particles remained constant throughout oxidation.

XRD Results:

XRD analysis was performed following the procedure outlined in Section 3.0. Three samples were initially analyzed to identify any differences in the observed diffraction patterns. If any differences were observed, additional samples would be analyzed between the two dissimilar diffraction patterns in order to determine which exposure period resulted in a compositional change.

The three sample exposure times that were chosen to be analyzed included 48 hrs, 120 hrs and 192 hrs samples. The 5 and 10 hr samples did not have a sufficient amount of spalled material to give detectable diffraction patterns. Figure 34 shows the resulting XRD diffraction patterns for the initial three samples.

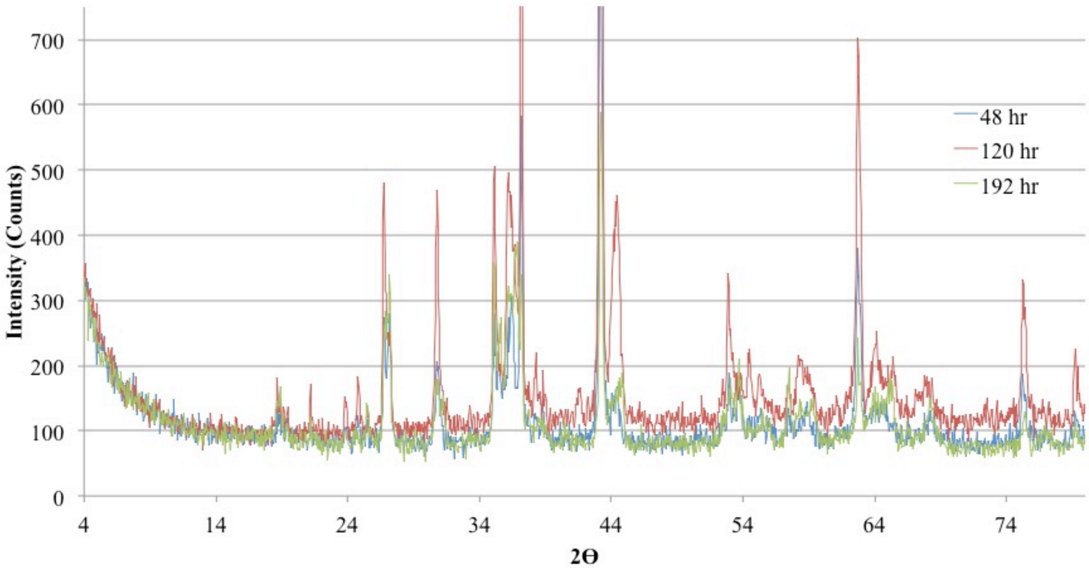

Figure 34: XRD diffraction patterns for un-coated CMSX-4 samples.

From Figure 34, it can be observed that there is no difference between each sample's diffraction patterns, other than increased intensity of the pattern. From the XRD patterns, and the EDS data that was gathered on each specimen, possible oxide compounds for each oxide layer could be formulated. Figure 35 depicts the XRD diffraction pattern and peak matched compounds of the 48 hr sample and Figure 36 shows an illustration with the various oxide layers labeled with possible compound.

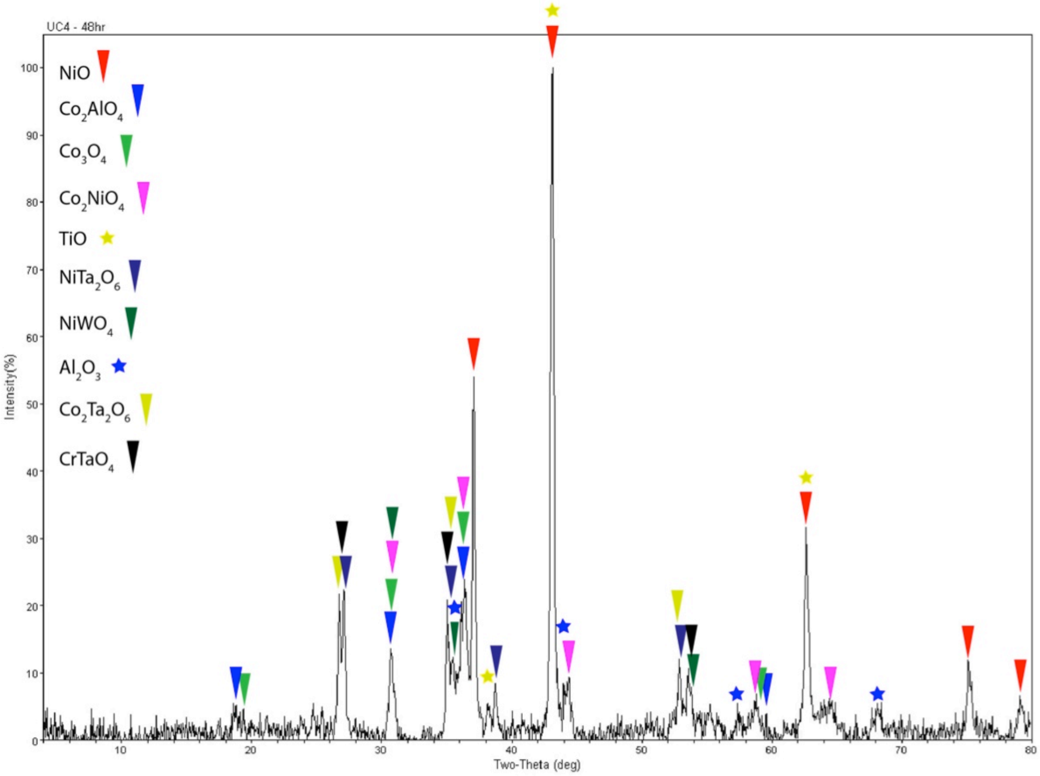

Figure 35: XRD pattern for un-coated CMSX-4 sample exposed for 48 hrs.

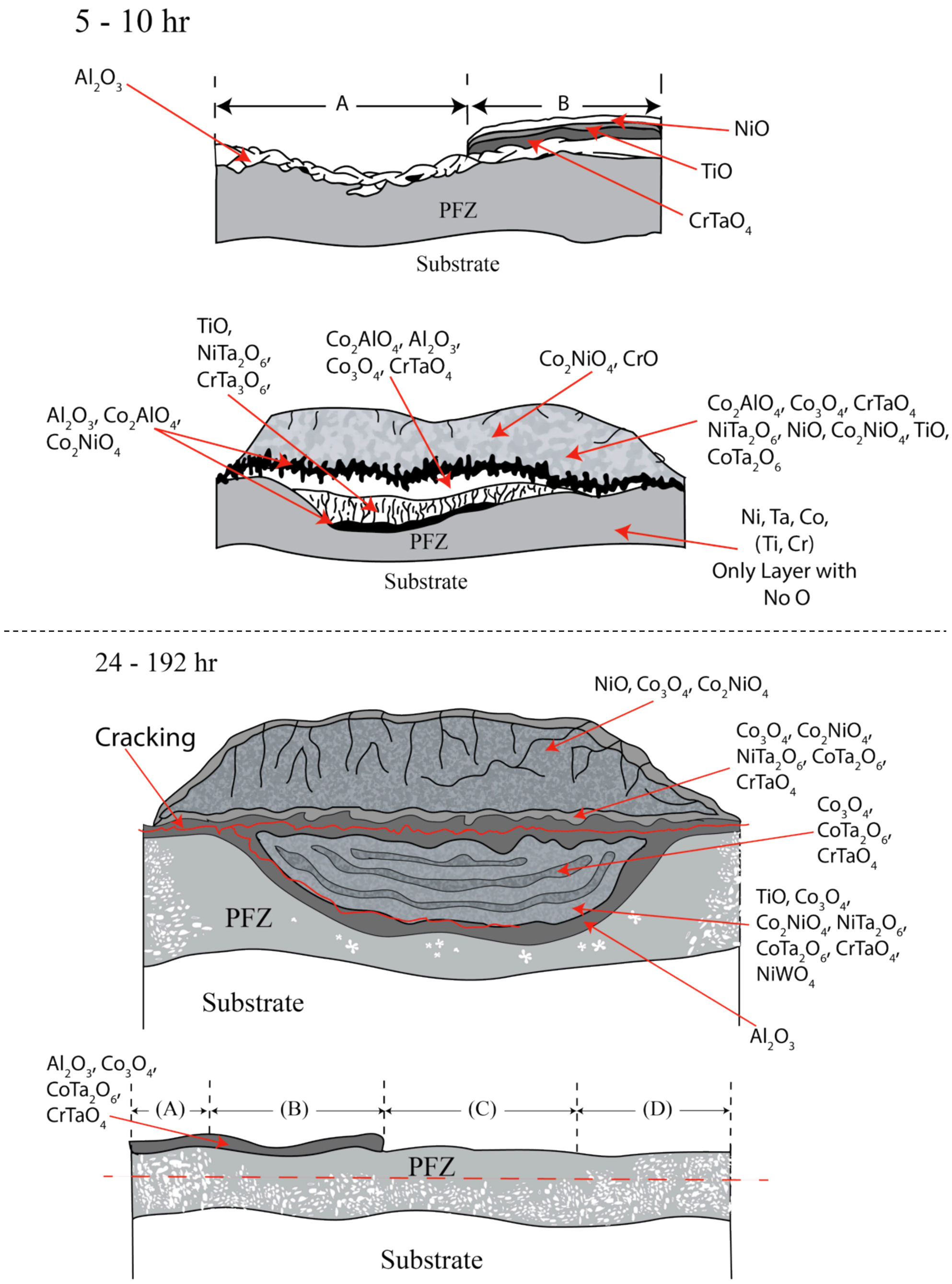

Figure 36: Summary of the possible compounds present in each oxide layers observed during high temperature exposure of CMSX-4.

Full diffraction patterns for each sample with peak matching can be found in Appendix A.

5.1.2 CMSX-486 Microstructure and Composition

This section covers microstructural and compositional changes observed during the oxidation test of un-coated CMSX-486. The first section outlines the observed microstructures and oxides obtained from SEM analysis. The following section provides observed oxidation behavior based on the mass gain, microstructure and chemical composition from SEM, EDS and XRD analyses.

5.1.2.1 Oxide Microstructural Changes with Exposure

As illustrated by the mass gain plots given in Figure 27, upon a closer inspection of the CMSX-486 samples, there is substantially more oxidized surface that still had oxide attached to it for microstructural and chemical analysis as compared to CMSX-4. There were three distinct groups of exposure periods that showed similar oxide morphology and composition. These groups are discussed in the following sections.

5 hr – 24 hr Exposure:

Oxides observed on the 5 hr – 24 hr samples were mostly disorganized multilayered oxide structures. Many of the oxide scales consisted of super-oxidized regions showing very large internal and external oxidized regions (ranging between 15 – 20 μm high and 40 – 60 μm in length). These super-oxidized regions often were connected to other super-oxidized regions or long sections of single layer external oxide scales. These super-oxides showed some evidence of spallation occurring within the external and/or internal oxidation regions.

Oxides which were adjacent to the PFZ, had finger like structures reaching 3 - 5 μm into the PFZ from the oxide scales above. Often white structures were observed within these finger structures, and within the PFZ separate from the oxide layers. The PFZ observed on the 5 hr exposure sample, was between 5 – 10 μm thick, which grew steadily as exposure time increased and again showed to be depleted in Al and Ti. Finally, under the PFZ, γ', as well as the $\gamma - \gamma'$ eutectic became coarser as observed with CMSX-4 oxidation.

48 hr – 72 hr Exposure:

Samples observed between 48 hrs – 72 hrs showed significant growth of the super-oxidized regions (height between 40 – 100 μm and lengths in excess of 150 μm). However, these regions also showed significant spallation within the external and internal oxide scales as illustrated by Figure 37. In addition, some super-oxide regions had only internal, or external oxide scales still visible, which are contrary to what was observed with the CMSX-4 samples (where only the external oxide scales were missing). The super-oxide regions were often connected to other super-oxide regions or to multilayer external oxide scales, unlike the single oxide scales observed in shorter exposure times.

The oxide fingers were measured to penetrate the PFZ between 5 – 10 μm, while the oxide and PFZ thickness steadily increased with exposure time. Particles within the PFZ also increased in size and frequency during the same period.

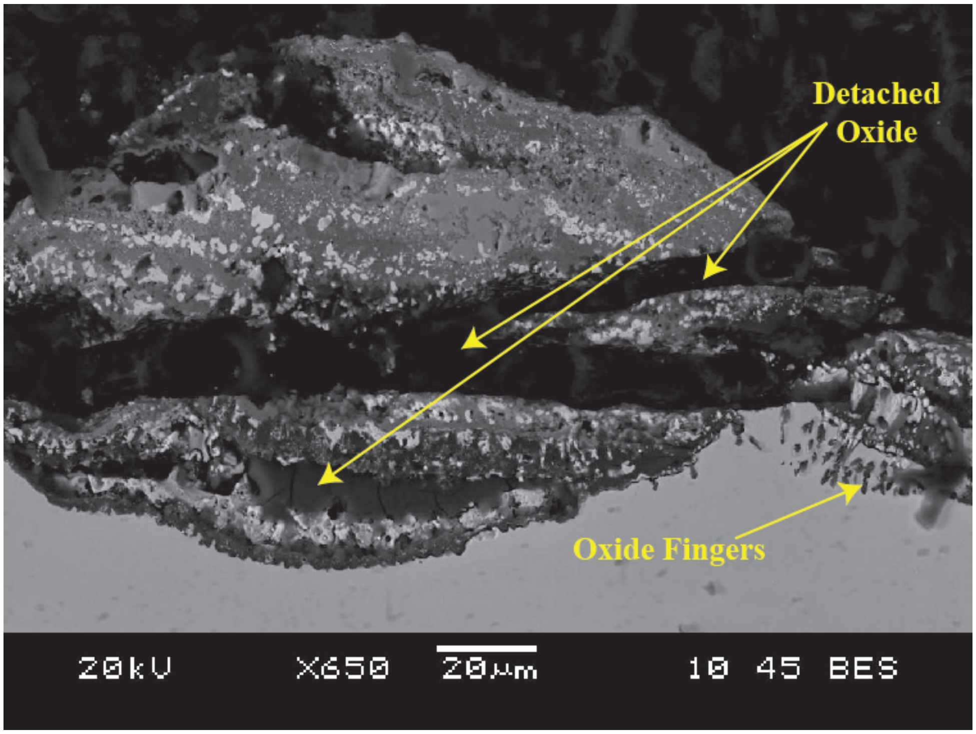

Figure 37: Backscatter electron image of a super-oxidized region on the 72 hr un-coated CMSX-486 sample showing regions of spalled material within the super-oxide scale. Oxide fingers are also shown reaching from the oxide into the PFZ.

96 hr – 192 hr Exposure:

Samples observed between 96 hrs – 192 hrs showed steadily increasing PFZ (which was as large as 40 μm in some areas) and oxide fingers (size now reaching 15 – 20 μm into the PFZ) as shown in Figure 38. Oxide particles within the PFZ also increased in frequency and size.

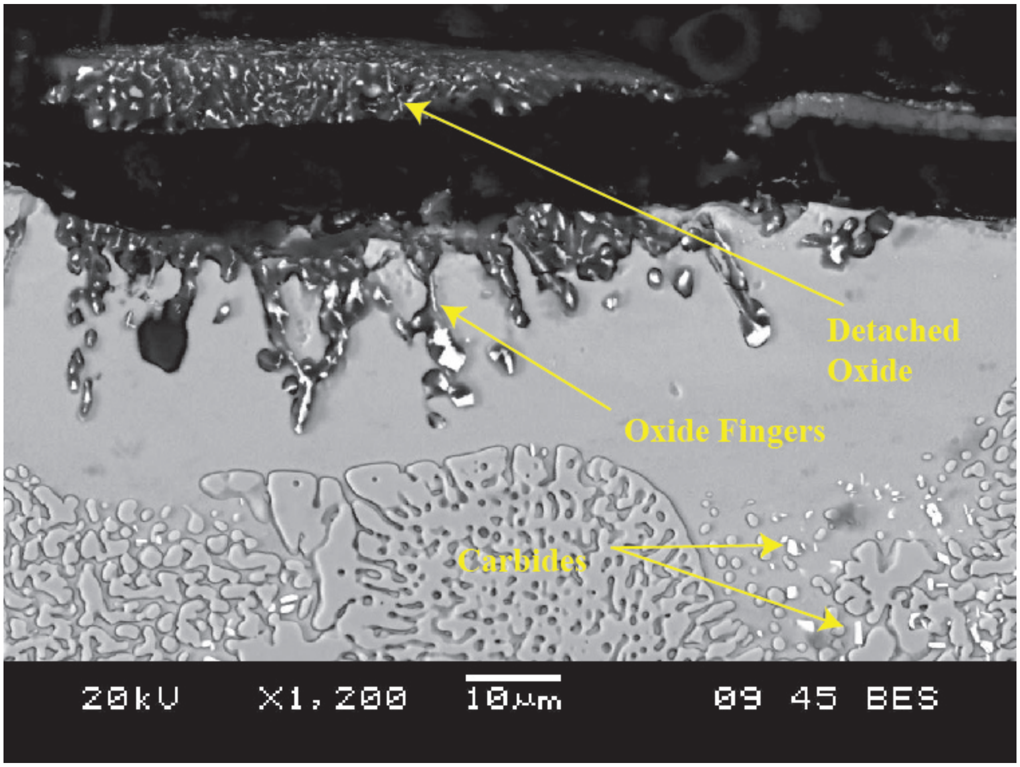

Figure 38: Backscatter electron image of the 192 hr un-coated CMSX-486 sample. Detached oxide regions, oxide fingers and some carbides close to the PFZ can be observed under the oxide scale.

Super-oxidized regions stayed relatively the same size as the 48 hr – 72 hr samples, and still showed evidence of external and internal oxide scale spallation. However, these regions were observed to border large sections of completely spalled material (usually only exposed PFZ remained) or other super-oxidized sections with large amounts of spalled material within the oxide scales.

5.1.2.2 Oxide Composition Changes with Exposure

Compositional analysis was carried out using EDS and XRD techniques as described in Section 3.0. EDS analysis of the oxides was done on the materials still attached to the substrate surface, while XRD analysis was performed on the spalled materials collected in the crucible after oxidation.

During the exposure duration, the microstructural features first observed on the 5 hr sample were consistently observed throughout the rest of the samples. The key features observed include:

1) Super-oxidized regions with a mixed, multilayered structure
2) White particle fingers reaching into the PFZ
3) Small white particles (as viewed from backscatter images) within the PFZ separate from the oxide layers
4) Bulky white particles (as viewed from backscatter images) below the PFZ within the γ/γ' substrate material.

Each of these features underwent EDS compositional analysis and later XRD results used to confirm possible compound matches to these regions.

Super-oxidized Regions:

As previously mentioned, these regions had significant mixing of the multilayer structure as compared with the CMSX-4 samples. An area map of elements performed on a super-oxidized region on the 192 hr sample is shown in Figure 39.

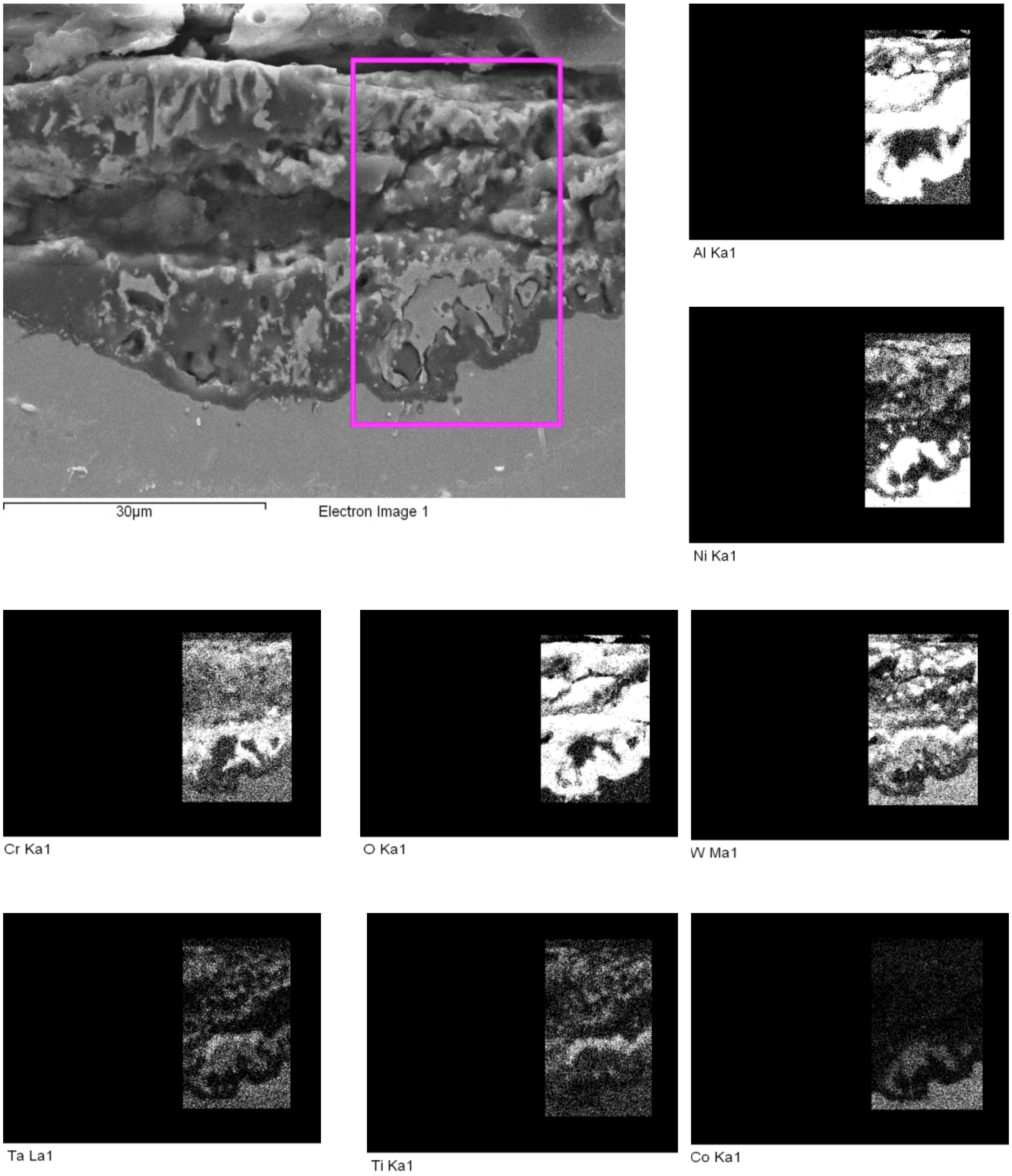

Figure 39: EDS area map of a super-oxidized region on the 192 hr un-coated CMSX-486 sample.

From Figure 39, the external and internal oxide scale is mostly composed of Al, Cr, Co, Ta and W oxides with some Ni oxides mixed within the scale.

Oxide Finger Structure:

The next significant structure observed is the finger like structure reaching into the PFZ from the bottom of the oxide scale. An EDS line scan of the finger structure is given in Figure 40.

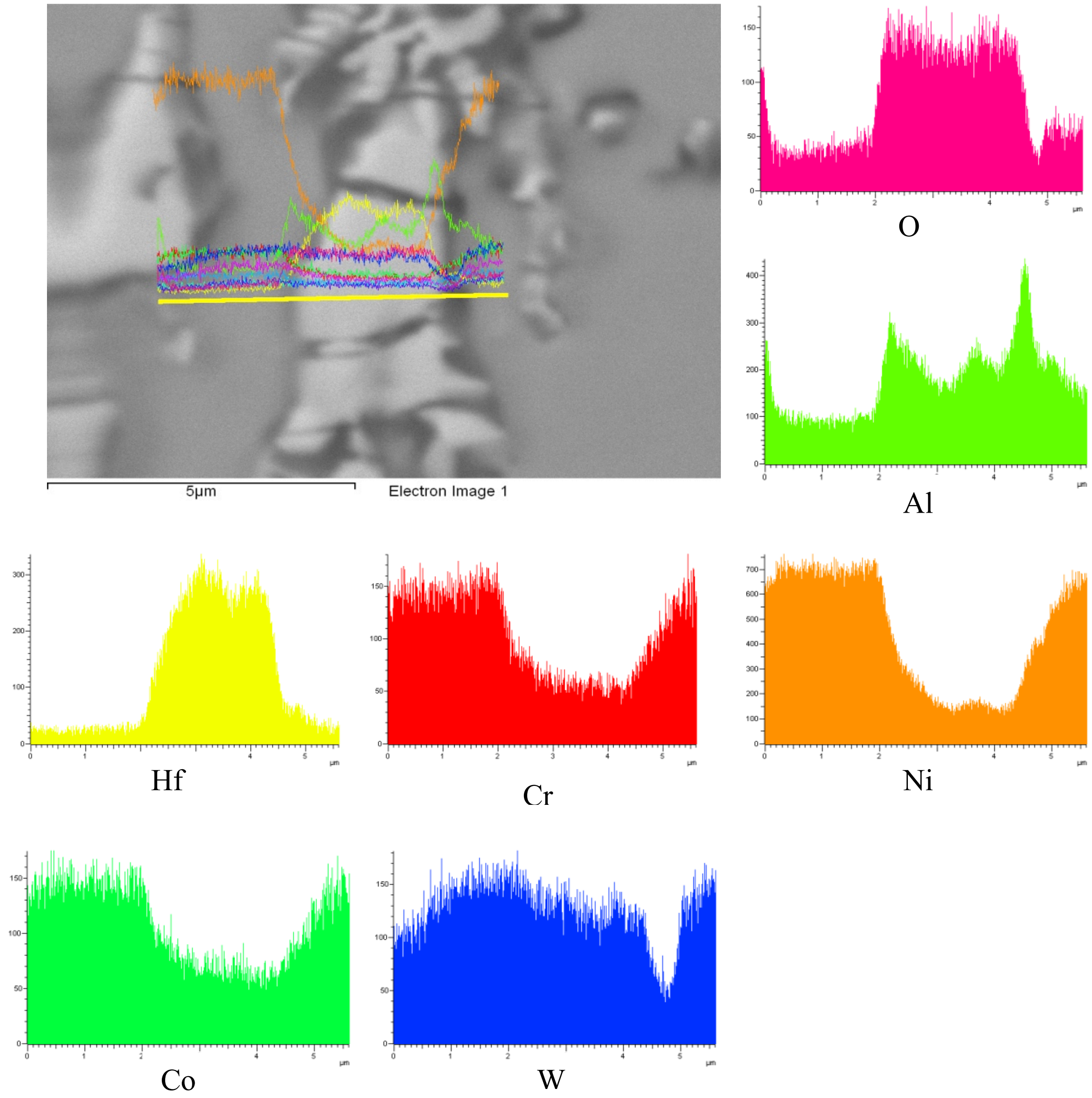

Figure 40: Line scan of the 5 hr un-coated CMSX-486 sample showing oxide fingers reaching into PFZ from oxide scale.

EDS line scans of these regions reveal the fingers are mainly rich in Al-oxides with an internal region rich in Hf-oxides. These internal Hf-rich regions within the oxide fingers are present as white sections on the backscattered electron images shown in Figure 37, Figure 38 and Figure 40. EDS line scans of the external oxide scale shown in Figure 37 and Figure 38 reveal some of the white regions to also be rich in Hf. Therefore, Hf-oxides are not only limited to the PFZ/oxide scale interface.

PFZ Particles and Large Particles in γ/γ' Substrate :

The occurrence of particles in the PFZ that were detached from the main oxide scales reveled they were often rich in Hf. Multiple scans of different particles found in the PFZ reveled little to no oxygen present, typical of the particles close to the PFZ/substrate interface, or significant oxygen content, typical of the particles close to the oxide/PFZ interface.

The large white particles (as seen on backscattered electron images) found close to or in the γ/γ' substrate showed to be rich in Ta and W and had significantly higher C content. Therefore, given the evidence, it is believed these large particles are Ta/W rich carbides, with higher levels of Hf, a similar composition to the carbides found in the as-cast material.

XRD Results:

XRD analysis was performed following the procedure outlined in Section 3.0. Three samples were initially analyzed to identify any differences in the observed diffraction patterns. If any differences were observed, additional samples would be analyzed between the two dissimilar diffraction patterns in order to determine which exposure period resulted in a compositional change.

The three sample exposure times that were chosen to be analyzed included 48 hrs, 120 hrs and 192 hrs samples. The 5 and 10 hr samples did not have a sufficient amount of spalled material to give detectable diffraction patterns. Figure 41 shows the resulting XRD diffraction patterns for the initial three samples.

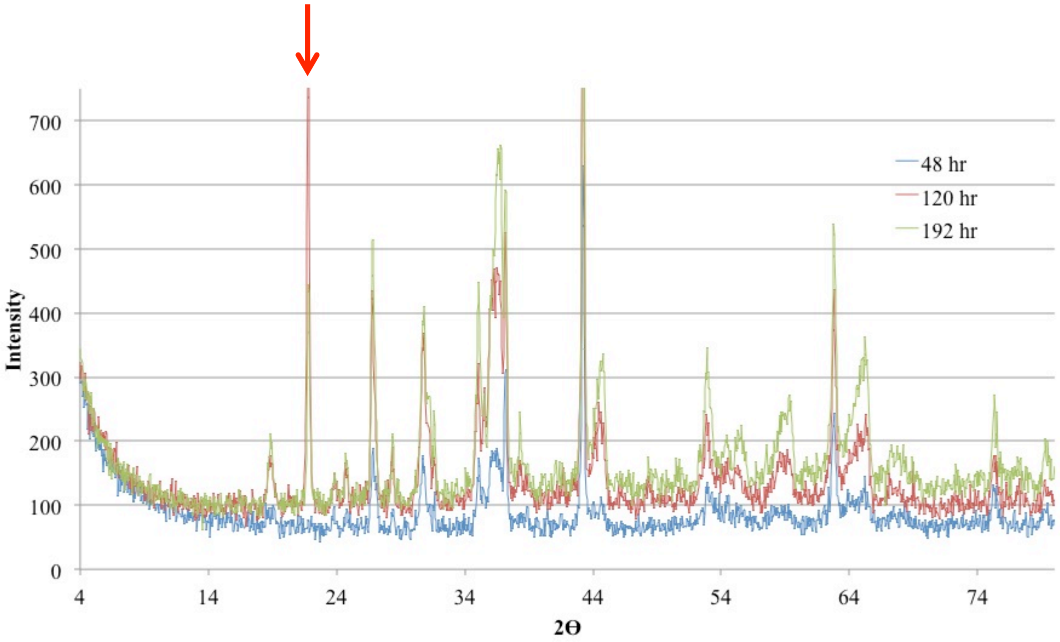

Figure 41: XRD diffraction patterns for un-coated CMSX-486 samples. Red arrow indicates a difference in observed diffraction patterns for the 120 hr and 192 hr samples compared with the 48 hr sample.

From Figure 41, there is a slight difference between the 120 hr and 48 hr samples' diffraction patterns, which is indicated by the red arrow in the figure. This single peak did not match any diffraction peak for any compound found in the samples of this work, and is therefore though to be some form of contamination of the slides used to hold the powder during the analysis. This peak is also present on the 192 hr sample's diffraction pattern, but is less intense. Other differences include the increased intensity of the pattern itself.

From these plots, and the EDS data that was gathered on each specimen, possible oxide compounds for each oxide layer could be formulated. Figure 42 depicts the XRD diffraction pattern and peak matched compounds of the 48 hr sample and Figure 43 shows an illustration with the various oxide layers labeled with possible compounds.

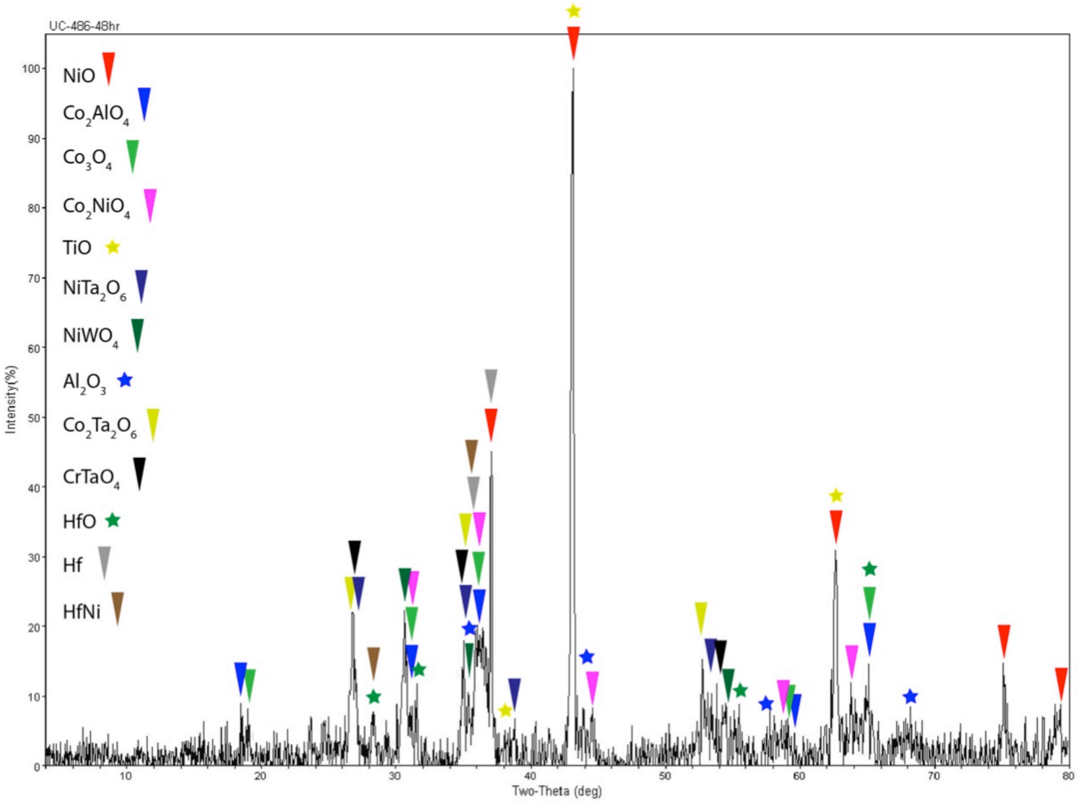

Figure 42: XRD pattern for un-coated CMSX-486 sample exposed for 48 hrs.

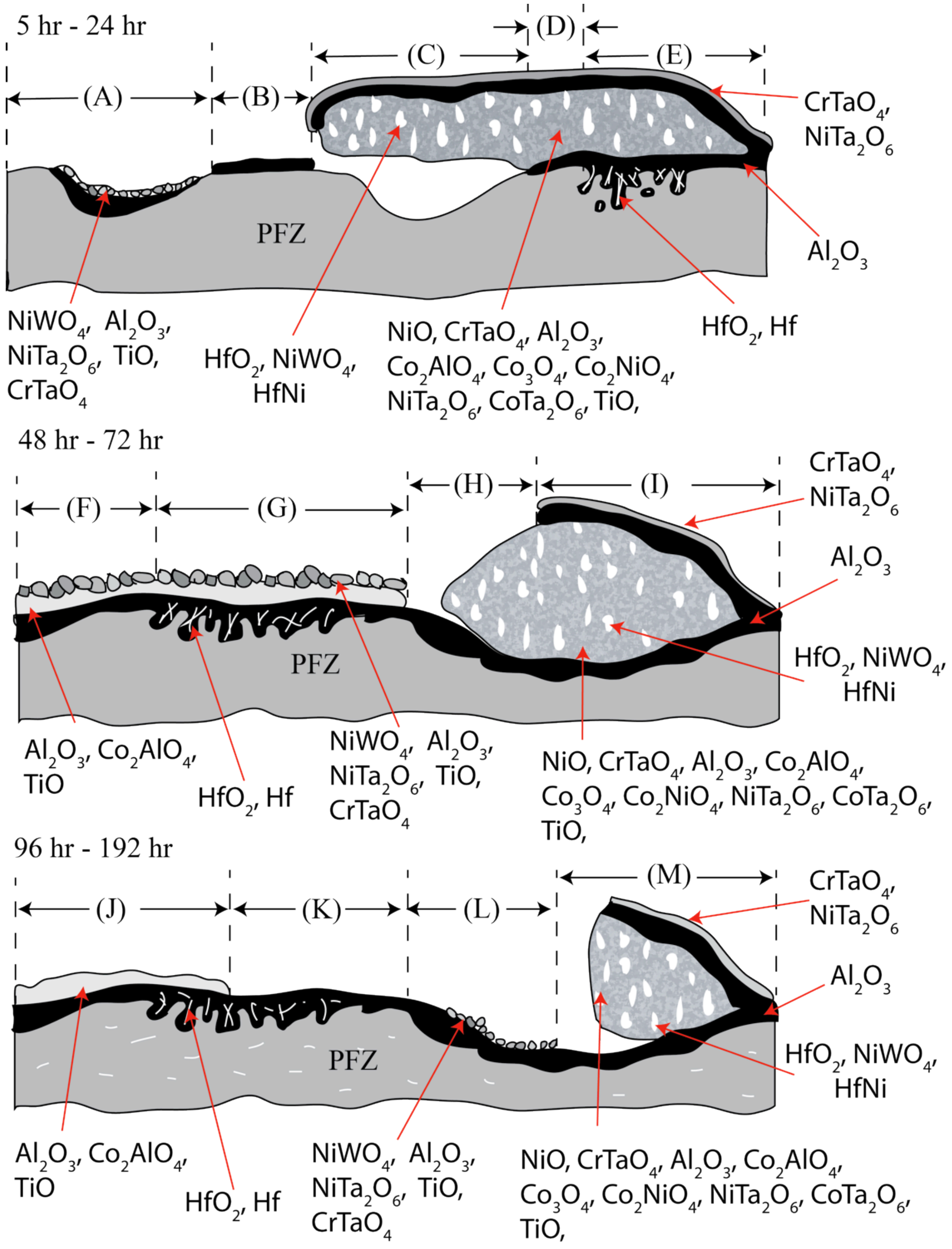

Figure 43: Summary of the possible compounds present in each oxide layers observed during high temperature exposure of CMSX-486.

Full diffraction patterns for each sample with peak matching can be found Appendix B.

5.2 Discussion of Un-Coated CMSX-4 and CMSX-486 Experiments

The results obtained from isothermal oxidation testing as described in Section 3.0 have been presented in the previous section. The oxidation conditions for the un-coated and coated materials were held constant in order to study the effect of coating on the oxidation performance of the alloys. In Section 5.2, a discussion of the various similarities and differences in oxidation mechanisms, trends and failure mechanisms are presented for the un-coated materials in order to explain the oxidation performance of the two alloys. Section 6.2 will explore the mechanisms, trends and failure mechanisms for the coated materials in order to explain the effect of coating on oxidation performance of the two alloys. Both sections will attempt to relate observed microstructural characteristics to those published in literature.

5.2.1 Microstructure and Composition

Isothermal oxidation testing of un-coated CMSX-4 and CMSX-486 has allowed for detailed analysis on the effect of microstructure on oxidation performance with increased exposure time. In particular, details such as microstructural and compositional changes, as verified with XRD, are presented in previous sections. From these results several distinct features are noticed to have a profound influence on the performance of these two alloys. These include effects of Hf, CTE mismatch, scale adherence and strength and element diffusion, which are discussed in detail subsequently.

5.2.1.1 Oxidation Performance and Mass Change

From the analysis of the mass change plots presented in Figure 27, CMSX-486 has shown to have better oxidation performance as compared to CMSX-4 in the un-coated condition due to the stronger adherence of the oxide scale to the substrate material. However, even though CMSX-486 does have better performance (less mass lost for a given exposure duration), both alloys have unacceptable oxidation characteristics in the un-coated condition since both alloys show mass loss (negative mass change) due to oxide scale spallation. Therefore, using these alloys in the un-coated condition at temperatures approaching 1100 °C is not recommended without some kind of surface treatment. Typically, single crystal superalloys are not used in any hot gas stream components as modern turbo fan jet engines without a coating deposited on the surfaces to improve oxidation performance, which is consistent with the findings of this work [*59*]. Other experiments that have been conducted on Ni-based superalloys with similar compositions to the alloys used in this work have also reported negative mass gains both in isothermal [*32, 40, 60*] and cyclic [*61*] oxidation conditions at temperatures between 1000 °C and 1200°C.

5.2.1.2 Oxide Adherence and Strength

The adherence of the oxide scales, which developed on CMSX-486, can be attributed to the formation of Hf-rich oxides. These HfO_2 regions, typically found in the alumina surface scale as illustrated in Figure 38 and summarized in sections E, G, J and K of the illustration presented in Figure 43, promote the formation of alumina fingers or peg structures into the substrate beneath. These finger structures, typically found within close proximity to eutectic regions of the substrate material, help to physically attach the oxide scale to the substrate material increasing the physical adhesion of the oxide to the substrate. This increased adhesion results in less spallation during oxidation for CMSX-486 leading to the reduced mass loss as shown in Figure 27. In comparison, CMSX-4, where HfO_2 is absent from the oxide (presented in Figure 32 and summarized in the illustration presented in Figure 36), has lower scale adherence and therefore greater mass loss. Studies found in literature, which were conducted on superalloys with various amounts of reactive elements such as Hf, Y and Zr in the superalloy or coating materials report similar peg like oxides forming at the coating/oxide or substrate/oxide interface. In almost all cases where reactive elements were included, an increase in oxidation performance was reported due to the so-called reactive element effect. However, there were some concentrations of reactive elements where too many peg structures formed due to the over doping effect, resulting in high growth stresses and upon cooling increased spallation. It was therefore reported that there is an optimum concentration of reactive elements in each system that would improve oxide scale adherence while minimizing increased stresses around the peg oxides thereby reducing spallation [*26, 30, 32, 50, 62, 63*].

Although CMSX-486 does have stronger oxide adherence as compared to CMSX-4, the oxides also appear to be much more brittle on the former, resulting in easy removal during cooling or post oxidation processing. This can also be attributed to the formation of many Hf-rich oxides, which are found in the oxide scale as white rods, (shown as white specks in Figure 37 and Figure 38). At the end of these Hf-rich rods there is an area of higher stress, much like the Hf-rich finger structures observed at the substrate/coating interface discussed previously. Upon cooling the CTE mismatch increases the stress in the brittle alumina oxide scale at these peg/finger structures, resulting in regions of high stresses and subsequent micro-cracking. Once the microcracks coalesce, large regions of the oxide scale can easily spall during cooling or be removed from polishing processes. This effect has also been reported in literature [*26, 30, 32, 50, 62, 63*].

The spallation of the single alumina rich oxide layer found on CMSX-4 and CMSX-486 likely occurred due to the CTE mismatch between the oxide and the substrate, increasing the stresses within the oxide during cooling in regions which already have high stresses. These areas of high stresses include:

1) Areas where the oxide scale has cracked and new oxides are growing between already formed oxides.
2) Areas that underwent a volume change when transient alumina underwent transformation to stable alpha alumina.
3) Areas where different oxides are forming at different rates due to different oxidation mechanisms.
4) Inherent growth stresses due to the mechanism by which the oxide develops.

Other experiments performed on alumina forming systems found in literature report similar findings where spallation is likely due to increased stresses resulting from CTE mismatch between the alloy/coating and oxides, as well as the increased stresses due to phase changes resulting in subsequent volume reduction [*16, 17, 32, 44*].

The spallation mechanisms of the super-oxidized regions found in CMSX-4 are more complex than those observed in CMSX-486. Since CMSX-4 did not have any significant formation of Hf-rich peg/finger structures, there was no increase in adherence of the oxide scale observed. In addition, there was no subsequent increase in localized stresses associated with the Hf-rich oxide structures. As such, the adherence of the oxides on CMSX-4 is much lower but the strength of the oxides on CMSX-4, especially the super-oxidized regions, is much higher than that of CMSX-486 (by observation of how easily the oxide scale was removed during post-oxidation processing). The increased strength of the oxides within the super-oxidized regions can account for, at least partially, the failure mechanisms observed to occur within these regions. This is best illustrated in Figure 31 where large cracks are observed along the boundary between the Al_2O_3 and TiO layers. Failure of the internal and external scales is seen to be due to the coalescence of voids found in the vicinity of Ti and Ta-rich oxides just above the Al_2O_3 oxide scale. This allowed cracking to proceed along the length of the Ti-rich oxide/Al_2O_3 oxide layers with very little influence from other oxide layers due to the laminar nature of the super-oxidized regions found on CMSX-4. The cracking allowed for large regions of the external scale to spall off, and in some cases the internal scale was removed as well. Since this mechanism requires sufficient number of voids within close proximity to each other and high stresses to promote the formation and propagation of cracks through the oxide scale, failure of the super-oxidized regions on CMSX-4 was less common than what was observed on CMSX-486, and accounts for the stronger oxide found on CMSX-4. The effect of Ti oxides on the adherence of alumina on Ni-based superalloys has been well documented. Most recently, Tawancy and Al-Hadhrami [*26*] noted that the cause of failure for a protective thermal barrier coating deposited on CMSX-4 was due to the occurrence of crack coalescence along the voids which formed near Ti-rich oxides in the TGO layer. They also noted that depending on the relative concentration of Ti in the substrate material, the negative effect caused by the formation of Ti-rich oxides could be mitigated. Furthermore, the formation of less protective oxides could also increase the rate of mass loss from CMSX-4 as compared with CMSX-486 [*26*].

5.2.1.3 Super-oxidized Regions

During oxidation a significant amount of oxides spalled upon cooling to room temperature for both materials. Upon a closer inspection of the oxidized surfaces, both alloys had some oxides still attached as previously mentioned. However, CMSX-4 had oxide regions which were arranged in what can be called organized multi-layered oxide scales running parallel to the substrate/oxide interface, while CMSX-486 had a much more disorganized multi-component scale structure. This can be seen clearly in the micrographs of the super-oxidized regions of CMSX-4 presented in Figure 29 and Figure 30 and CMSX-486 presented in Figure 37. The failure of the super-oxidized regions in CMSX-486 can be explained by the presence of Hf-rich oxides. However, the failure of the super-oxidized regions of CMSX-4 has more to do with the formation of specific layers as described in the previous section.

The formation of the super-oxidized regions has been reported in literature to be attributed to the extent of localized internal oxidation. Work done by Reed *et al.* [*38*] has shown as Ni diffuses to form a NiO scale with a Cr and Al rich oxide external scale, oxygen diffuses inwards through the scale in addition to short circuit pathways such as voids or cracks in the scale surface. As oxygen diffuses into the substrate, Al, Ti and Cr are selectively oxidized to form the internal oxidized regions. Temperature, element segregation, oxygen partial pressure and other factors were reported to be the primary factors which dictate how far into the material the internal oxidation zone reaches. Therefore, the different super-oxidized regions observed in both CMSX-4 and CMSX-486 can be attributed to the type and state of the oxide scale over the substrate and the presences of various elements in the sub-surface of these localized regions. The formation of oxide particles within the PFZ can also be attributed to internal oxidation mechanisms.

5.2.1.4 Effects of Oxidation on Substrate Material

During high temperature exposure both CMSX-4 and CMSX486 alloys undergo various oxidation processes as previously discussed. These oxidation processes deplete alloying elements through a process of selective oxidation, and therefore create a concentration gradient near the surface of the substrate. As exposure time increases a significant change was noticed in the $\gamma + \gamma'$ region of the substrate in both alloys. In particular, there was a significant reduction in γ' directly below the substrate/oxide interface, which continued to grow in thickness. This region was presented in the results section as the precipitate free zone (PFZ) due to the absence of any γ' precipitates. The creation of this PFZ or γ' depleted zone is well documented in literature for oxidation experiments carried out on un-coated superalloys [*38, 40, 44, 61*]. As a consequence of selective oxidation of Al and Ti, the concentration of these elements in γ' precipitates reduces to levels where γ' goes back into solid solution leaving only the matrix material (γ) appearing as a single precipitate free phase beneath the substrate/oxide interface. As oxidation continues, Al and Ti from deeper within the alloys diffuse towards the substrate/oxide interface driven by the concentration gradient created by the selective oxidation processes. The diffusion not only enlarges the PFZ, it has an effect on the morphology of the γ' precipitates as well, which is apparent in the micrographs presented in Section 5.0.

Research presented in literature shows that the size and distribution of γ' within a superalloy depends on element concentrations, in addition to many other parameters. Changes to one parameter will invariably alter the morphology and distribution of γ', which in turn affect the strength and creep resistance of the material [*35, 38, 40, 44, 61*].

6.0 Part C: Coated Oxidation Experiments

This section presents the results of isothermal exposure of the Ni-5Cr-15Al coated alloys at 1100 °C as described in Section 3.0. The results discussed in the following sections include microstructural and compositional changes during exposure, as well as an account of which oxides were present at various stages of oxidation. A discussion of the oxidation characteristics of the two alloys as well as information regarding oxidation performance of CMSX-4 and other alloys similar to CMSX-486 are presented in literature is given in Section 6.2.

6.1 Results of Ni-5Cr-15Al Coated CMSX-4 and CMSX-486 Experiments

The mass change plots are shown together in Figure 44 for ease of comparison of the two alloys. The entire surface area was used for the calculation of the mass change per area even though only one surface was coated. This is because all surfaces were exposed to the oxidizing environment and showed signs of oxidation during post oxidation analysis.

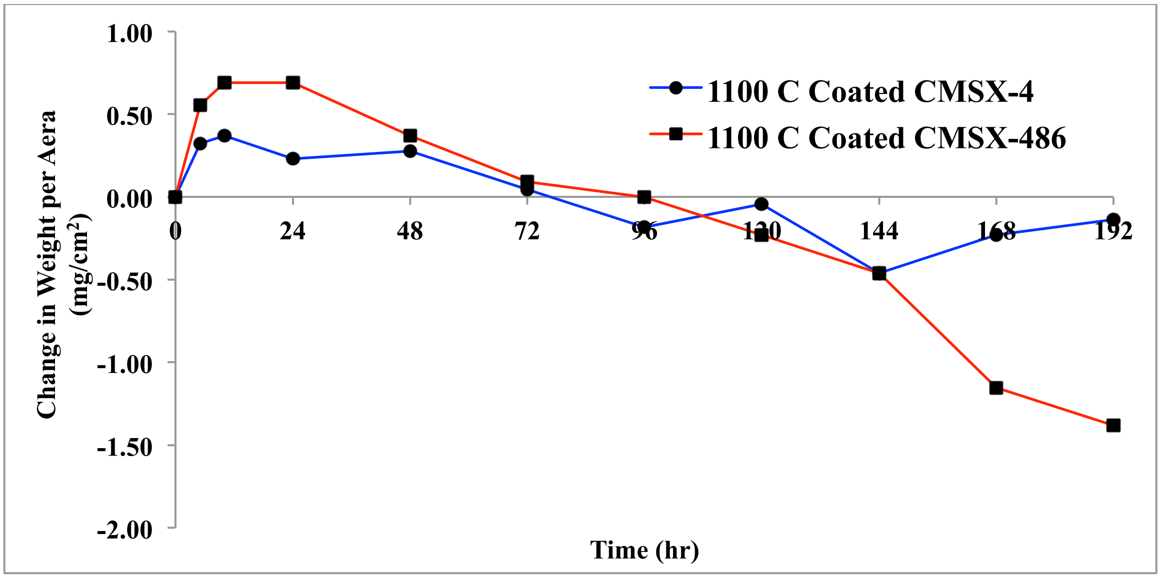

Figure 44: Mass gain plots for coated CMSX-4 and CMSX-486 after isothermal oxidation at 1100 ℃.

For CMSX-4 the total area was approximately 2.17 cm^2 and 2.30 cm^2 for CMSX-486.

6.1.1 Microstructural Changes with Exposure

Similar to the un-coated samples, both coated CMSX-4 and CMSX-486 showed signs of oxide spallation from the coated surfaces. However, micrographs of the coated surface showed more oxides attached to the surface as compared with the un-coated materials. These oxides were typically single layer, thin scales (initially 3 – 5 μm) running parallel to the substrate surface. Micrographs taken of these regions show signs of porosity and at later exposure times, (where the average oxide scale thickness was 10 – 15 μm), micro-cracking within the oxide scale. The micrographs taken of CMSX-4 and CMSX-486 illustrating this feature are presented in Figure 45 and Figure 46, respectively.

For both coated alloys, there was no sign of any significant super-oxidized regions along the coated surfaces. However, some localized regions showed signs of internal oxidation of the coating material due to the presence of oxide peg like structures. Typically, these structures stretched 10 – 25 μm into the coating material after 192 hrs for CMSX-486 and only 10 – 15 μm for CMSX-4 with widths around 5 – 10 μm for both alloys. The compositions of these structures on both alloys are discussed in more detail in Section 6.1.3. Micrographs of the peg structures for CMSX-4 and CMSX-486 are shown in Figure 47 and Figure 48.

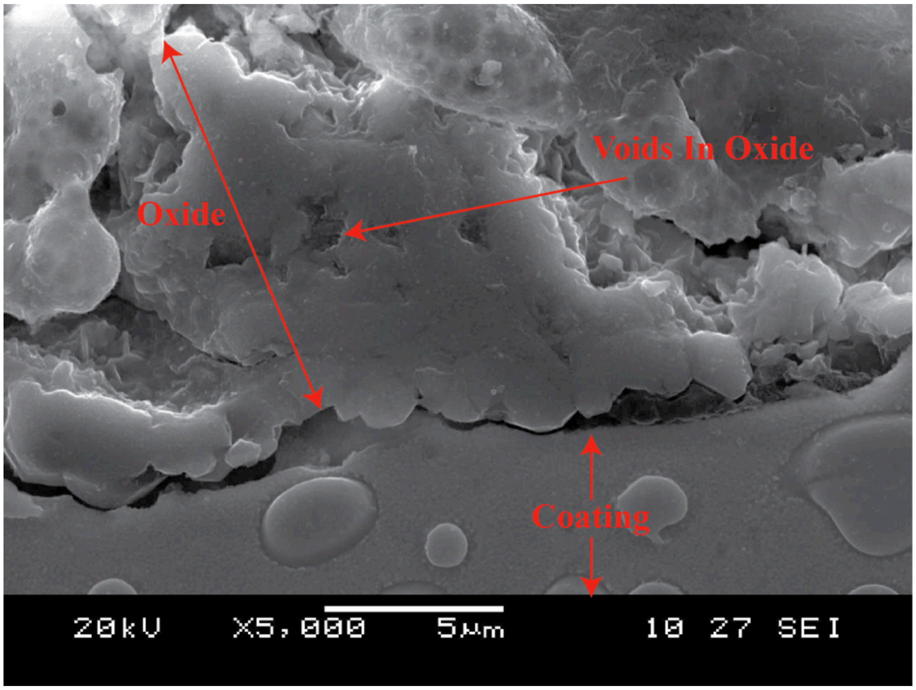

Figure 45: Oxide layer with voids as seen on 96 hr coated CMSX-4.

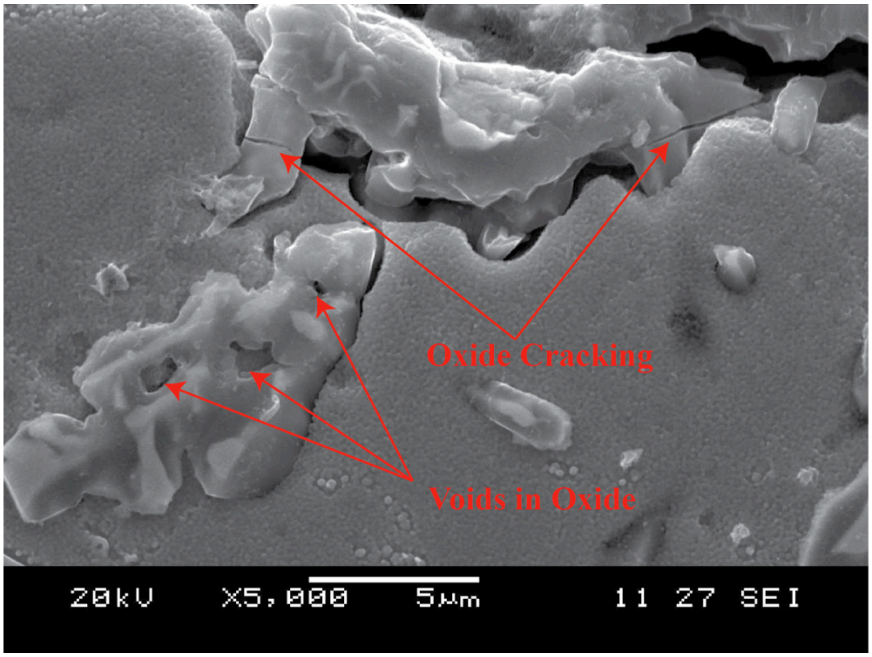

Figure 46: Oxide layer with voids and cracking as seen on the 168 hr coated CMSX-486.

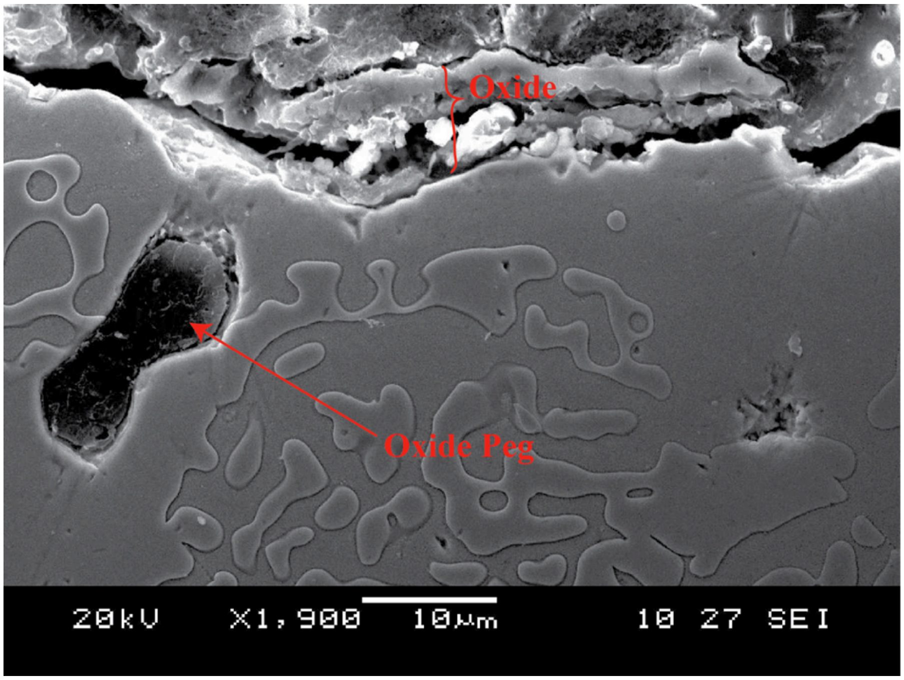

Figure 47: Oxide peg structure on 144 hr coated CMSX-4 sample.

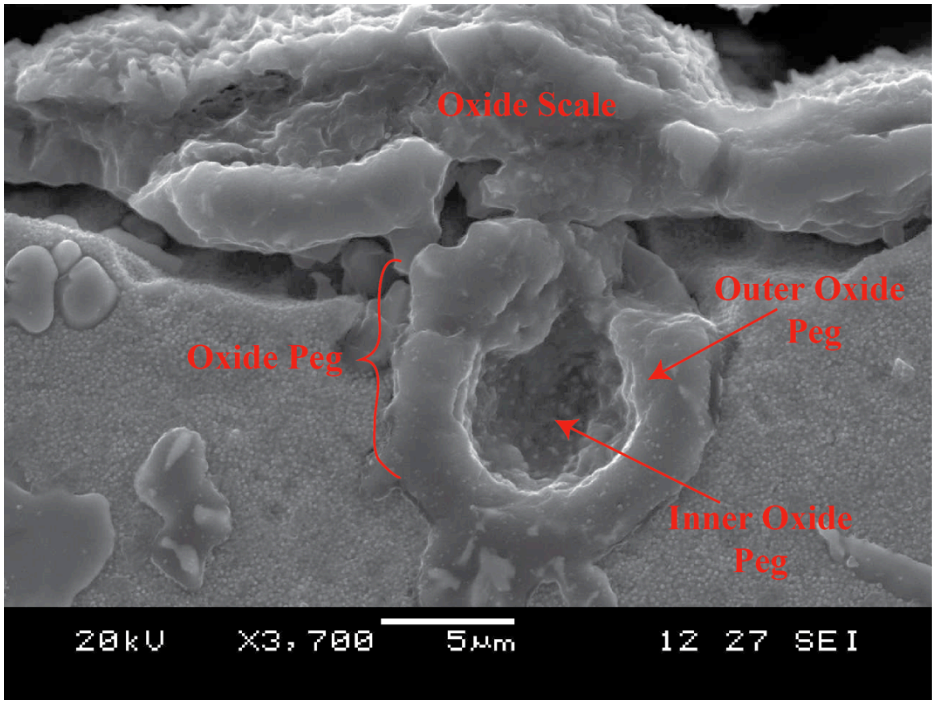

Figure 48: Oxide peg structure on 192 hr coated CMSX-486 sample. Inner oxide has been removed during polishing steps.

With exposure of the heat-treated coated samples to 1100 ℃, the multiple layer structure was still observed for all exposure durations. However, zone 3 and zone 4 for both alloys experienced the most significant structural changes while zone 2 only experienced an increase in size with increased exposure time. Minor changes in composition and γ' size (γ' coarsening and precipitation of smaller particles) were observed in zone 1 for both materials. Figure 49 and Figure 50 illustrate the development of these layers with increased exposure time for CMSX-4 and CMSX-486, respectively. These illustrations reveal that the general microstructural change for both alloys is very similar.

6.1.2 Coating Composition Change with Exposure

As mentioned in Section 6.1.1, the layered structure of the heat-treated coated materials was observed throughout the oxidation experiments. EDS analysis of these layers in conjunction with phase diagrams for Ni-Al-Cr alloys at 1100 ℃ reveal the primary phases present during the oxidation experiments.

Zone 4:

Approximate Composition: Ni - 75 at% Al - 20 at% Cr - 5 at%

In as heat-treated condition, zone 4 is single phase γ', as seen in micrographs of zone 4 presented earlier in this report. Upon exposure, zone 4 stays relatively constant for elemental concentrations of Ni, Al and Cr throughout the oxidization experiments. As exposure time continues to increase, elements from zone 4 diffuse or are selectively oxidized from this region. As a result, specific regions within zone 4 undergo a significant depletion of Al causing a phase change from strictly γ' to $\gamma + \gamma'$. This results in the reduction in size and eventual discontinuous nature of zone 4.

Zone 3:

Approximate Composition: Ni - 80 at% Al - 15 at% Cr - 5 at%

In oxidized samples, zone 3 was found to have a composition that matched the $\gamma + \gamma'$ region with large particles observed in this region. Zone 3 slowly becomes depleted of Ni and Al and enriched with Cr from the substrate resulting in a continued element concentration in the $\gamma + \gamma'$ section of the phase diagram. Micrographs of these regions on CMSX-4 and CMSX-486 confirm two phases are present (small particles, γ', within the matrix, γ). Diffusion of other elements, like Co, into zone 3 from the substrate may also contribute to the stability of the $\gamma + \gamma'$ phases.

Zone 3 Large Particles:

Approximate Composition: Ni - 75 at%   Al - 20 at%   Cr - 5 at%

Zone 3 particles (making reference to the large particles found in zone 3 of both alloy's coating) have compositions of Ni, Al and Cr which put them in the γ' region of the phase diagram at 1100 ℃. From EDS data, the composition of these particles stays relatively constant with exposure time. The decrease in size is due to element diffusion/selective oxidization from these particles resulting in the depletion of elements from the particles. As the composition is changed within localized areas of these particles, the phase shifts to become $\gamma + \gamma'$ (zone 3), which gives the appearance of the particle slowly shrinking. However, the particles that remain are shown to be consistently γ' during the entire oxidation process.

Zone 2:

Zone 2 is observed as a single phase in micrographs taken of both alloys. This phase is believed to be an intermetallic phase as a result of interdiffusion between the substrate and coating. The presence of various elements and their relative concentrations change very little during increased exposure time.

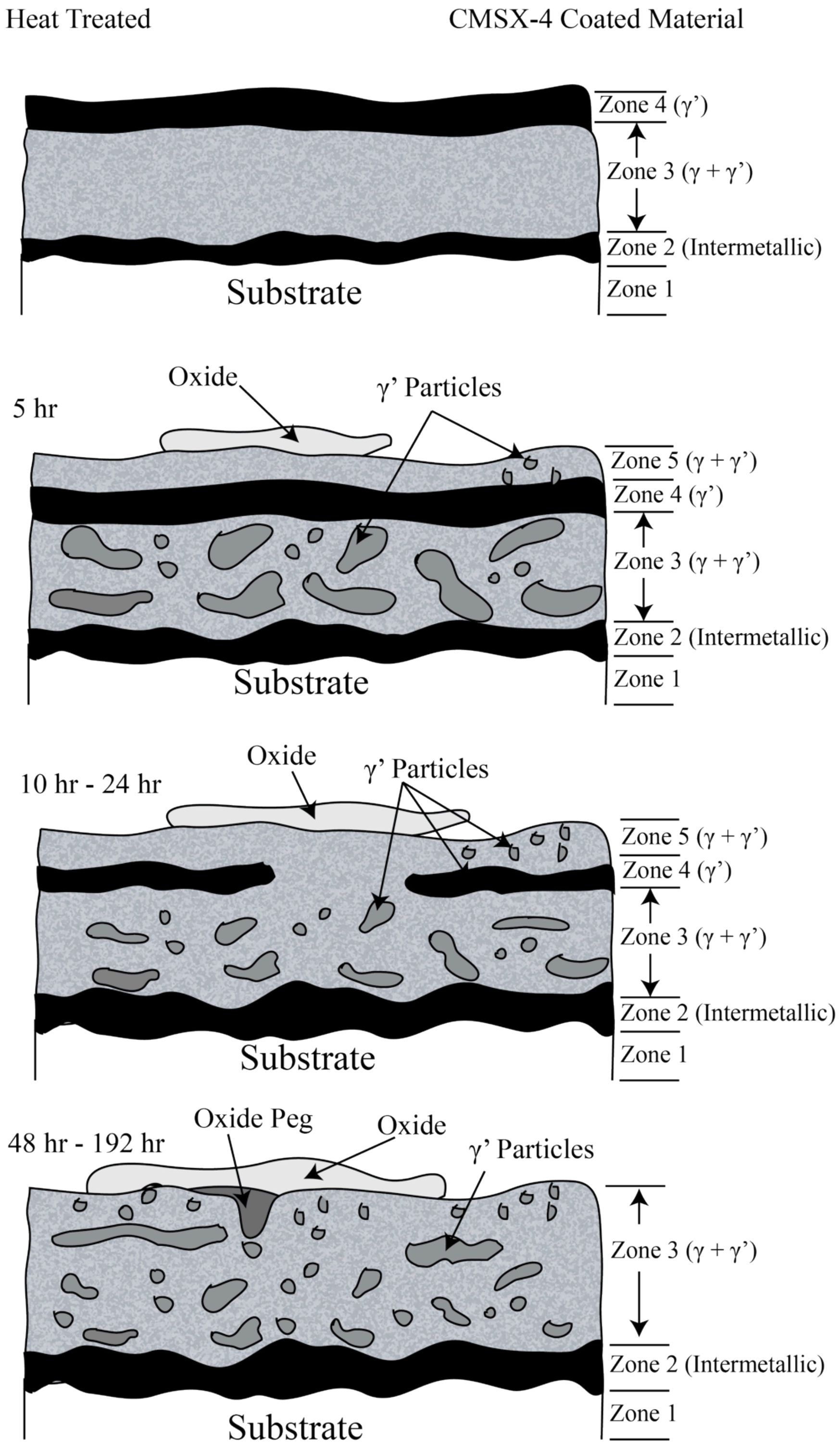

Figure 49: Illustration of the microstructural development of coated CMSX-4 during 1100 ℃ oxidation experiment.

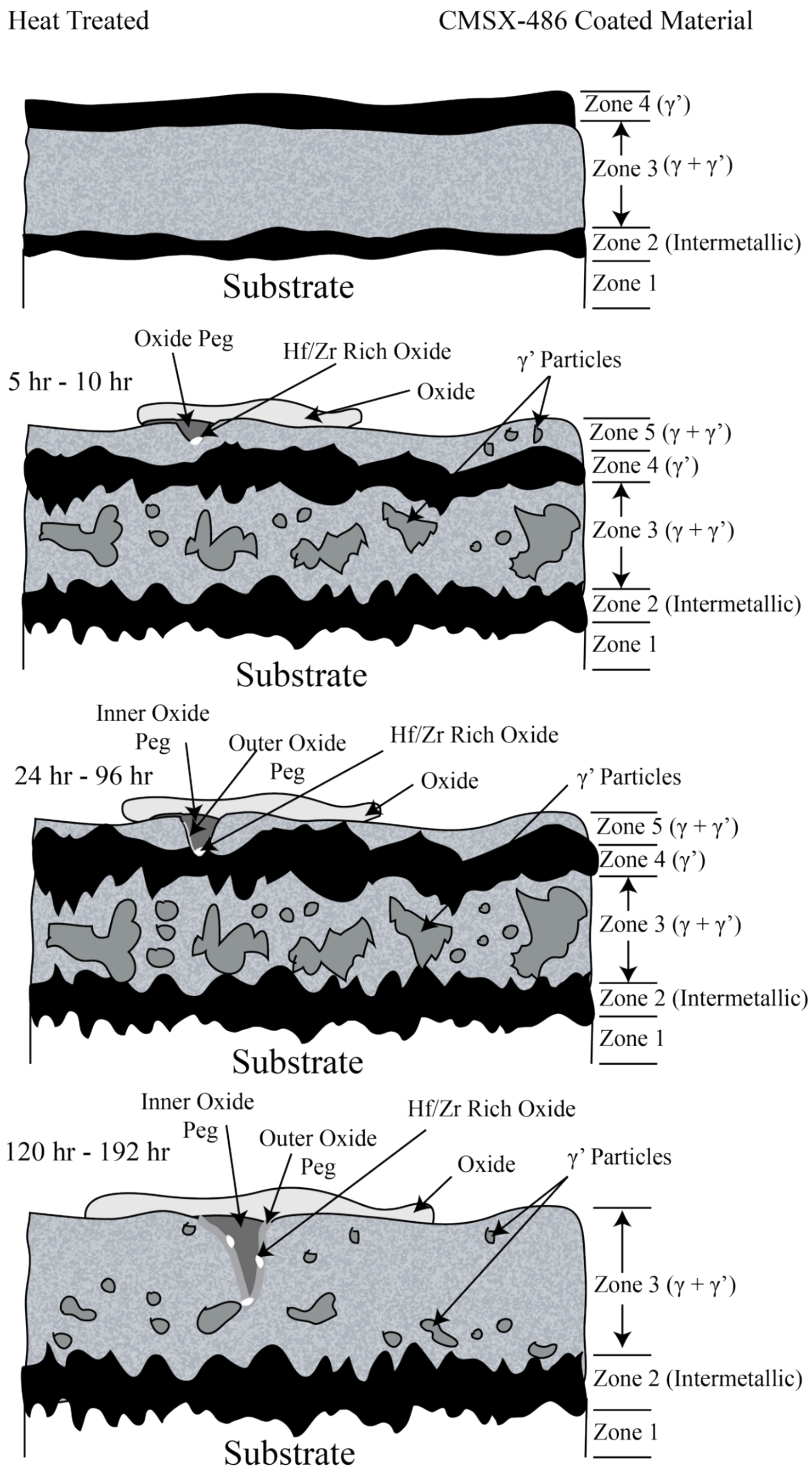

Figure 50: Illustration of the microstructural development of coated CMSX-486 during 1100 °C oxidation experiment.

The slight difference between the microstructural shape of the various zones in CMSX-4 and CMSX-486 can be attributed to the presence of and difference in minor trace elements such as Co, Ta, Mo and others not detected by the EDS detector used in this work. It should be noted that a power failure caused a brief shutdown around the removal of the coated CMSX-486 96 hr sample allowing some cooling to occur before the set point was reestablished. There was no significant change in oxidation behavior before or after the power failure.

6.1.3 Oxide Composition Change with Exposure

Compositional analysis on the oxides which formed on the coating material was done by EDS and XRD analyses as described in Section 3.3. Two distinct oxide microstructures were observed for both CMSX-4 and CMSX-486, which were described in the previous section as an oxide scale and oxide peg structures. Although these structures look structurally very similar to each other when comparing both alloys, their compositions are different.

Oxide Scale:

The oxide scale, which developed on the surface of coated CMSX-4 alloy, was shown to be primarily composed of Al-rich oxides with minor amounts of Cr and Ni present. However, when EDS scans of the oxide scale wwe performed on the coated CMSX-486 alloy, regions of high Hf and Zr oxides were detected within the Al-rich scale. Although this was not observed for all surface scales on CMSX-486, there was a significant amount of Hf/Zr oxides present in the oxidized material. Regions which did not have Hf or Zr oxides showed similar compositions to that of coated CMSX-4 (primarily Al-rich oxides with minor Ni and Cr). Line scans for CMSX-4 and CMSX-486 surface oxide scales are presented in Figure 51 and Figure 52, respectively.

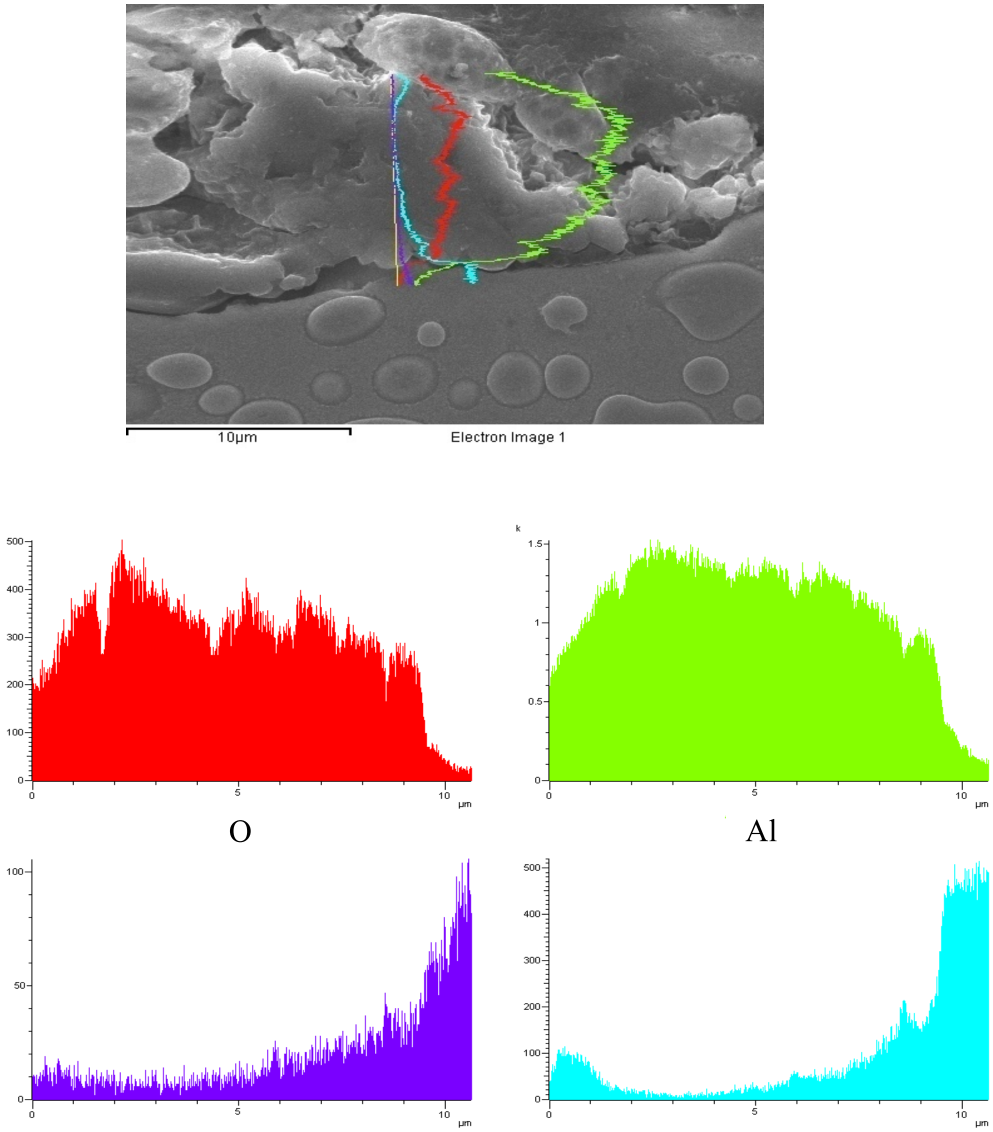

O

Al

Cr

Ni

Figure 51: EDS line scan of surface oxide on 96 hr coated CMSX-4.

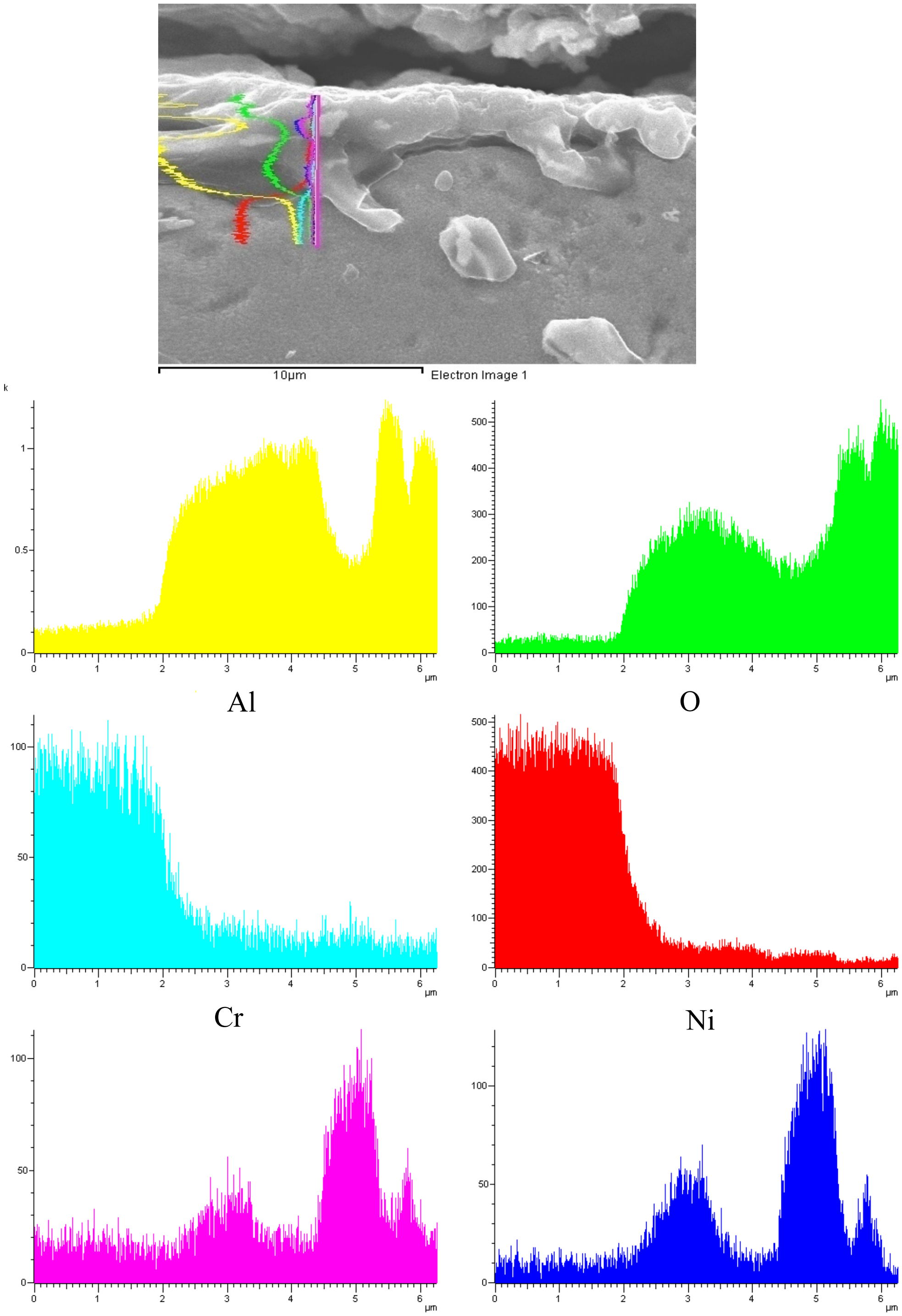

Al

O

Cr

Ni

Zr

Hf

Figure 52: EDS line scan of surface oxide on 144 hr coated CMSX-486.

With increased exposure, these surface oxides were observed to increase in both thickness and surface area on both alloys. However, the composition of these oxides remained constant with time. Only slight variations in the amount of Hf/Zr oxides were noticed. These oxides were not observed in large quantities until longer exposure times.

Oxide Pegs:

The oxide peg structures were observed on both coated alloys. Although, these structures were observed to form earlier and slightly more frequently on coated CMSX-486 as compared to coated CMSX-4. Furthermore, the peg structures observed on coated CMSX-486 underwent a transformation into a dual layer structure at longer exposure times (as shown in Figure 48 and illustrated in Figure 50). A micrograph showing the internal and external peg oxides for the coated CMSX-486 material is shown in Figure 53. Compositional analysis for both coated CMSX-4 and CMSX-486 oxide peg structures are summarized in TABLE VII.

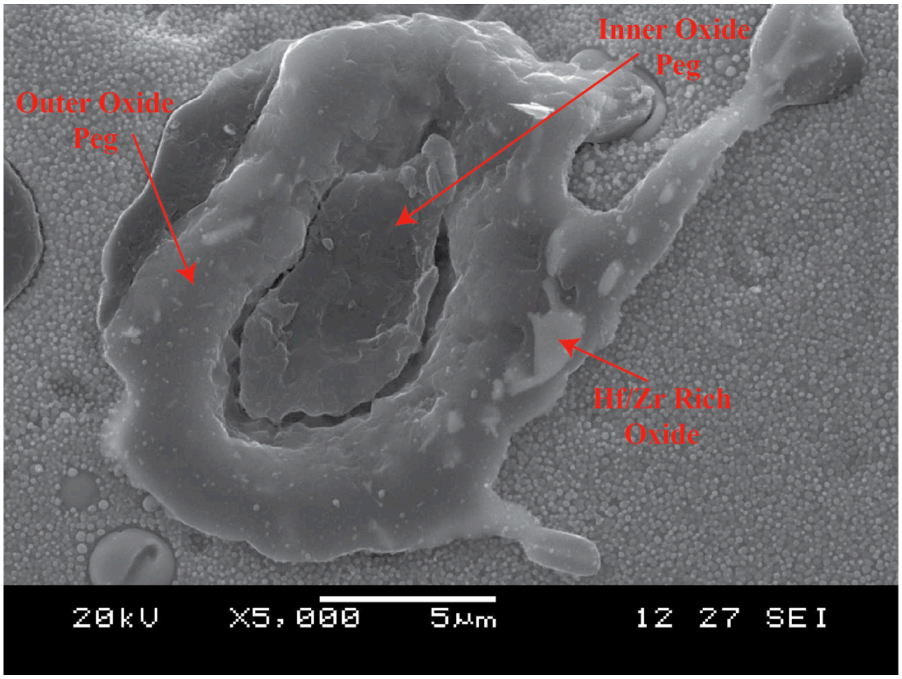

Figure 53: Inner and outer oxide peg structure for 192 hr coated CMSX-486.

TABLE VII: COMPOSITION OF OXIDE PEG STRUCTURES IN COATED CMSX-4 AND CMSX-486 192 HR SAMPLES.

	Coated CMSX-4 Oxide Peg (wt%)	Coated CMSX-486 Oxide Peg (wt%)	
		Inner Peg	Outer Peg
O	9.73	19.60	49.71
Ni	74.91	9.66	2.98
Al	2.28	60.34	47.31
Cr	8.20	3.49	-
Mo	-	3.80	-
Hf	-	3.11	-
Ta	1.66	-	-
Co	3.23	-	-

With increased exposure, these peg oxides were observed to increase in both thickness and depth in both alloys. However, the compositions of these oxides remained constant with time with only a slight variation found in CMSX-486 peg structures in the concentration of Hf and Zr oxides present. These oxide pegs were not observed frequently until longer exposure times.

XRD Analysis:

XRD analysis on the oxides, which formed on the coated CMSX-4 and CMSX-486 alloys, was performed using the procedure outlined in Section 3.3.3. The analysis was done on the 192 hr exposure samples on both alloys since these samples had the largest oxides and would make it possible to gather enough material for proper XRD measurements. Microscopic inspection of other exposure times did not reveal the occurrence of any different colored oxides that were not already present on the 192 hr samples. Therefore, due to the requirement of large areas of oxide material for the XRD technique used, specimens with shorter exposure times were not used for XRD analysis. It should also be noted that the presence of the oxides shown in Figure 54 and Figure 55 developed at different rates, and therefore were not all observed on initial exposure times. Oxides were removed an analyzed based on color, as viewed from the optical microscope, as shown in Figure 54 and Figure 55. However, some oxides were not easily removed from the underlying coating material and thus did not yield significant diffraction patterns for analysis.

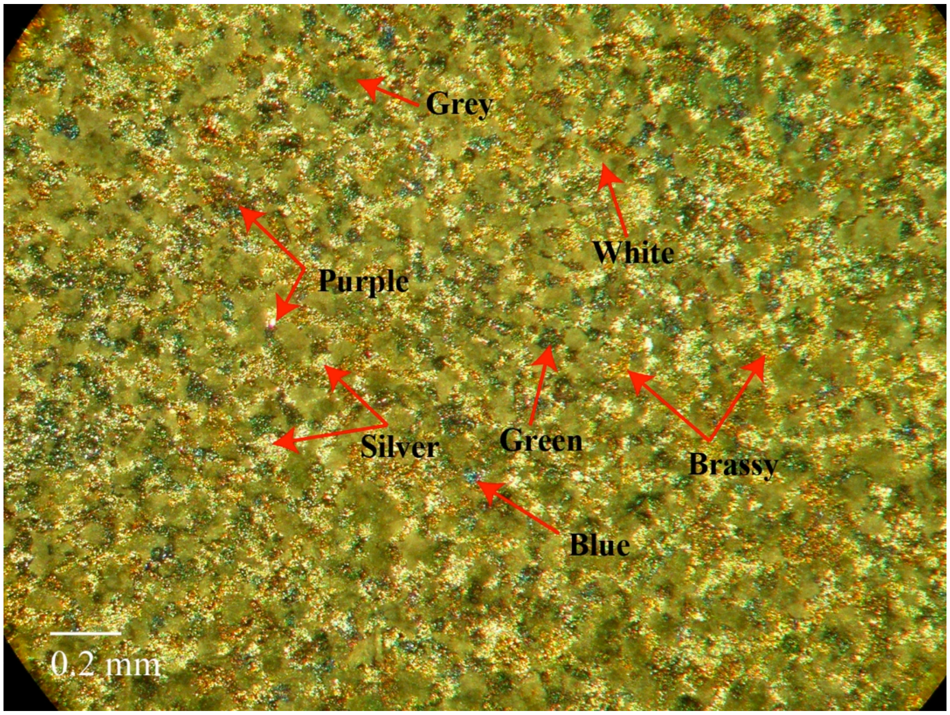

Figure 54: Top surface optical image of the coated 192 hr CMSX-4 material.

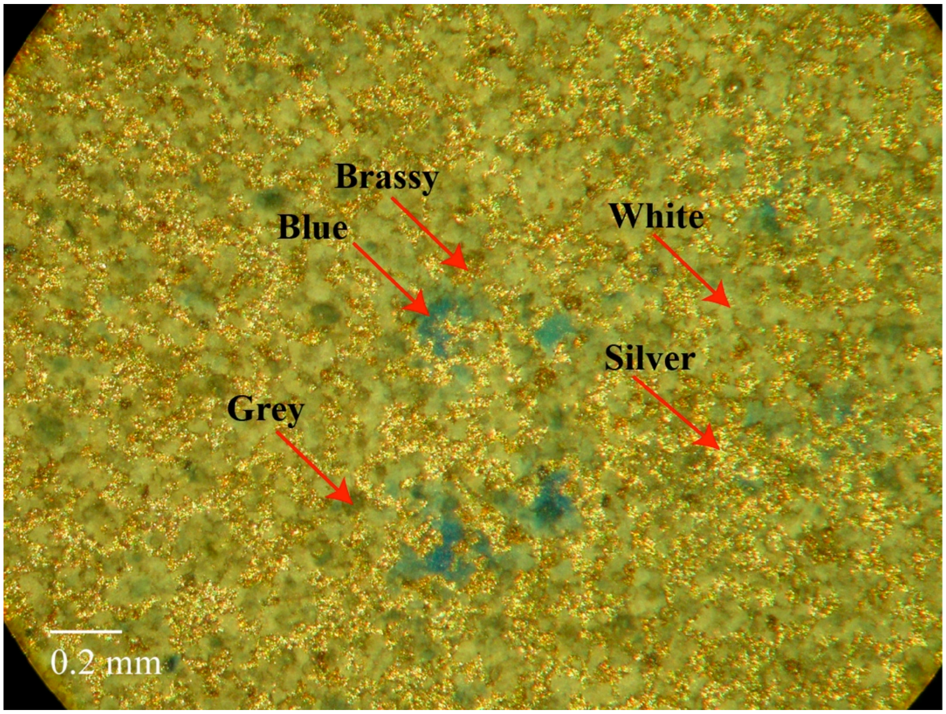

Figure 55: Top surface optical image of the coated 192 hr CMSX-486 material.

From the collected oxide samples, XRD patterns were generated. Using EDS scans of the oxides and XRD database of diffraction pattern, the peaks of the generated data were matched to possible compounds. Figure 56 shows an example of matched diffraction data and TABLE VIII summarizes the compounds present for each of the analyzed oxides.

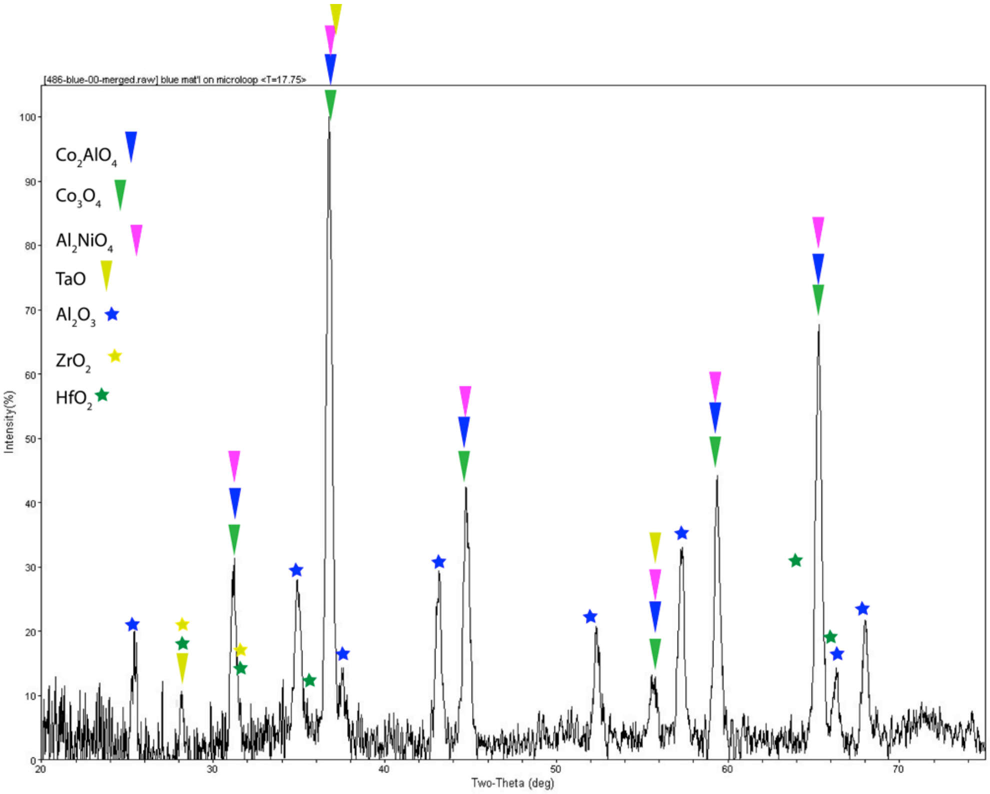

Figure 56: XRD pattern for coated 192 hr CMSX-486 blue oxide scale.

TABLE VIII: SUMMARY OF POSSIBLE COMPOUNDS MATCHED TO XRD DATA.

Coated CMSX-4		Coated CMSX-486		
Blue	Grey	Blue	Grey	White
Al_2NiO_4	Al_2NiO_4	Al_2NiO_4	Al_2NiO_4	Al_2NiO_4
Al_2O_3	Al_2O_3	Al_2O_3	Al_2O_3	Al_2O_3
Co_3O_4	Co_3O_4	Co_3O_4	TaO	TaO
-	-	TaO	-	ZrO_2
-	-	$CoAlO_4$	-	HfO_2
-	-	ZrO_2	-	-
-	-	HfO_2	-	-

Based on the obtained peak matching for the oxides that were successfully removed, it can be seen that the compounds found in each of the oxides analyzed are very similar. Therefore, it is likely the compositions of those oxides that were not analyzed are similar to those that were. The other diffraction patterns with peak matching for the coated materials can be found in Appendix C.

6.2 Discussion of Coated CMSX-4 and CMSX-486 Oxidation Experiments

The oxidation conditions for the un-coated and coated material were held constant in order to study the effect of coating on the oxidation performance of the alloys. In Section 5.2, a discussion of the various similarities and differences in oxidation mechanisms, trends and failure mechanisms is presented for the un-coated materials in order to explain the oxidation performance of the two alloys. This section will explore the development, trends and failure mechanisms for the coated materials in order to explain the effect the coating has on oxidation performance of the two alloys. An attempt to relate observed information to that which is presented in literature is also presented.

6.2.1 Microstructure and Composition

Isothermal oxidation testing on coated CMSX-4 and CMSX-486 has allowed for detailed analysis on the effect of microstructure on oxidation performance with increased exposure time. In particular, details such as microstructural and compositional changes, as verified with XRD, are presented in previous sections. From these results several distinct features are noticed to have profound influence on the performance of these two alloys. These include effects of Hf/Zr, CTE mismatch and element diffusion, which are discussed in detail subsequently.

6.2.1.1 Oxidation Performance of Coating and Mass Change

Both CMSX-4 and CMSX-486 demonstrate better oxidation characteristics in the coated condition as compared to their performance in the un-coated condition. In Section 5.2 it was shown that CMSX-486 had significantly better oxidation resistance compared to CMSX-4 when both alloys were un-coated. However, there is no significant difference between the initial oxidation characteristics of CMSX-4 and CMSX-486 (mass change and microstructural development) when comparing the alloys in the coated condition. This trend can be seen when looking at the mass change plots for the two coated alloys given in Figure 44. The absence of significant improvement in oxidation behavior for CMSX-486 in the coated condition can be explained by lack of the oxide fingers of alumina, promoted by the presence of HfO_2. With the un-coated CMSX-486, there was significant HfO_2 present on large surface areas (closely associated with the areas of eutectic microstructures) of the substrate/gas interface, which promoted the formation of many alumina fingers into the substrate beneath. As previously explained, this lead to an increased physical adhesion of the oxide to the substrate. However, in the coated experiments, only some localized regions of the coating deposited on CMSX-486 showed evidence where oxide penetration into the substrate had occurred. The lack of alumina/oxide fingers inevitably meant there was lower physical adhesion between the oxide scale and coating.

The lack of HfO_2, and by extension the decreased presence of alumina fingers, resulted from the lower availability of Hf. With the deposition of a coating, which had no additions of Hf, resulted in Hf having to diffuse into the coating from the substrate material. Since Hf has low solubility in gamma and gamma prime, which were mainly the phases present in the coating material, the diffusion rate of Hf was retarded. This lower diffusion, combined with the larger diffusion distance to the oxide/gas interface, resulted in less HfO_2 present in the coating on CMSX-486.

Essentially, since there was lower Hf present in the coating material, which was the main contributing factor for the improved oxidation performance of un-coated CMSX-486, the coating material on both alloys was forming similar oxides during oxidation (as confirmed by XRD and EDS analyses). As time went on, the development of some small, localized oxide fingers on coated CMSX-486 was not sufficient to increase the physical adhesion of the oxide scale. Therefore, the oxide development and oxidation performance were very similar between CMSX-4 and CMSX-486, which is reflected in the mass change plots. As previously discussed, the role of Hf in superalloy oxidation is well documented in literature, [*26, 30, 32, 50, 62, 63*]. Typically, in commercially used overlay coatings reactive elements, such as Hf , Y and Zr, are added directly to the coating material to improve oxide adherence to the coating. The most commonly used reactive element is Y, typically found in MCrAlY coatings. The ability to control the amount of reactive elements precisely in overlay deposition techniques allows for optimum additions of the reactive elements, thus reducing the chances of over doping (too much Hf pegs causing spallation) or under doping (not enough Hf pegs causing no effect) as seen in this work [*23, 54*].

It is unclear at this point why ZrO_2 was observed up in close proximity to the HfO_2 on coated CMSX-486 but not on un-coated CMSX-486. One possible explanation comes from a study on the effect of Zr on the stability of oxides, where Zr was added to the alloy. In particular, ZrO_2 was shown to form on Ni_3Al alloys, where it was reported that ZrO_2 could interlock with the Ni_3Al matrix [*63*]. Since the coating material in the present work consisted of either a $\gamma + \gamma'$ or a strictly γ' region directly beneath the coating/oxide interface, ZrO_2 may have been more stable on the coated CMSX-486 material by interlocking with the Ni_3Al (γ') structure beneath the oxide surface. Conversely, in the un-coated material, the region directly across for the substrate/oxide interface was the PFZ, which was predominately γ (matrix). The results of ZrO_2 found in this work seem to lead to the conclusion that this oxide is more stable when Ni_3Al is present in large quantities close to the sub-surface/oxide interface, which agrees with other studies presented in literature [*63*]. The author of this work acknowledges that there may be other mechanisms at work which play a more dominate role in determining the mechanisms by which ZrO_2 is present in the coating material and not in the un-coated CMSX-486. This may be of focus for future work.

6.2.1.2 Oxide Adherence and Strength

Oxidation of both alloys with coating deposited on their surfaces showed slow mass losses from the samples by creating a thin oxide layer over the coating surface. The effect of this thin oxide layer on the performance of the substrate and coating during oxidation is discussed in Section 6.2.1.3.

The oxide peg structures observed on both coated alloys were found to be protruding into the coating in a similar fashion as the oxide fingers found on the un-coated CMSX-486. However, the presence of these peg structures in both coated alloys is not abundant enough to influence large surface areas and produce an increase in oxide scale adherence on either of the coated alloys. The lack of peg particles resulted in a similar oxidation behavior for both alloys as previously discussed in Section 6.2.1.1.

The thin oxide scale that formed on both coated alloys is porous and brittle which are evident from the micrograph shown in Figure 45, and EDS/XRD analyses confirming the presence of strong but brittle ceramic Al_2O_3. The presence of voids in the oxide scale suggests that the volume reduction associated with the phase change of transient Al_2O_3 to stable α-Al_2O_3 is responsible for some of the voids and increased stresses found in the Al_2O_3 scale. Growth stresses as a result of selective oxidation of Al to form Al_2O_3 scale may have also increased the stresses within the thin oxide scale. Upon cooling, CTE mismatch increased the stresses found around the void regions, resulting in spallation of some oxide material or substantial cracking in the oxides that remained attached, as illustrated in Figure 46. Other experiments performed on alumina forming systems found in literature report similar findings where spallation is likely due to increased stresses resulting from CTE mismatch between the alloy/coating and oxides as well as the increased stresses due to phase changes resulting in a subsequent volume reduction [*16, 17, 32, 44*]. In addition, experimental results reported on studies regarding the primary growth mechanisms for alumina scales show that alumina primarily grows by inward diffusion of oxygen, with only minor growth due to outward diffusion of Al cations. This primarily inward growth mechanism results in higher stresses in the scale since new oxide material is preferentially forming under pre-existing scales. This results in high compressive stresses in the newly formed oxide, which may also contribute to cracking and spallation [*23*].

6.2.1.3 Effects of Oxidation on Substrate and Coating Material

The Al and Ni reserve in the deposited coating material reduced the amount of diffusion required from the substrate material, thereby eliminating the creation of the PFZ observed in the un-coated experiments. In addition, the element concentrations found in the coating were able to maintain a protective alumina oxide layer for the duration of the experiments.

The abundance of protective Al_2O_3 resulted in increased protection of the coated material, which is reflected in the increased mass gain observed for the coated samples compared to their un-coated counterparts. As illustrated in Section 6.1.2, there are no oxides present in zones 1-4 of the material or coating. These results agree with what is reported in literature, where Al_2O_3 has been shown to be stable at high temperatures and slow the transport of oxygen through the oxide scale, thus limiting the penetration of oxygen into the substrate material beneath the alumina scale. This makes alumina scales more protective and sought after compared to NiO, TiO or other oxides in high temperature applications [*3, 23, 25*]. Furthermore, the thin alumina scale, due to its limiting transport of oxygen, reduces the internal oxidation of material. This may be a contributing factor that can account for the absence of any super-oxidized regions in the coated samples, which resemble those found in the un-coated samples.

Not all the oxides shown in Figure 54 and Figure 55 were analyzed due to the difficulty associated with the removal of substantial amount of similar material. However, with the EDS and XRD data that were gathered, it is reasonable to conclude these different colored surface oxide scales are primarily Al_2O_3 with some minor inclusions of various other oxides as tabulated in TABLE VIII, such as TaO, HfO_2 and ZrO_2 to name a few. The differences in color can be attributed to the relative amount of the compounds present in each of the localized areas and/or the inclusion of contaminant (substitution element) within the Al_2O_3 compound's crystal structure. For example Al_2O_3 with Cr substituted into the structure is commonly known as rubies while pure alumina is colorless and blue Al_2O_3 is referred to as sapphires [*64*].

7.0 Conclusions

Microstructural analyses using SEM, EDS and XRD equipment were performed on un-coated and coated CMSX-4 and CMSX-486 materials, which were isothermally oxidized at 1100 ℃ for up to 192 hrs. An attempt to study the oxidation performance of Ni-5Cr-15Al coating on both alloys was made by comparing the oxidation behavior of the un-coated material to the coated material by relating the observed microstructure and compositional changes. The findings of this research are summarized as follows:

1) The un-coated CMSX-4 and CMSX-486 have unacceptable oxidation characteristics due to non-protective oxides on the substrate/gas interface, which leads to high levels of internal oxidation of the substrate materials.

2) CMSX-486 has a more adherent but more brittle oxide scale in the un-coated condition due to the formation of Hf-rich oxide peg structures in the alumina scale. These peg structures were shown to promote the formation of oxide fingers of alumina into the substrate material thereby increasing the physical adherence of the oxide scale. The presence of Hf-rich oxides in the oxide scale above the substrate/oxide interface is suggested to lead to higher stresses, which resulted in crack formation and spallation of large sections of oxides during cooling or post-oxidation handling.

3) Diffusion of Al, Ti and Ni towards the substrate/oxide interface where they were selectively oxidized depleted the near surface region of these elements in the un-coated experiments. As a result, the concentrations of Al and Ti in the γ' precipitates were reduced to levels where the γ' precipitates were

transformed back to solid solution γ phase. This left a large area of precipitate free zone close to the substrate/oxide interface. The reduction of precipitates has been reported in literature to compromise the strength and creep resistance of these areas.

4) Oxidation resistance of the coated materials increased due to the formation of a thin, protective Al_2O_3 layer. This layer is suggested to slow down the inward diffusion of oxygen, thereby reducing the diffusion of Al within the coating material. The protective Al_2O_3 layer also slowed down Al depletion and therefore no PFZ was observed.

5) The adherence and strength of the alumina layer on the coated materials was observed to be low. This can be attributed to the lack of any significant Hf/Zr-oxides resulting in insufficient amount of alumina fingers protruding into the coating material. As a result, no benefit of physical adhesion was noticed in the coated CMSX-486 material as compared with large increase in physical adhesion of CMSX-486 in the un-coated state. This reason is also suggested as the foundation for the lack of any significant difference between oxidation performance of coated CMSX-4 and CMSX-486.

6) In all cases, spallation and/or oxide removal may be a result of increased stresses caused by: CTE mismatch during cooling, growth stresses, and stresses due to volume reduction associated with transient alumina to stable alumina phase transformations. Consequently, crack formation and propagation, often through voids in the oxide scale, resulted in coating spallation.

8.0 Future Work:

1) TEM analysis should be performed, in conjunction with higher resolution metallurgical XRD analysis to better categorize the oxides and phases present in the oxide, coating and substrate regions. A more powerful X-ray source should also be considered for more penetration into the material.
2) In situ XRD measurements may also be performed to better understand which oxides develop at which point during oxidation. In addition, in situ XRD measurements can provide information regarding the development of growth stresses in the various oxide layers.
3) Different concentrations of Hf in CMSX-486 should be considered to study how varying Hf amounts affects the oxidation characteristics of Ni-5Cr-15Al coating.
4) Experimental investigations should be conducted to look at why ZrO_2 is present in the coating material and not in the un-coated material of CMSX-486. Attempts should be made to understand if having more than one reactive element take part in the oxidation process is beneficial or detrimental to oxide scale adherence.
5) Experiments similar to those carried out in this study should also be performed using the same alloy substrates but using commercially available overlay coatings in order to understand how CMSX-4 and CMSX-486 perform with coatings commonly used in industry.

9.0 References

[1] G. W. Goward, "Progress in coatings for gas turbine airfoils," *Surface and Coatings Technology*, vol. 108-109, pp. 73-79, 1998.

[2] H. Saravanamutto, G. Rogers, H. Cohen, and P. Straznicky, *Gas Turbine Theory*, Sixth Edition ed. Edinburgh Gate, Harlow, England: Pearson Education Limited, 2009.

[3] The University of Manchester, *Shreir's Corrosion*, 4th ed., R. A. Cottis et al., Eds. Amsterdam, Netherlands: Elsevier Ltd., 2010, vol. 1.

[4] P. Caron and T. Khan, "Evolution of Ni-based superalloys for single crystal gas turbine blade applications," *Aerospace Science Technology*, vol. 3, pp. 513-523, 1999.

[5] L. Huang, X. F. Sun, H. R. Guan, and Z. Q. Hu, "Improvement of the oxidation resistance of NiCrAlY coatings by the addition of rhenium," *Surface and Coatings Technology*, vol. 201, no. 3-4, pp. 1420-1425, October 2006.

[6] T. A. Taylor and D. F. Bettridge, "Development of alloyed and dispersion-strengthened MCrAlY coatings," *Surface and Coatings Technology*, vol. 86-87, pp. 9-14, December 1996.

[7] E. Tzimas, H. Müllejans, S. D. Peteves, J. Bressers, and W. Stamm, "Failure of thermal barrier coating systems under cyclic thermomechanical loading," *Acta Materialla*, vol. 48, no. 18-19, pp. 4699-47074, December 2000.

[8] D. R. Mumm and A. G. Evans, "On the role of imperfections in the failure of a thermal barrier coating made by electron beam depostion," *Acta Materialla*, vol. 48, no. 8, pp. 1815-1827, May 2000.

[9] A. G. Evans, D. R. Mumm, J. W. Hutchinson, G. H. Meier, and F. S. Pettit, "Mechanisms controlling the durability of thermal barrier coatings," *Progress in Materials Science*, vol. 46, no. 5, pp. 505-553, 2001.

[10] T. Xu, S. Faulhaber, C. Mercer, M. Maloney, and A. Evans, "Ovservations and analysis of failure mechanisms in thermal barrier systems with two phase bond coats based on NiCoCrAlY," *Acta Materialla*, vol. 52, no. 6, pp. 1439-1450, April 2004.

[11] A. Rico, J. Gómex-Garcia, C. J. Múnex, P. Poza, and V. Utrilla, "Mechanical properties of thermal barrier coatings after isothermal oxidation: Depth sensing indentation analysis," *Surface and Coatings Technology*, vol. 203, no. 16, pp. 2307-2314, May 2009.

[12] A. Gil et al., "Effect of surface condition on the oxidation behaviour of MCrAlU coatings," *Surface and Coatings Technology*, vol. 201, no. 7, pp. 3824-3828, December 2006.

[13] J. Vetter, O. Knotek, J. Brand, and W. Beele, "MCrAlY coatings deposited by cathodic vacuum are evaporation," *Surface and Coatings Technology*, vol. 68-69, pp. 27-31, December 1994.

[14] A. A. Tchizhik, A. I. Rybnikov, I. S. Malashenko, S. A. Leontiev, and A. S. Osyka, "The effect of EBPVD coatings on structure and properties of nickel-base superalloy for gas turbine blades," *Surface and Coatings Technology*, vol. 78, no. 1-3, pp. 113-123, January 1996.

[15] Y. F. Han, Z. P. Xing, M. C. Chaturvedi, and Q. Xu, "Oxidation resistance and microstructure of Ni-Cr-Al-Y-Si coating on Ni3Al based alloy," *Materials Science and Engineering*, vol. 239-240, pp. 871-876, December 1997.

[16] B. Wang et al., "Oxidation behaviour of NiCrAlY coatings on Ni-based superalloy," *Surface and Coatings Technology*, vol. 149, no. 1, pp. 70-75, January 2002.

[17] M. Reid, M. J. Pomeroy, and J. S. Robinson, "Microstructural instability in coated single crystal superalloys," *Journal of Materials Processing Technology*, vol. 153-154, pp. 660-665, November 2004.

[18] J. R. Nicholls, N. J. Simms, W. Y. Chan, and H. E. Evans, "Smart overlay coatings - concept and practice," *Surface and Coatings Technology*, vol. 149, no. 2-3, pp. 236-244, January 2002.

[19] B. G. Mendis, B. Tryon, T. M. Pollock, and K. J. Hemker, "Microstructural observations of as-prepared and thermal cycled NiCoCrAlY bond coats," *Surface and Coatings Technology*, vol. 201, no. 7, pp. 3918-3925, December 2006.

[20] R. C. Pennefather and D. H. Boone, "Mechanical degradation of caoting systems in high-temperature cyclic oxidation," *Surface and Coatings Technology*, vol. 76-77, no. 1, pp. 47-52, November 1995.

[21] M. Simonettie and P. Caron, "Role and behaviour of μ phase during deformation of a nickel-based single crystal superalloy," *Materials Science and Engineering*, vol. 254, no. 1-2, pp. 1-12, October 1998.

[22] H. Bhadeshia. (2003) University of Cambridge. [Online]. http://www.msm.cam.ac.uk/phasetrans/2003/Superalloys/superalloys.html

[23] N. Birks, G. Meier, and F. Pettit, *Introduction to the High Temperature Oxidation of Metals.*: University of Cambridge, 2006.

[24] T. Pollock and S. Tin, "Nickel-based superalloys for advanced turbine engines: Chemistry, microstructure and properties," *Journal of Propulsion and Power*, vol. 22, no. 2, pp. 361-374, 2006.

[25] ASM International, *ASM Metals Handbook Special Volume: Heat Resistant Material.*: ASM International, 1997.

[26] H. Tawancy and L. Al-Hadhrami, "Comparative performance of a thermal barrier coating system utilizing platinum aluminide bond coat on alloys CMSX-4 and MAR M 002DS," *Journal of Engineering for Gas Turbines and Power*, vol. 134, January 2012.

[27] G. Sabol and R. Stickler, "Microstructure of nickel-based superalloys," *Physica Status Solidi*, vol. 35, no. 1, pp. 11-52, 1969.

[28] K. Cheng, C. Jo, T. Jin, and Z. Hu, "Effect of Re on the precipitation behavior of mu phase in several single crystal superalloys," *Journal of Alloys and Compounds*, vol.

536, pp. 7-19, 2012.

[29] R. Darolia, D. Lahrman, and R. Field, "Formation of topologically closed packed phases in nickel base single crystal superalloys," *Superalloys 1988*, pp. 255-264, 1988.

[30] H. Guo, Y. Cui, and S. Gong, "Improved cyclic oxidation resistance of electron beam physical vapor deposited nano-oxide dispersed Beta-NiAl coatings for Hf-containing superalloy," *Corrosion Science*, vol. 52, pp. 1440-1446, 2010.

[31] V. Tolpygo, K. Murphy, and D. Clarke, "Effect of Hf, Y and C in the underlying superalloy on the rumpling of diffusion aluminide coatings," *Acta Materialia*, vol. 56, pp. 489-499, 2008.

[32] A. Göbel, A. Rahmel, and M. Schütze, "The isothermal oxidation behavior of several nickel-based single crystal superalloys with and without coatings," *Oxidation of Metals*, vol. 39, no. 3-4, pp. 231-261, 1992.

[33] K. Harris and J. Wahl, "Improved single crystal superalloys, CMSX-4 (SLS)[La+Y] and CMSX-486," *Superalloys 2004*, 2004.

[34] A. Schwartz et al., Eds., *Electron Backscatter Diffraction in Materials Science*, 2nd ed. USA: Springer, 2009.

[35] C. Sullivan and M. Donachie, Jr., "Some effects of microstructure on the mechanical properties of nickel-based superalloys," *Metals Engineering Quarterly*, 1967.

[36] M. J. Pomeroy, "Coatings for gas turbine materials and long term stability issues," *Materials and Design*, vol. 26, no. 3, pp. 223-231, May 2005.

[37] X. Huo, J. S. Zhang, B. L. Wang, F. J. Wu, and Y. F. Han, "Evaluation of NiCrAlYSi overaly coating on Ni3Al based alloy IC-6 after an engine test," *Surface and Coatings Technology*, vol. 114, no. 2-3, pp. 174-180, May 1999.

[38] A. Akhtar, S. Hegde, and R. C. Reed, "The oxidation of single-crystal nickel-based superalloys," *JOM Journal of the Minerals, Metals and Materials Society*, vol. 58, no. 1, pp. 37-42, January 2006.

[39] L. Huang, X. Sun, H. Guan, and Z. Hu, "Oxidation behavior of a single-crystal Ni-based superalloy in air at 900, 1000 and1100 C," *Oxidation of Metals* , vol. 65, no. 3-4, pp. 207-222, 2006.

[40] C. Younes, G. Allen, and J. Nicholson, "High temperature oxidation behaviour of single crystal superalloys RR3000 and CMSX-4," *Corrosion Engineering, Science and Technology*, vol. 42, no. 1, pp. 80-88, 2007.

[41] T. Tammann, *Anorg. Chem*, vol. 111, no. 78, 1920.

[42] N. Philling and R. Bedworth, *Inst. Met.*, vol. 29, no. 529, 1923.

[43] D. Monceau and B. Pieraggi, "Determination of parabolic rate constants from a local analysis of mass-gain curves," *Oxidation of Metals*, vol. 50, no. 5-6, pp. 477-493, 1998.

[44] R. Jackson, "The effect of bond coat oxidation on the microstructure and endurance of two thermal barrier coating systems," PhD Dissertation 2009.

[45] J. W. Fairbanks and R. J. Hecht, "The durability and performance of coatings in gas turbine and diesel engines," *Material Science and Engineering*, vol. 88, pp. 321-330, 1987.

[46] C. Leyens, U. Schulz, B. A. Pint, and I. G. Wright, "Influence of electron beam physical vapor deposited thermal barrier coating microstructure on thermal barrier coating system performance under cyclic oxidation conditions," *Surface and Coatings Technology*, vol. 120-121, pp. 68-76, November 1999.

[47] W. Li et al., "Microstructural characteristics and degradation mechanism of the NiCrAlY/CrN/DSM11 system during thermal exposure at 1100 °C," *Journal of Alloys and Compounds*, vol. 506, no. 1, pp. 77-84, September 2010.

[48] J. Yang, Q. Zheng, X. Sun, H. Guan, and Z. Hu, "Topologically close-packed phase precipitation in a nickel-base sueralloy during thermal exposure," *Materials Science and Engineering A*, vol. 465, pp. 100-108, 2007.

[49] C. Rae and R. Reed, "The precipitation of topologically close packed phases in rhenium containing superalloys," *Acta Materialia*, vol. 49, pp. 4113-4125, 2001.

[50] V. Tolpygo and D. Clarke, "Rumpling induced by thermal cycling of an overlay coating: The effect of coating thickness," *Acta Materialia*, vol. 52, pp. 615-621, 2003.

[51] S. Dryepondt, J. Porter, and D. Clarke, "On the initiation of cyclic oxidation induced rumpling of platinum modified nickel aluminide coatings," *Acta Materialia*, vol. 57, no. 6, pp. 1717-1723, 2009.

[52] M. He, A. Evans, and J. Hutchinson, "Effects of morphology on the decohesion of compressed thin films," *Materials Science and Engineering*, vol. 245, no. 2, pp. 168-181, 1998.

[53] A. Strawbridge and H. Evans, "Mechanical failure of thin brittle coatings," *Engineering Failure Analysis*, vol. 2, no. 2, pp. 85-103, 1995.

[54] ASM International, *Surface Engineering for Corrosion and Wear Resistance*, J Davis, Ed.: ASM International, 2001.

[55] ASM International, *ASM Metals Handbook Volume 5: Surface Engineering*.: ASM International, 1994.

[56] D. Sanders and A. Anders, "Review of cathodic arc deposition technology at the start of the new millennium," *Surface and Coatings Technology*, vol. 133-134, pp. 78-90, 2000.

[57] Wikipedia. (2010, October) Wikipedia Cathodic Arc Deposition. [Online]. http://en.wikipedia.org/wiki/Cathodic_arc_deposition

[58] T. Velikanova, K. Korniyenko, and V. Sidorko, "Aluminum-Chromium-Nickel," in *Landolt-Börnstein - Group IV Physical Chemistry*.: Springer, 2004, vol. 11A1: Light Metal Systems Part 1, pp. 371-410.

[59] Walter Gretschmann, , 2012, Senior Process Engineer Engineering Technology Support StandardAero.

[60] V. Deodeshmukh and S. Srivastava, "Long term cyclic oxidation behavior of selected high temperature alloys," *Superalloys 2008*, pp. 689-698, 2008.

[61] A. Göbel, A. Rahmel, and M. Schütze, "The cyclic oxidation behavior of several nickel-based single-crystal syperalloys without and with coatings," *Oxidation of Metals*, vol. 41, no. 3-4, pp. 271-300, 1994.

[62] Y. Wang, M. Suneson, and G. Sayre, "Synthesis of Hf-modified aluminide coatings on Ni-base superalloys," *Surface and Coatings Technology*, vol. 206, pp. 1218-1228, 2011.

[63] T. Chang, Y. Pan, and T. Chuang, "The oxidation behavior of Ni2Al-Zr alloys with various zirconium content," *Journal of Alloys and Compounds*, vol. 243, pp. 126-132, 1996.

[64] K. Dang, S. Takei, M. Kawahara, and M. Nanko, "Pulsed electric current sintering of transparent Cr-doped Al2O3," *Ceramics International*, vol. 37, pp. 957-963, 2011.

10.0 Appendix A

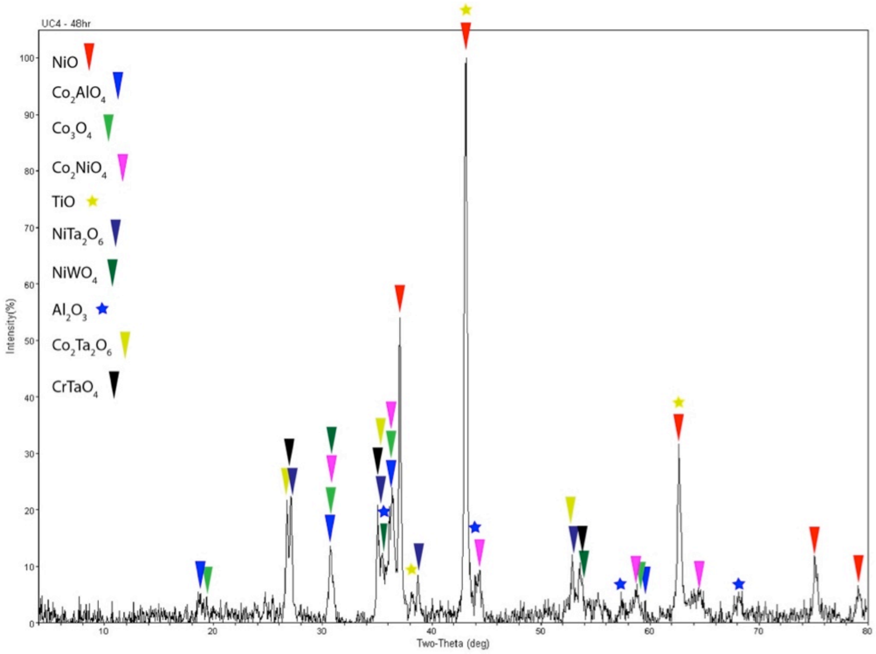

Figure 57: Peak matched XRD pattern for un-coated CMSX-4 48 hr sample.

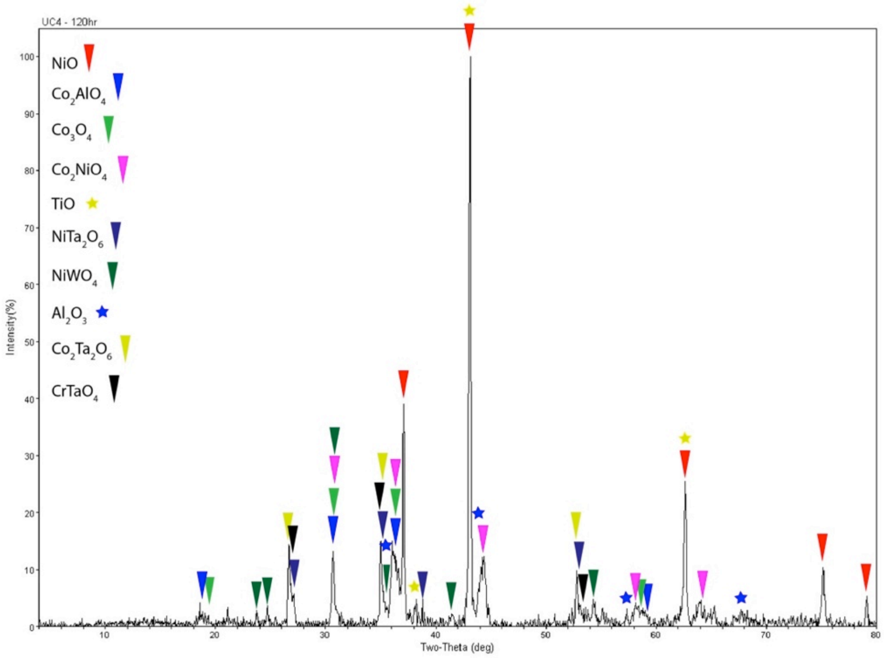

Figure 58: Peak matched XRD pattern for un-coated CMSX-4 120 hr sample.

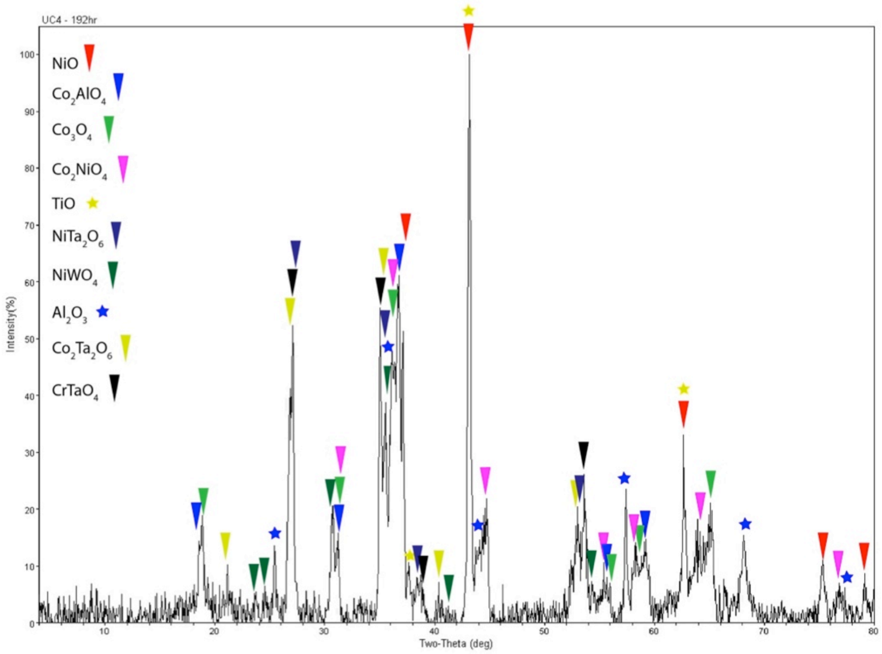

Figure 59: Peak matched XRD pattern for un-coated CMSX-4 192 hr sample.

11.0 Appendix B

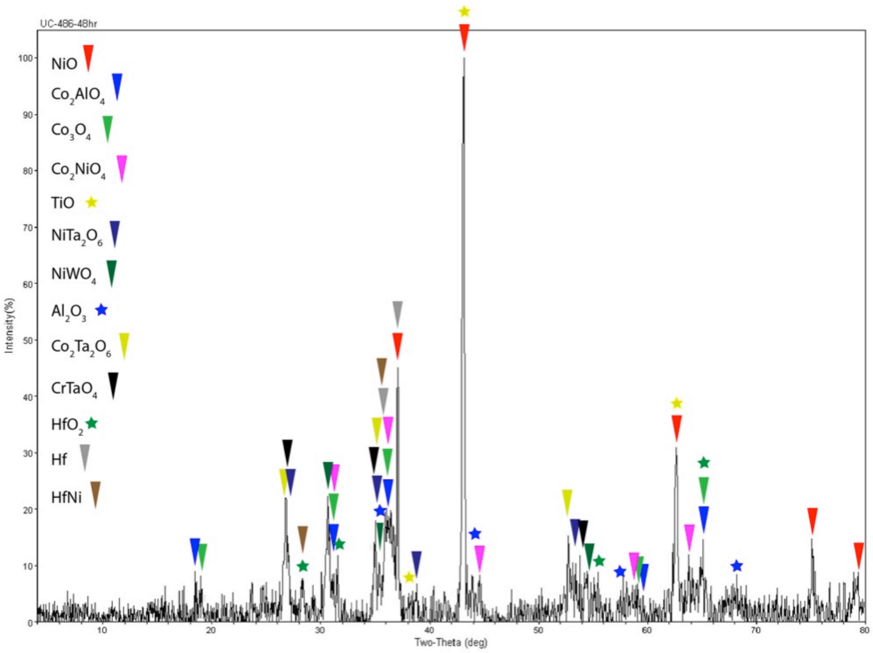

Figure 60: Peak matched XRD pattern for un-coated CMSX-486 48 hr sample.

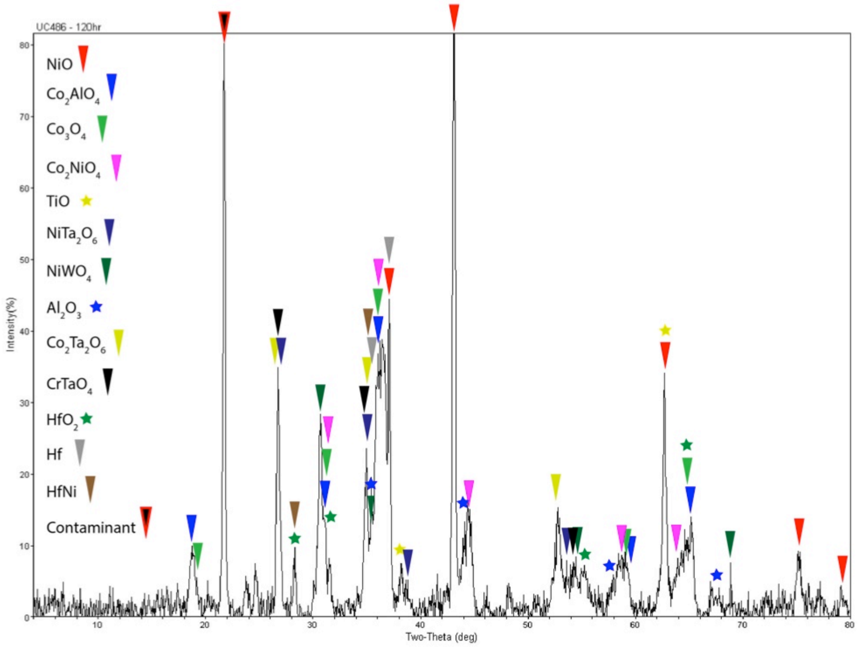

Figure 61: Peak matched XRD pattern for un-coated CMSX-486 120 hr sample.

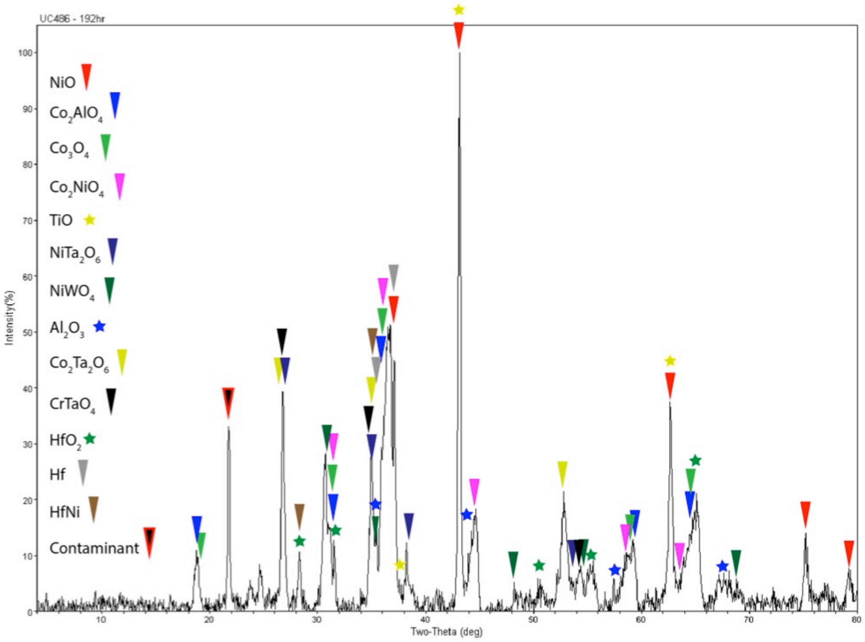

Figure 62: Peak matched XRD pattern for un-coated CMSX-486 192 hr sample.

12.0 Appendix C

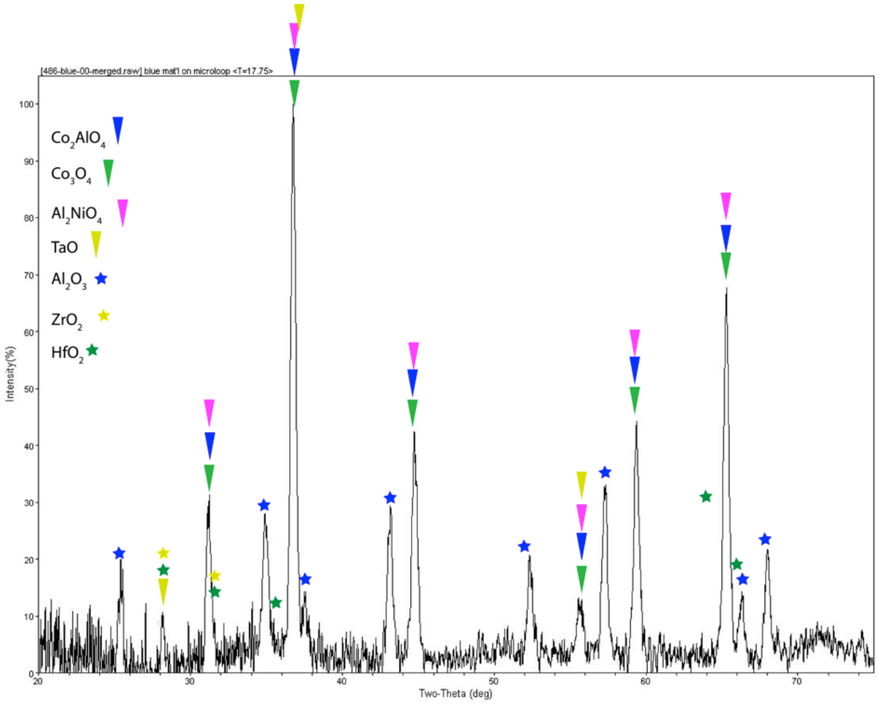

Figure 63: Peak matched XRD pattern for coated CMSX-486 192 hr sample blue oxide.

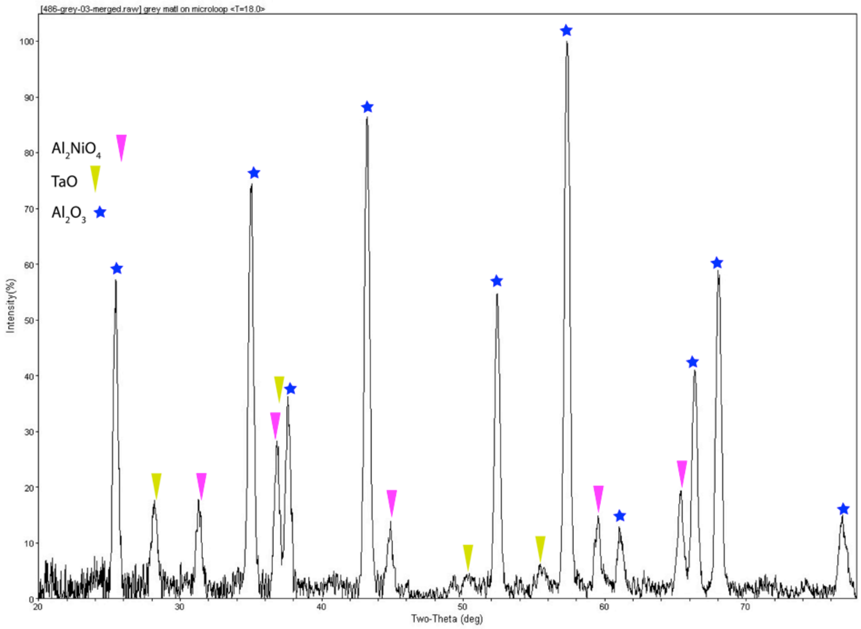

Figure 64: Peak matched XRD pattern for coated CMSX-486 192 hr sample grey oxide.

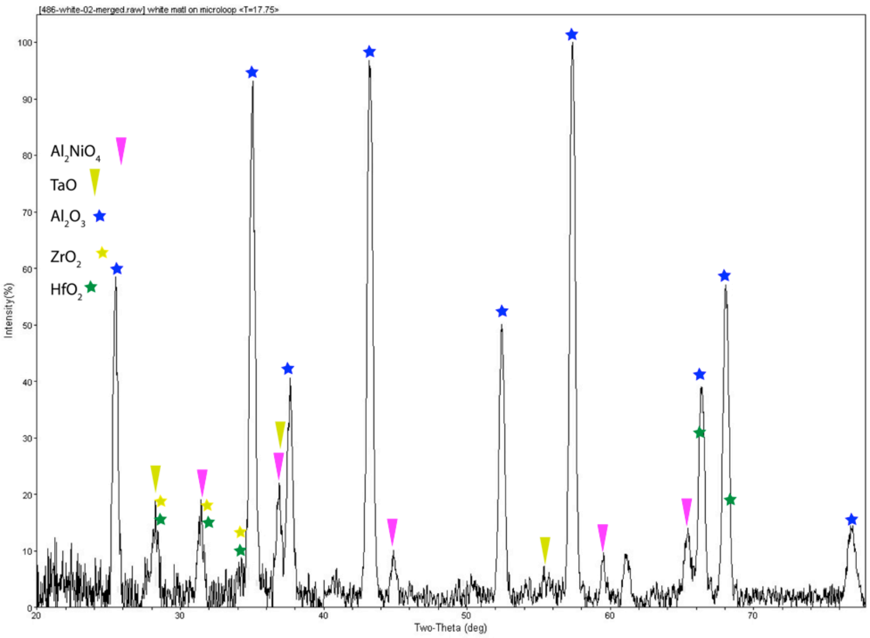

Figure 65: Peak matched XRD pattern for coated CMSX-486 192 hr sample white oxide.

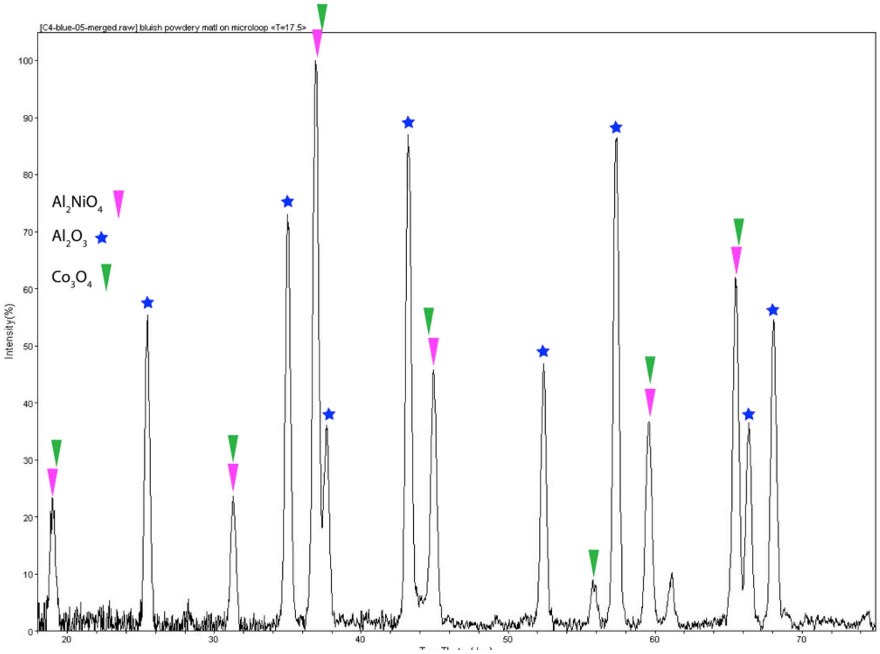

Figure 66: Peak matched XRD pattern for coated CMSX-4 192 hr sample blue oxide.

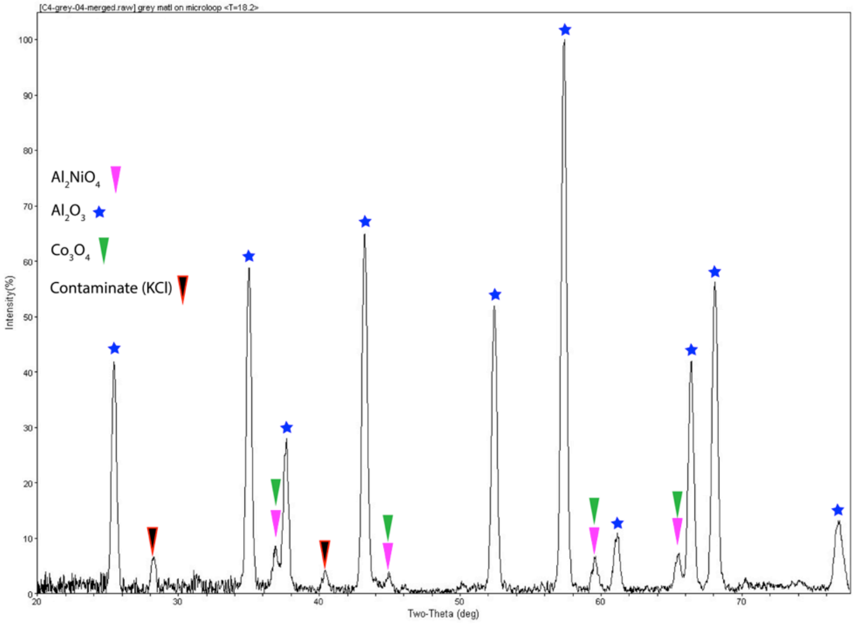

Figure 67: Peak matched XRD pattern for coated CMSX-4 192 hr sample grey oxide.